University of Alberta

# SEARCH FOR A SUPERFLUID PHASE OF CONDENSED MOLECULAR HYDROGEN

by

Joseph D. Turnbull

A thesis submitted to the Faculty of Graduate Studies and Research
in partial fulfillment of the requirements for the degree of
Doctor of Philosophy

Department of Physics
Edmonton, Alberta
Fall 2008

Library and Archives Canada

Published Heritage Branch

395 Wellington Street
Ottawa ON K1A 0N4
Canada

Bibliothèque et Archives Canada

Direction du Patrimoine de l'édition

395, rue Wellington
Ottawa ON K1A 0N4
Canada

*Your file Votre référence*
*ISBN: 978-0-494-46441-0*
*Our file Notre référence*
*ISBN: 978-0-494-46441-0*

NOTICE:
The author has granted a non-exclusive license allowing Library and Archives Canada to reproduce, publish, archive, preserve, conserve, communicate to the public by telecommunication or on the Internet, loan, distribute and sell theses worldwide, for commercial or non-commercial purposes, in microform, paper, electronic and/or any other formats.

The author retains copyright ownership and moral rights in this thesis. Neither the thesis nor substantial extracts from it may be printed or otherwise reproduced without the author's permission.

AVIS:
L'auteur a accordé une licence non exclusive permettant à la Bibliothèque et Archives Canada de reproduire, publier, archiver, sauvegarder, conserver, transmettre au public par télécommunication ou par l'Internet, prêter, distribuer et vendre des thèses partout dans le monde, à des fins commerciales ou autres, sur support microforme, papier, électronique et/ou autres formats.

L'auteur conserve la propriété du droit d'auteur et des droits moraux qui protège cette thèse. Ni la thèse ni des extraits substantiels de celle-ci ne doivent être imprimés ou autrement reproduits sans son autorisation.

---

In compliance with the Canadian Privacy Act some supporting forms may have been removed from this thesis.

While these forms may be included in the document page count, their removal does not represent any loss of content from the thesis.

Conformément à la loi canadienne sur la protection de la vie privée, quelques formulaires secondaires ont été enlevés de cette thèse.

Bien que ces formulaires aient inclus dans la pagination, il n'y aura aucun contenu manquant.

Canada

**University of Alberta**

**Library Release Form**

**Name of Author:** Joseph D. Turnbull

**Title of Thesis:** Search for a superfluid phase of condensed molecular hydrogen

**Degree:** Doctor of Philosophy

**Year This Degree Granted:** 2008

Permission is hereby granted to the University of Alberta Library to reproduce single copies of this thesis and to lend or sell such copies for private, scholarly, or scientific research purposes only.

The author reserves all other publication and other rights in association with the copyright in the thesis, and except as herein before provided, neither the thesis nor any substantial portion thereof may be printed or otherwise reproduced in any material form whatever without the author's prior written permission.

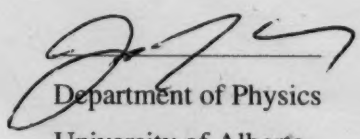

Department of Physics
University of Alberta
Edmonton, Alberta
Canada, T6G 2J1

Date: Sept 4, 2008

# ABSTRACT

Bulk molecular hydrogen is studied at low temperature in a variety of regimes, with the goal of determining possible physical conditions compatible with the observation of superflow. Using state-of-the-art quantum Monte Carlo methods, we focus our theoretical investigation on physical mechanisms that may overcome the barriers to the existence of a superfluid phase – namely, crystallization (hence particle localization). Several systems are studied toward this end, including $p$-$H_2$ films adsorbed upon the exterior surface of fullerenes, $p$-$H_2$ and $o$-$D_2$ films adsorbed upon krypton pre-plated graphite, and $p$-$H_2$ intercalated within a strictly 2D crystal of impurities. It is found that reduction of dimensionality and incommensuration are insufficient to suppress crystallization and stabilize a liquid phase of para-hydrogen at low temperature. Interesting physics is found for the case of $p$-$H_2$ intercalated within the 2D crystal of impurities, where reduction of dimensionality coupled with a periodic background potential leads to a novel phase of solid molecular hydrogen with significant quantum delocalization and particle exchanges; however, no superfluid or "supersolid" phases exist in the thermodynamic limit, as the equilibrium configuration of $p$-$H_2$ here is a commensurate, non-superfluid crystal (i.e. no vacancies nor interstitials). Finally, we study the effect of disorder and find that it leads to enhanced quantum localization and abrupt attenuation of quantum exchanges, rendering the system more classical. Altogether, significant doubt is cast upon the notion that bulk molecular hydrogen can become a superfluid, absent a direct mechanism weakening particle interactions.

# ACKNOWLEDGEMENTS

I'd first like to express my gratitude for having the opportunity to work in a positive and stimulating scientific environment here at the University of Alberta. Foremost, I want to thank my doctoral supervisor, Massimo Boninsegni, for providing, in addition to invaluable insight, the optimal conditions for a focus on scholarly research - though I am certain I at times did not take full advantage of them. I cannot list in this space every way Massimo's assistance has been critical for my scientific and professional endeavors.

Important student-student interactions within my research group must also be acknowledged. From day-to-day mutual assistance, to frank discussions about our research, I have gained tremendously from my collaboration with Fabio Mezzacapo, Long Dang, and Javier Cuervo. The utility of having colleagues to bounce ideas off of cannot be understated.

In the same vein, I would also like to acknowledge beneficial collaborations with other scientists, including Nikolay Prokof 'ev (U. Mass, Amherst) for providing a (free) summer workshop on the worm algorithm, and for checking some of my results with his code; P. N. Roy (Dept. of Chemistry, U. of Alberta) for sharing his important insights over the course of my doctorate; Horst Wiechert (Johannes Gutenberg-Universitat, Mainz) for offering unpublished experimental details of his research critical for my physical models; and Milton Cole (Penn State) for his assistance related to interaction potentials. Thanks also to Jim MacKinnon for his technical support.

The interactions with my co-scientist siblings, Matthew and Teresa, during my studies have been very important to me, in particular our encouraging of each other. I also want to acknowledge the rest of my family, especially my parents Carmen and Richard for their advice and dedication; my in-laws, Geraldine and John Mitchell, for being supportive; and my uncles Jim Turnbull and Reno Schembri, and grandmothers Maria Schembri and Violet Turnbull, for their interest in my studies.

Mattea has helped me and enriched my life in many ways over the last decade. Without my wife's love and encouragement, I would have not pursued advanced studies in the first place.

My work was supported by the Natural Sciences and Engineering Research Council of Canada (NSERC) through the PGSA and PGSB scholarship program, as well as through research Grant No. 121210893. Computing support from Westgrid and from AICT, University of Alberta is gratefully acknowledged, as is funding from the Alberta Informatics Circle of Research Excellence (ICORE) and the Faculty of Graduate Studies and Research.

# Table of Contents

**List of Figures**

**List of Tables**

**1 Introduction** **1**

1.1 Early History . . . . . 1

1.2 Superfluidity and Bose-Einstein Condensation . . . . . 2

1.3 Superfluid Hydrogen . . . . . 3

1.4 Supersolidity . . . . . 6

1.5 Summary of Original Research . . . . . 8

1.5.1 Adsorption of *para*-Hydrogen on Fullerenes . . . . . 8

1.5.2 Molecular hydrogen isotopes adsorbed on krypton-preplated graphite 9

1.5.3 Supersolid hydrogen in two dimensions: incommensuration and disorder . . . . . 11

**2 Physical Model, Methodology, and Simulation** **13**

2.1 Formalism . . . . . 13

2.2 Path Integral Monte Carlo . . . . . 19

2.2.1 Path Sampling . . . . . 20

2.3 Extended Configuration Space: Worm Algorithm . . . . . 22

2.3.1 Motivation . . . . . 22

2.3.2 Worm Sampling . . . . . 24

2.3.3 The Return on Investment . . . . . 27

2.3.4 Physical Estimators . . . . . 27

2.4 Path Integral Ground State . . . . . 31
2.4.1 Ground State Projection Methods . . . . . 32
2.4.2 Implementation: Monte Carlo . . . . . 33
2.5 Computational Details . . . . . 35
2.5.1 Boundary Conditions . . . . . 35
2.5.2 Estimates for Statistical Errors . . . . . 37
2.5.3 Interparticle Potentials . . . . . 38
2.6 A Note on Molecular Hydrogen . . . . . 42

**3 Adsorption of *para*-hydrogen on fullerenes 44**
3.1 Introduction . . . . . 44
3.2 Model . . . . . 46
3.3 Computational Method . . . . . 47
3.4 Results . . . . . 48
3.5 Conclusions . . . . . 57

**4 Molecular hydrogen isotopes adsorbed on krypton-preplated graphite 59**
4.1 Introduction . . . . . 59
4.2 Model . . . . . 62
4.3 Computational Method . . . . . 63
4.4 Results . . . . . 65
4.5 Discussion . . . . . 73

**5 Para-hydrogen in two dimensions: incommensuration and disorder 75**
5.1 Introduction . . . . . 75
5.2 Model . . . . . 77
5.3 Computational Details . . . . . 78
5.3.1 Simulations . . . . . 78
5.4 Results: $p$-$H_2$ intercalated within a periodic 2D impurity matrix . . . . . 80
5.5 Results: $p$-$H_2$ intercalated within a random 2D impurity matrix . . . . . 88
5.6 Results: $p$-$H_2$ intercalated within a nearly-periodic 2D impurity matrix . . 91
5.7 Conclusions . . . . . 93

**6 Summary and Conclusions** 95

**Bibliography** 100

# List of Tables

2.1 Parameters for the Silvera-Goldman potential given by (2.58). All parameters are dimensionless, except for $\epsilon$ (given in K) and $r_m$ (given in Å). . . . . 41

3.1 Effective $p$-$H_2$ monolayer coverages for both the corrugated and uncorrugated models of the fullerenes. For the model including corrugation, $N_C$ and $N_I$ mark the number of $p$-$H_2$ molecules in the adsorbed layer at commensuration and incommensuration, respectively, with coverages $\theta_C$ and $\theta_I$ (in $Å^{-2}$). The number $N_S$ marks the number of $p$-$H_2$ molecules in the adsorbed layer on a smooth fullerene, $\theta_S$ being the corresponding coverage. The radius $a$ of each fullerene (in Å) is also given. . . . . 54

# List of Figures


2.1 An example configuration of $N$=5 particles at $T$=1 K. Each dot denotes a single imaginary-time bead, of which there are $M$=80 for every particle. The spread of each particle gives a rough measure of the quantum zero point motion. Distance between tics is 1 Å. . . . . 21

2.2 Swap move between world-lines $A$ and $C$ between imaginary-time slices $i$ and $i + m$, as described in the text. World-line $B$ is a spectator for this swap process. . . . . 27

3.1 Energy per $p$-$H_2$ molecule $e(N)$ computed by VPI, as a function of the number of molecules adsorbed on a $C_{20}$ fullerene. Filled squares: results obtained with the angularly averaged potential (3.2). Filled circles: results obtained by explicitly modeling all carbon atoms in the fullerene. Solid lines are polynomial fits to the VPI data. Inset shows the number of particles $N$ plotted as a function of the chemical potential $\mu$, for the fully corrugated model. The chemical potential of bulk solid $p$-$H_2$ is $-88$ K, and that is where the $N(\mu)$ curve ends. . . . . 50

3.2 Same as Fig. 3.1, but for a $C_{36}$ fullerene. The commensurate layer has $N_C = 20$ $p$-$H_2$ molecules and is compressible, as evidenced by the finite slope of the curve $N(\mu)$ for $20 \leq N \leq 28$. . . . . 51

3.3 Same as Fig. 3.1, but for a $C_{60}$ fullerene. . . . . 52

3.4 Same as Fig. 3.1, but for a $C_{80}$ fullerene. . . . . 53

3.5 Radial density profiles of a $p$-$H_2$ layer adsorbed on $C_l$. Solid lines: profiles obtained for the smooth fullerene model. Dotted lines: profiles of commensurate layers on corrugated model. Dashed lines: profiles of incommensurate layers on corrugated models. Density is given in $Å^{-3}$, whereas the distance $r$ from the center of the fullerene is given in Å. . . . 55

4.1 Energy per $p$-$H_2$ molecule $e(N)$ (in K) computed by PIGS, as a function of the coverage $\theta$ (in $Å^{-2}$). . . . . 60

4.2 Potential energy surface, at the vertical equilibrium distance of molecular hydrogen, as a function of position. The two energetically degenerate sublattices of preferential adsorption sites, A and B, are shown. A *commensurate* coverage is defined as the occupation of one entire sublattice (also termed "$\frac{1}{2}$ filling"). . . . . 64

4.3 Energy per molecule $e(\theta)$ (in K) for $p$-$H_2$ (○), shifted by $-50$ K for clarity, and $o$-$D_2$ (●) computed by PIGS ($T$=0), as a function of the coverage $\theta$ (in $Å^{-2}$). Inset: $e(\theta)$ calculated using WA for $o$-$D_2$ is shown with ▼ for $\theta$=0.08389 $Å^{-2}$ and ▽ for $\theta$=0.07253 $Å^{-2}$, values marked with □ on the $T$=0 $o$-$D_2$ curve. . . . . 66

4.4 The product $\theta e(\theta)$ (in $KÅ^{-2}$) for $p$-$H_2$ (○), and for $o$-$D_2$ (●) computed by PIGS ($T$=0), as a function of the coverage $\theta$ (in $Å^{-2}$). ▲ denote coverages within regions of positive curvature. . . . . 67

4.5 Density profile of $o$-$D_2$ adsorbed to the composite substrate for $\theta$=0.08389 $Å^{-2}$ and $\theta$=0.07253 $Å^{-2}$ at $T$=1 K (solid line and dashed line respectively). The square represents the position of graphite (at $z$=0 Å) and the circle represents the position of the Kr layer (at $z$=3.46 Å). Plots have been normalized to particle number. . . . . 68

4.6 Snapshots of typical configurations of $p$-$H_2$ molecules, with $\theta$=0.07253 $Å^{-2}$ at $T$=0 K, adsorbed to the graphite/compressed Kr substrate. The positions of all molecules at each one of the imaginary time slices are shown as discrete paths. Distances are expressed in Å. . . . . 70

4.7 Snapshots of typical configurations of $o$-$D_2$ molecules, with $\theta$=0.07253 Å$^{-2}$ at $T$=0 K, adsorbed to the graphite/compressed Kr substrate. The positions of all molecules at each one of the imaginary time slices are shown as discrete paths. Distances are expressed in Å. . . . . 71

4.8 Snapshots of typical configurations of $o$-$D_2$ molecules, with $\theta$=0.08389 Å$^{-2}$ at $T$=0.5 K, adsorbed to the graphite/compressed Kr substrate. The positions of all molecules at each one of the imaginary time slices are shown as discrete paths. Distances are expressed in Å. . . . . 72

5.1 Energy per $p$-$H_2$ molecule for a regular crystalline arrangement of impurities, at the equilibrium coverage $\theta_e$=0.0381 Å$^{-2}$ as a function of the temperature, for different system sizes. Different symbols show estimates for lattices of 4 (circles), 16 (squares) and 30 (diamonds) impurities. Inset shows the energy per molecule computed at $T$=1 K as a function of the coverage $\theta$, obtained for a system of 30 impurities. . . . . 81

5.2 The superfluid density, $\rho_s$, for the 2×2 system (■), and the 4×4 system (•). Lines are guides to the eye. . . . . 82

5.3 Snapshot of a typical configuration of $p$-$H_2$ molecules at $T = 0.25$ K for $\theta$=0.0381 Å$^{-2}$ on the 4×4 system, intercalated within the periodic 2D fixed impurity matrix with density $\Omega$=0.01155 Å$^{-2}$. The positions of all $p$-$H_2$ molecules at each one of the imaginary time slices are shown as discrete paths, while impurities are shown as solid circles. All distances are expressed in Å. . . . . 84

5.4 Snapshot of a typical configuration of $p$-$H_2$ molecules at low $T$ at $\theta = \theta_e$, intercalated within the periodic 2D fixed impurity matrix (described in the text). The positions of all $p$-$H_2$ molecules at each one of the imaginary time slices are shown as discrete paths, while impurities are shown as solid circles. All distances are in Å. Inset shows a schematic representation of the ensuing phase, inferred from a visual inspection of configurations. Large circles represent impurities, whereas smaller circles are $p$-$H_2$ molecules. Red circles are $p$-$H_2$ molecules forming the 1/3 commensurate triangular phase, which can occupy either one of two equivalent lattices (different color shades). . . . . 87

5.5 Snapshot of a typical configuration of $p$-$H_2$ molecules at $T$= 0.5 K for $\theta$=$\theta_e$, intercalated within the 2D matrix of randomly placed impurities with $\Omega$=0.0133 Å$^{-2}$. The positions of all $p$-$H_2$ molecules at each one of the imaginary time slices are shown as discrete paths, while impurities are shown as solid circles. All distances are expressed in Å. . . . . 89

5.6 Ground state $p$-$H_2$ pair correlation functions ($g(r)$) for equilibrium $p$-$H_2$ coverage. All functions have been uniformly displaced upwards by their y-intercept to ease comparison. Results *a* through *d* refer to randomly placed impurities with decreasing density (from $\Omega$=0.022 (*a*) to 0.01155 (*d*) Å$^{-2}$). Also shown for comparison are $g(r)$ for bulk 2D $p$-$H_2$ (*e*), as well as for the case of a triangular impurity lattice (*f*), with impurity density $\Omega$=0.01155 Å$^{-2}$. . . . . 90

5.7 Snapshot of a typical configuration of $p$-$H_2$ molecules at $T$ = 0.5 K for $\theta$=$\theta_e$, intercalated within the aperiodic 2D fixed impurity matrix with density $\Omega$=0.01155 Å$^{-2}$. The positions of all $p$-$H_2$ molecules at each one of the imaginary time slices are shown as discrete paths, while impurities are shown as solid circles. All distances are expressed in Å. . . . . 92

# Chapter 1

# Introduction

In this chapter, we will outline the history of the general research area, provide motivation for our current studies, and broadly outline the results obtained.

## 1.1 Early History

The field of low-temperature science was born in earnest in 1908[1], when Heike Kamerlingh Onnes, building off of the work of James Dewar, first liquified $^4$He.

In 1937[2], Kapitsa [1], and independently Allen and Misener [2], discovered that bulk liquid helium-4 undergoes a superfluid transition (inferred by a fluid-fluid transition from a viscous to an inviscid state - for example, determined by experiments showing that helium could flow through narrow channels without any measurable drop in pressure) at 2.177 K. Fritz London very quickly investigated this remarkable result [3], and proposed that the phase transition in liquid helium might be related to Bose-Einstein condensation (BEC), until then viewed almost as a mathematical abstraction.

Within months of these advances, Laszio Tisza introduced the phenomenological *two-fluid model* [4] which explained the above results simultaneously with the seemingly discordant findings of other groups [5].

[1] Also, Lev Landau, 1962 Nobel Laureate in Physics for his theory describing the properties of superfluid helium-4, was born in this year.

[2] Robert C. Richardson, 1996 Nobel Laureate in Physics for his discovery of superfluid $^3$He, was born that year.

In Tisza's two-fluid model, helium-4, below its transition temperature, $T_\lambda$, mathematically contains two components - one is viscous, termed the *normal* component, and the other is inviscid, termed the *superfluid* component (which is irrotational, carries no entropy, nor contributes to the heat capacity of the liquid). As the temperature is lowered below $T_\lambda$, the ratio of the superfluid to normal component increases; this feature of the theory also provided a framework to partially understand the early torsional oscillator results of Andronikashvilii a decade later, who measured the temperature dependence of the moment of inertia of a torsion cell filled with helium, and found that the moment of inertia decreased continuously upon cooling the cell [6].

Landau later expanded upon Tisza's work, and introduced a quasiparticle model to better explain some of the features of superfluid helium, including the behavior of the specific heat as a function of temperature [7]. His proposed roton excitation picture, quantitatively confirmed in experiments a decade later [8], provided a theoretical foundation for the two-fluid model, and permitted a direct calculation of the superfluid density (with the obtained values confirmed in later experiments).

In the last three-quarters of a century, an enormous body of literature has been devoted to the plethora of interesting properties of superfluids, such as extremely high thermal conductivity [9], and novel film flow [10]. Intervening discoveries related to the field also include the theory of superconductivity [11], and the formation of Bose-Einstein condensates using ultra-cold gases [12]. Yet, aside from $^4$He, the only other system to be experimentally observed in a *bulk* superfluid state is another isotope of helium, (wherein fermionic $^3$He particles pair up to form composite bosons).

## 1.2 Superfluidity and Bose-Einstein Condensation

Today, we still define superfluidity (SF) as a phase of matter with the macroscopic property of zero viscosity - a pure superfluid flows without resistance. In analogy with superconductors, a superfluid set in motion (below a certain critical velocity) around a closed loop would flow continuously without friction for as long as it was kept below the transition temperature.

Bose-Einstein condensation (BEC) occurs when a system composed of bosons, which

are integer spin particles, congregate into the same single-particle quantum state. Qualitatively, BEC can be said to occur when the thermal wavelength of a particle of mass $m$, at temperature $T$, $\lambda = \hbar/\sqrt{mT}$, is of the order of the average interparticle distance. As an example, a system of non-interacting bosons (referred to as a free Bose gas), with the parameters corresponding to those for bulk 3D $^4$He, has a BEC critical temperature of approximately 3 K, reasonably close to the superfluid transition temperature for $^4$He.

The connection between SF and BEC, however, is not one-to-one. A free Bose gas, which undergoes BEC, is *not* a superfluid - interactions must be switched on in order to induce SF [13].

Similarly, experimental and theoretical studies of 2D helium-4 films reveal superflow, but the macroscopic occupation of a single-momentum state (BEC) cannot occur in fewer than three dimensions at *finite* temperature [13, 14, 15].

BEC and superfluidity in 3D, for translationally invariant systems, are associated with off-diagonal long-range order signified by a finite asymptotic value of the one-body density matrix. The one-body density matrix for 2D superfluid films, on the other hand, cannot asymptote to a finite value; specifically, the decay of the one-body density matrix, instead of being exponential as in the case of normal fluids and solids, follows a power law, with such a decay indicative of what is termed 'off-diagonal *quasi*-long-range order'. Such 2D physics is explained by the theory of Kosterlitz and Thouless (KT) [16, 17].

## 1.3 Superfluid Hydrogen

Our microscopic understanding of superfluidity could be significantly enhanced by the discovery of another bulk superfluid system. It is agreed upon that the critical ingredients include a low mass $m$, and a relatively weak interparticle interaction $\epsilon$. These considerations are together encapsulated by the dimensionless de Boer parameter [18],

$$\Lambda = \frac{\lambda}{\sigma} = \frac{\hbar}{\sigma(m\epsilon)^{1/2}} \tag{1.1}$$

where $\sigma$ is the characteristic scale of confinement, and $\sigma$ is the characteristic potential energy (generally defined in terms of a potential-well depth). When $Lambda \gtrsim 1$, quantum

effects play a dominant role; when $\Lambda \lesssim 1$, quantum effects are small, including macroscopic quantum behavior such as BEC and SF.

The square of $\Lambda$ gives a measure of the ratio of the particle's zero-point energy when trapped in a box of linear size $\sigma$ to its potential energy in a well of depth $\epsilon$. Decreasing $m$ or $\sigma$ enhances the kinetic energy, while decreasing $\epsilon$ decreases the potential energy.

It is natural to thus seek out Bose many-body systems comprised of particles for which $\Lambda$ is large. Aside from spin-polarized atomic hydrogen[3], the highest value is that for helium, where $^4$He has $\Lambda$=2.677. The next largest values correspond not to atoms, but to hydrogenic molecules; $\Lambda$=1.719 for *para*-hydrogen ($p$-$H_2$), and $\Lambda$=1.246 for *ortho*-deuterium ($o$-$D_2$); see section 2.6 for a related discussion. For all other atoms and molecules, $\Lambda$ rapidly decays to values well below 1.

The candidate system to explore would therefore appear to be molecular hydrogen, $p$-$H_2$ in particular. But, thus far, the push to observe superfluidity in molecular hydrogen has not met with success in the bulk.

The difficulty in experimentally observing a superfluid phase of (especially bulk) $p$-$H_2$ stems from the crystallization of the system at a temperature $T_c \approx 14$ K, significantly higher than that ($T \approx 6$ K) at which phenomena such as Bose-Einstein condensation (BEC) and, possibly, superfluidity (SF), may be expected to occur in the liquid phase [20] in 3D. Crystallization takes place because of the depth of the attractive well of the interaction potential between two hydrogen molecules, approximately three times that between two helium atoms.

The physical property of SF is microscopically underlain by quantum exchange cycles involving macroscopic numbers of identical particles. Since quantum exchanges are, in general, greatly suppressed in the crystal phase, due to particle localization, it is widely accepted that the observation of SF for $p$-$H_2$ hinges on the stabilization of a low-temperature liquid phase. Several attempts have been made [21, 22, 23, 24] to supercool bulk liquid $p$-$H_2$, but the experimental hurdles have thus far made it unfeasible to reach a temperature in the range where SF might be observed.

For non-bulk systems, computer simulations have yielded evidence of superfluid be-

[3]which is unstable against recombination - i.e. formation of hydrogen molecules, with an attendant release of energy, renders possible experimental observation of BEC only in highly-controlled settings [19]

havior in very small $p$-$H_2$ clusters [25, 26, 27, 28], and claims have been made of its actual experimental observation [29]. Considerable effort has also been devoted, in recent times, to the theoretical characterization of superfluid properties of solvating $p$-$H_2$ clusters around linear molecules, such as OCS [30, 31]. However, in Chapter 3, we show results for a system with a geometry which interpolates between that of such clusters and planar surfaces by investigating theoretically the properties of $p$-$H_2$ adsorbed on the exterior surface of comparatively large fullerene molecules. The physics of $p$-$H_2$ is found to be strongly two-dimensional, with $p$-$H_2$ always forming a solid; the attractive well depth of the fullerene molecule significantly enhances particle localization as well, further inhibiting quantum effects necessary for the observation of superfluidity.

Several other experimental avenues aimed at suppressing crystallization have been explored as well, including reduction of dimensionality. For example, the phase diagram and structure of thin $p$-$H_2$ films adsorbed on graphite and similar substrates have been studied extensively using various techniques [32, 33, 34, 35, 36, 37]. One of the most remarkable aspects [36] is that the melting temperature $T_m$ of a solid $p$-$H_2$ monolayer can be significantly less than bulk $p$-$H_2$.

There appears to be a limit, however, to what can be achieved by reduction of dimensionality alone. A theoretical study of the phase diagram of $p$-$H_2$ in two dimensions [38] has shown that the equilibrium phase of the system at low $T$ is a triangular crystal, with no evidence of even a metastable liquid phase at lower density. Indeed, the system remains solid all the way to the spinodal density. The melting temperature $T_{\rm m}$ of the equilibrium crystal is 6.8 K, i.e., approximately half that of bulk $p$-$H_2$ but still significantly higher than the temperature at which the system, if it remained a liquid, would turn superfluid, which is estimated to be roughly 2 K.

Later theoretical studies of $p$-$H_2$ adsorbed onto weakly attractive substrates predicted only a very slight reduction of $T_{\rm m}$ with respect to the purely 2D case, due to an enhancement of the kinetic energy arising from zero-point motion in the direction perpendicular to the substrate (for example, in the case of lithium [39], arguably one of the weakest substrates existing, a reduction of merely 0.3 K was observed). This suggests that mere reduction of dimensionality is not sufficient to stabilize a fluid phase of $p$-$H_2$ down to low enough a temperature for superfluidity to be observed.

In a recent neutron scattering investigation of $o$-$D_2$ films adsorbed on a krypton preplated graphite substrate [40], evidence of a stable "liquid-like" phase of $o$-$D_2$ down to $T \sim 1.5$ K was reported (termed a "domain-wall" fluid by the authors). This result is obviously of great interest, as it appeared that the substrate considered in this work may indeed provide an avenue to the observation of the long sought superfluid phase of molecular hydrogen, given the low temperature down to which a liquid-like phase may exist, in analogy with grain-boundary superfluidity in solid helium [41].

Motivated by this experiment, we have undertaken a theoretical study of the low temperature phase diagram of $p$-$H_2$ and $o$-$D_2$ films adsorbed on such a substrate, the results of which can be found in Chapter 4. In terms of superfluid properties, we summarize our findings by reporting that the null result is observed - particle localization is still far too pronounced, especially along the domain walls.

## 1.4 Supersolidity

Solid order may not, however, be entirely incompatible with superflow. So-called "supersolids", characterized by crystalline order and superfluidity, have been theorized and studied for more than 50 years [42, 43, 44, 45, 46, 47].

Like a superfluid, a supersolid should exhibit dissipationless mass flow through its (crystalline) structure. For a cartoon description of how this mass current could be manifested, liquid helium in a pipe would flow from one end of a supersolid plug (of arbitrary length) and emerge unimpeded from the other end, with unchanged momentum; in contrast, a regular solid helium plug would be impermeable to flow [48]. The effect could also be established using traditional torsional oscillator experiments by observing nonclassical rotational inertia (NCRI), with the superfluid fraction of the solid decoupling from any (slow) induced rotation. In both examples, one would need to confirm that the helium sample (or plug, in the former case) has uniformly solidified, with no percolating liquid channels capable of supporting liquid superflow.

Since defect-free crystals are incompatible with superfluidity [49], theories of supersolidity demand that the low-temperature crystal be incommensurate. As a consequence of their quantum behavior, point defects such as vacancies and interstitials can Bose con-

dense at low temperature, giving rise to superfluid properties.

An investigation of point-defects in solid $^4$He reveals that a uniform gas of defects is thermodynamically unstable against separation into a vacancy-rich phase, and a perfectly crystalline vacancy-free phase, with the vacancies forming clusters at all concentrations [50]. This line of investigation was later expanded to other systems with quenched disorder, such as extended defects, in $^4$He [41], revealing that some forms of incommensuration can lead to a metastable quantum phase supporting simultaneous diagonal and off-diagonal long-range order. In [51], it was shown that extended defects in $^4$He of the form of *screw dislocations* could support the formation of a bosonic Luttinger liquid with the property of quasi-one dimensional superflow. Similar simulations performed for $p$-$H_2$ yielded that the resulting dislocation core is insulating, precluding similar properties for molecular hydrogen in this geometry.

In quasi two dimensions, an interesting question is whether by "fine tuning" of a substrate, collective quantum many-body phenomena could become observable, in some thermodynamically stable low-temperature solid phase, with defects at equilibrium.

In 1997, Gordillo and Ceperley [52] (GC) proposed that a significant lowering of the equilibrium density of 2D $p$-$H_2$, and the ensuing stabilization of a low temperature "liquid" phase, could be achieved by embedding a $p$-$H_2$ fluid in a regular crystal of identical scatterers (e.g., foreign atoms or molecules), incommensurate with the equilibrium crystal structure of pure 2D $p$-$H_2$. Path Integral Monte Carlo (PIMC) simulations of such a model system yielded some evidence of a possible superfluid transition at $T \sim 1$ K. However, the size of the simulated system was very small (of order of 10 $p$-$H_2$ molecules). A subsequent PIMC study, comprising up to ten times as many particles, suggested that the $p$-$H_2$ actually forms a solid, and that the observation of a finite superfluid density is merely a finite-size effect (in that the system size utilized in the simulation could not convey the phase representative of the thermodynamic limit) [53].

A source of controversy for Ref. [53] is related to the inefficiency of explicitly sampling long permutations using PIMC, and that this inefficiency, which can manifest itself strongly in larger systems, could lead to *artificial* suppression of permutations, and thus generate false negatives for superfluid properties. In other words, the ergodicity problem associated with the intrinsic sampling inefficiency PIMC suffers from in this regard ren-

ders it difficult to decipher whether the vanishing of the superfluid signal for large systems is representative of the thermodynamic limit, or a symptom of the algorithmic limitations.

In Chapter 5, we report the results of a theoretical study which seeks to clarify this point of contention by repeating the simulations of Ref. [52] and Ref. [53] using an improvement of standard PIMC, the novel continuous-space *worm algorithm* (WA), which does not suffer from severe inefficiencies in the generation of permutation cycles.

## 1.5 Summary of Original Research

Altogether, the research represented by this thesis is a contribution to our physical understanding of 2D superfluid films, and the behavior, in particular, of 2D $p$-$H_2$ at low temperature. We have employed state-of-the-art computational techniques to uncover and clarify novel physics, with the following specific primary aims, as they relate to superfluid 2D films of molecular hydrogen:

1. to investigate the role of dimensionality in the quantum many-body properties of bosons.
2. to explore the role of incommensuration in the stabilization of liquids to low temperature.
3. to clarify the relationship between superflow and solid order in 2D.
4. to study the effect of introducing disorder on local and global properties of quantum films.

These points are addressed as follows.

### 1.5.1 Adsorption of *para*-Hydrogen on Fullerenes

Points **1** and **2** are first addressed by studying the adsorption of $p$-$H_2$ on the surface of fullerenes at $T$=0 K. Two models are adopted; the first treats each fullerene as a smooth spherical surface, interacting with $p$-$H_2$ with roughly the strength of a single plane of

graphite. Strong particle localization is observed, with the $p$-$H_2$ found to approximately recreate their 2D equilibrium configuration (a triangular lattice).

A second model, incorporating the corrugated structure of the fullerenes, is then studied in the hopes of introducing incommensuration (i.e. preventing the $p$-$H_2$ from forming their preferred structure by imposing a competing order). The equilibrium configuration of hydrogen in this case is, however, commensurate with the carbon-ring adsorption sites on the surface of the fullerene, with severe particle localization experienced by $p$-$H_2$. The $p$-$H_2$ is found to in general be compressible, with $p$-$H_2$ again attempting to recreate their equilibrium 2D configurations on the fullerene surface as the chemical potential is increased.

Being solids with a high degree of particle localization, these systems are thus not candidates for the observation of the superfluid phase of $p$-$H_2$. Secondary information gleaned is related to the structural and energetic properties of adsorbed $p$-$H_2$ on fullerenes, of some relevance to the field of hydrogen fuel storage.

This research was published in
Joseph Turnbull and Massimo Boninsegni. Physical Review B **71**, 205421 (2005).
Reprinted in Virtual Journal of Nanoscale Science and Technology **11**, 23 (2005).

### 1.5.2 Molecular hydrogen isotopes adsorbed on krypton-preplated graphite

Points **1** and **2** are again our focus here. We confirm that reduction of dimensionality alone is insufficient to extend the fluid state of $p$-$H_2$ to a low enough temperature for superfluidity to be observed. This is accomplished by studying the adsorption of $p$-$H_2$ on a graphite substrate preplated by a single atomic monolayer of Krypton atoms, which are *commensurate* with the underlying graphite, inspired by [40]. The idea is to adsorb $p$-$H_2$ upon a surface similar to graphite, but more weakly interacting.

We find that there are two stable phases of $p$-$H_2$, both solid; one is a monolayer commensurate with the Kr layer, while the other is an incommensurate monolayer, compressible within a small range of coverages. Quantum exchanges of hydrogen molecules are

suppressed in this system; altogether, our findings are similar to what is seen for $p$-$H_2$ on bare graphite.

A closely related system is next studied to probe a potential mechanism for inducing incommensuration. The krypton monolayer preplating the graphite substrate is instead compressed, following from additional structural information provided by the lead author of [40]. In reference [40], it is reported that $p$-$H_2$ with coverage above 1/2 filling adsorbed upon such a geometry displays fluid-like properties down to $T$=1.5 K. The hypothesis is that a particular range of densities of $p$-$H_2$ are accommodated by the formation of commensurate regions separated by heavy domain walls, and that the position of these domain walls is fluid.

Using an exact ground state technique, for both $p$-$H_2$ and $o$-$D_2$, we find that a solid monolayer commensurate with the Kr layer is thermodynamically stable, and, in both cases, is the coverage corresponding to the minimum energy per particle. For $o$-$D_2$, we also find that there are two distinct compressible incommensurate solid regions, with the denser region, IC-II, corresponding to regions of commensuration separated by domain walls. Investigation of this coverage region at finite temperature, using the worm algorithm, down to $T$=0.25 K, yields no evidence of superfluidity, consistent with our observation of a high degree of localization of $o$-$D_2$ molecules. No quantum exchanges are found to take place, though they are sampled efficiently.

Though our simulations are not inconsistent with the "domain-wall fluid" interpretation offered by Wiechert et al., this mechanism is not found to support superfluidity of either hydrogen isotope. Our interpretation is that, while incommensuration is achieved in the sense that the number of particles is greater than the number of adsorption sites on one sublattice of the substrate, particles along the domain walls are still roughly localized around the minima of the potential (by partially occupying the second of two sublattices), reducing zero-point motion sufficiently to suppress quantum many-body effects.

This research was published in

Joseph Turnbull and Massimo Boninsegni. Physical Review B **76**, 104524 (2007).
Joseph Turnbull and Massimo Boninsegni. Journal of Low Temperature Physics **140**, 269 (2005).

### 1.5.3 Supersolid hydrogen in two dimensions: incommensuration and disorder

Here we address points **1** through **4** in one systematic investigation inspired by ref. [52]. We first embed $p$-$H_2$ in a regular crystal of identical scatterers, incommensurate with the equilibrium crystal structure of pure 2D $p$-$H_2$, and study this system as a function of density, temperature, and impurity distribution.

For smaller systems with periodic arrays of impurities, we find that the equilibrium phase of $p$-$H_2$ is an arrangement roughly coextensive (a kagomé tiling) with the impurity background, with the apparent presence of a $\sim 10\%$ concentration of interstitials. We obtain a finite superfluid signal, thus observing an apparent coexistence of diagonal long-range order and off-diagonal quasi-long-range order, making the system consistent with definitions of a "supersolid".

In order to confirm that this system, in the thermodynamic limit, indeed supports superflow in $p$-$H_2$, we next study the structural properties of a much larger manifestation of the system, containing hundreds of impurities and $p$-$H_2$ molecules. The $p$-$H_2$ is found to form a perfect crystal with a large unit cell (having non-trivial structure), devoid of interstitials. Such a phase is most likely insulating [49]. Thus, we conclude that the above-reported superfluid properties are finite-size artifacts, and that $p$-$H_2$ in this geometry is a regular quantum solid in the thermodynamic limit. Increasing the coverage does not lead to the formation of an interstitial-rich phase, but rather to the coexistence of different commensurate phases, separated by domain walls.

The second part to this investigation focuses on the role of disorder, where our aim is to determine whether the above perfectly crystalline equilibrium phase could be weakly disrupted by the introduction of disorder, which could introduce a finite density of interstitials at equilibrium, and lead to long-range superfluid coherence. Disorder is known to cause localization, with the ensuing *disappearance* of SF in a system of hard core bosons [54]. However, recent numerical work has yielded evidence of a possible "superfluid glassy" phase of condensed helium, characterized by simultaneous broken translational invariance (and therefore nonzero shear modulus) *and* SF, with no diagonal long-range order [55]. It is conceivable that a similar phase of $p$-$H_2$ could arise in disorder.

For sufficiently strong disorder, even though we observe exchanges of small groups of molecules, they have a local character, i.e., long permutation cycles spanning the entire system do not occur; as a result, a finite superfluid signal never materializes in the low temperature limit even for relatively small systems. We observe a glassy phase, but we also clearly observe that $p$-$H_2$ molecules *locally* attempt to recreate the triangular lattice structure associated with bulk 2D $p$-$H_2$ at equilibrium [38], only interrupted by the underlying impurity matrix.

For weak disorder, starting from a minor random displacement of the background impurities found to not disrupt the perfect crystalline state of $p$-$H_2$, the magnitude of the random displacements is increased to the point where the crystal structure of $p$-$H_2$ is disrupted and interstitials form part of the equilibrium phase, and all trace of off-diagonal quasi-long-range order is destroyed.

A manuscript of this research has been submitted for publication to Physical Review B (see ArXiv:0807.2210).

Altogether, we find strong evidence suggesting that reduction of dimensionality, incommensuration, and imposed disorder, alone or in conjunction, cannot stabilize a superfluid or supersolid state of bulk 2D $p$-$H_2$. The prognosis for observing superfluidity in bulk 2D $p$-$H_2$ thus appears to be poor. Absent some mechanism to directly renormalize (weaken) $p$-$H_2$-$p$-$H_2$ interactions, the propensity of bulk $p$-$H_2$ to crystallize rules out the observation of bulk hydrogenic superfluidity even in 2D.

# Chapter 2

# Physical Model, Methodology, and Simulation

In this chapter, the approach used to study the systems of interest is developed. We begin by stating the general form of the systems under investigation (i.e. defining the many-body Hamiltonian), and then framing the precise problem for which solutions are sought. Our procedures for constructing exact solutions to these problems are then explained; this entails a brief discussion of the general path integral formalism, as well as a description of one zero-temperature incarnation of the formalism (path-integral ground-state algorithm) and a recently developed extended configuration space method (the worm algorithm) for continuous Bose systems at finite-temperature. Included is a discussion of the configuration space sampling techniques, as well as the procedures used for calculating observables.

In later sections, we discuss technical details related to error estimation, the forms of the intermolecular potentials assumed, as well as a selection of other topics pertinent to our simulations.

## 2.1 Formalism

For a quantum-mechanical system of $N$ particles in thermal equilibrium at temperature $T$, we wish to obtain thermal averages for physical observables which are diagonal in the

coordinate representation as

$$\langle O \rangle = \frac{\sum_s O(s) e^{-\beta E_s}}{\sum_s e^{-\beta E_s}} \tag{2.1}$$

where the sum is taken over all $s$ configurations, $\beta = 1/T$, $e^{-\beta E_s}$ is proportional to the probability of the system occupying state $s$, and $O(s)$ is the value of the physical observable $O$ for state $s$ [56]. Here, we define a *state* to be one of an infinite number of unique definite-energy many-body wavefunctions, $\Psi_E(\mathbf{r}_1, \mathbf{r}_2, ..., \mathbf{r}_N)$, where $\mathbf{r}_i$ are the positions of the $N$ particles comprising the system.

The wavefunctions $\Psi_E$ are quantum-mechanical objects satisfying the many-body Schrödinger equation for our system

$$-\hbar^2 \sum_{k=1}^{N} \frac{1}{2m_k} \nabla_k^2 \Psi_E + V(\mathbf{r}_1, \mathbf{r}_2, ..., \mathbf{r}_N) \Psi_E = E \Psi_E \tag{2.2}$$

where $\hbar$ is Dirac's constant (in the units used herein, this constant is given by 7.64 x $10^{-12}$ K s), $m_i$ is the mass of particle $i$, and $V(\mathbf{r}_1, \mathbf{r}_2, ..., \mathbf{r}_N)$ is the total potential energy associated with the configuration of $N$ particles at positions $(\mathbf{r}_1, \mathbf{r}_2, ..., \mathbf{r}_N)$, with $V$ depending only upon the position of all particles. We also note that, in this thesis, all energies have been divided by Boltzmann's constant, $k_B$, (thus energies will have units of kelvins, K).

If $\Psi_E$ is normalized such that

$$\int d\mathbf{r}_1 d\mathbf{r}_2 ... d\mathbf{r}_N \, |\Psi_E(\mathbf{r}_1, \mathbf{r}_2, ..., \mathbf{r}_N)|^2 = \int dP(\mathbf{r}_1, \mathbf{r}_2, ..., \mathbf{r}_N) = N \tag{2.3}$$

we can associate $dP$ with a probability density. In general, $\Psi$ is unknown.

For the sake of notational convenience, we will introduce the short-hand notation $R \equiv \mathbf{r}_1, \mathbf{r}_2, ..., \mathbf{r}_N$ as a collective coordinate of the $N$ particles. It is convenient also to rewrite (2.2) in a more compact form as $\hat{H}\Psi_E(R)$=$E\Psi_E(R)$, where

$$\hat{H} \equiv -\hbar^2 \sum_{k=1}^{N} \frac{1}{2m_k} \nabla_k^2 + V(\mathbf{R}) \tag{2.4}$$

is referred to as the Hamiltonian operator, which is a sum of a kinetic energy operator $\hat{H}_0$ and a potential energy operator $\hat{V}$. For an arbitrary function $F$, we next make use of the formal relation $F(\hat{H})\Psi_E(R) = F(E)\Psi_E(R)$, to define the density matrix

$$\begin{aligned}\rho(R,R',\beta) &= \sum_E e^{-\beta E}\Psi_E^*(R')\Psi_E(R) \\ &= \sum_E \Psi_E^*(R')e^{-\beta\hat{H}}\Psi_E(R) \\ &= \left\langle R\left|e^{-\beta\hat{H}}\right|R\right\rangle\end{aligned} \tag{2.5}$$

where we have taken $F=F(\hat{H})=e^{-\beta\hat{H}}$ [56]. Using the above formalism, one can now rewrite (2.1) as

$$\begin{aligned}\langle O\rangle &= \frac{\sum_E e^{-\beta E}\int dR\, O(R)\,|\Psi_E(R)|^2}{\sum_E e^{-\beta E}\int dR\,|\Psi_E(R)|^2} \\ &= \frac{\int dR O(R)\rho(R,R,\beta)}{\int dR\rho(R,R,\beta)} \\ &= \frac{1}{Z}\int dR\, O(R)\,\rho(R,R',\beta)\end{aligned} \tag{2.6}$$

where $Z$ denotes the canonical partition function, $Z=\int dR\ \rho(R,R',\beta)$. While simply offering a reformulation of the original expression for thermal averages of observables, the density matrix formalism naturally lends itself to an elegant method of solution which computer simulations can tackle without recourse to approximation.

Upon applying the operator $\partial/\partial\beta$ to (2.5), one obtains

$$\frac{\partial\rho(R,R',\beta)}{\partial\beta} = -\sum_E e^{-\beta E}\ E\ \Psi_E^*(R')\Psi_E(R) = -\hat{H}\rho(R,R',\beta) \tag{2.7}$$

which is Bloch's equation, and we are reminded that $\hat{H}=\hat{H}_0+\hat{V}$. In the high-temperature limit $\beta\to 0$, we have $\rho(R,R',\beta)=\sum_E \Psi_E^*(R')\Psi_E(R)$ [56]. Thus, by the completeness property of the eigensolutions to (2.2), we must have that $\rho(R,R',0)$ is independent of $\hat{V}$ for any $N$-particle system; if we know the solution for one $\hat{V}$, we know that it will be a solution for any other $\hat{V}$ in the limit of low $\beta$. This is an intuitive result, as at very high temperatures, any system will behave as a non-interacting gas. We will use this property to construct an initial condition for Bloch's equation.

In general, we know neither $\{\Psi_E(R)\}$ nor $\rho(R,R,\beta)$ for our given $\hat{H}$. The simplest case for which an exact analytical calculation of the density matrix is known is for a

system of free particles. For one particle in D-dimensions, a direct solution of (2.2) and some algebra yields

$$\rho_f(\mathbf{r},\mathbf{r}',\beta) = \frac{\exp\left[-\frac{m(\mathbf{r}-\mathbf{r}')^2}{2\hbar^2\beta}\right]}{\left(2\pi\hbar^2\beta m^{-1}\right)^{D/2}} \tag{2.8}$$

For a system of $N$ distinguishable non-interacting particles, one obtains a simple decoupling, which leads to the solutions of (2.2) given by an $N$ term product of (2.8) [56]. The free particle density matrix for the entire system is thus given by

$$\rho_F(\mathbf{r},\mathbf{r}',\beta) = \prod_{i=1}^{N} \frac{\exp\left[-\frac{m_i(\mathbf{r}_i-\mathbf{r}_i')^2}{2\hbar^2\beta}\right]}{\left(2\pi\hbar^2\beta m_i^{-1}\right)^{D/2}} \tag{2.9}$$

As $\beta \rightarrow 0$, we know from the above that the value of the free-particle density matrix must coincide with the value of the general density matrix, i.e. $\rho(R,R',0) \equiv \rho_F(R,R',0)$ [56]. This is our sought initial condition.

Upon integrating both sides of (2.7) from 0 to $\beta$, we obtain

$$\rho(R,R',\beta) = \rho_F(R,R',0) - \int_0^\beta d\tau\ \hat{H}\ \rho(R,R',\tau) \tag{2.10}$$

which we then use to construct a formal expansion for the density matrix in powers of $\beta$ by feeding (2.10) iteratively into itself. Upon the evaluation of the resulting nested multidimensional integrals, we obtain

$$\rho(R,R',\beta) = \sum_{n=0}^{\infty} \frac{(-1)^n\beta^n\hat{H}^n}{n!}\rho_f(R,R',0) \equiv e^{-\beta\hat{H}}\rho_F(R,R',0) \tag{2.11}$$

which is a formal, though not yet useful, expression for the density matrix [56]. In order to make the evaluation of (2.11) tractable, we make use of the formal identity

$$e^{-\beta\hat{H}} \equiv \left(e^{-\tau\hat{H}}\right)^M \tag{2.12}$$

where $\beta$=$M\tau$. We refer to $\tau$ in this context as *imaginary time*, since the exponential in (2.12) has the same mathematical structure as the quantum-mechanical imaginary-time evolution operator. Replacing the corresponding term in (2.5) with the expression in (2.12), we obtain

$$\rho(R,R,\beta) = \left\langle R \left| \underbrace{e^{-\tau\hat{H}} e^{-\tau\hat{H}} \cdots e^{-\tau\hat{H}}}_{M \text{ times}} \right| R \right\rangle$$
$$= \int dR_1 dR_2 \cdots dR_{M-1}\, \rho(R,R_1,\tau)\rho(R_1,R_2,\tau)\cdots\rho(R_{M-1},R,\tau) \tag{2.13}$$

Upon fixing $\beta$, one can see, in the limit of large $M$ and small $\tau$, we have that $\rho(R,R',\tau)$ approaches the free-particle limit of the density matrix given by (2.9), and one obtains, to $O(\tau^3)$

$$\rho(R,R',\tau) \approx \rho_F(R,R',\tau)e^{-\tau V(R)} \tag{2.14}$$

which is exact for any finite $\beta$ only in the limit $\tau \to 0$ (i.e. $M \to \infty$); we will use this approximation explicitly in the following section. Following from reference [57], upon taking this limit and expressing (2.6) in terms of (2.14), one can recover an exact expression for expectation values of diagonal operators within this formalism as

$$\langle O \rangle = \frac{\int \mathcal{D}R(\tau)\, O(R(\tau))e^{-\mathcal{S}[R(\tau)]}}{\int \mathcal{D}R(\tau)\, e^{-\mathcal{S}[R(\tau)]}} \tag{2.15}$$

where the functional integrals are performed over all continuous many-particle configurations $R(\tau)$ constrained by $R(\beta)$=$R(0)$ ($\beta$ periodicity) where $0 \leq \tau \leq \beta$ (this is in contrast with classical mechanics, where the system follows only one specific $R(\tau)$ - the one corresponding to a stationary action [56]) and where the Euclidean action functional $\mathcal{S}[R(\tau)]$ is given by

$$\mathcal{S}[R(\tau)] = \int_0^\beta d\tau \left\{ \frac{m}{2\hbar^2} \sum_{k=1}^{N} \left( \frac{dr_k}{d\tau} \right)^2 + V(R(\tau)) \right\} \tag{2.16}$$

where the integrand is the total energy associated to each point along the path, an object which resembles the classical Lagrangian, but differs by the sign of the second term.

An important detail not yet discussed is related to quantum statistics. Namely, in our preceding analysis, we have implicitly assumed that the particles are distinguishable (in the sense that one could label a particle at some generalized set of coordinates $\mathbf{t}$, and track its evolution through coordinate space, as one can do in classical mechanics). For the quantum systems we study here, the indistinguishable character of particles must be

taken into account in order to properly capture the physics we are interested in, and this necessitates that our many-body wavefunction for the $N$ identical particles exhibits well defined properties under the coordinate permutation of any two particles.

Because the many-body wavefunction $|\Psi(R_1, R_2, \cdots, R_N)|^2$ is physically associated with a probability density of positions of identical particles, $\Psi$ must necessarily change only by a phase factor upon particle permutation (the configuration in which any two particles are permuted must in no way be physically different than the system prior to the permutation). This requirement is inherited by the formalism by requiring that

$$\Psi(R_1, R_2, \cdots, R_i, \cdots, R_j, \cdots, R_N) = \eta\Psi(R_1, R_2, \cdots, R_j, \cdots, R_i, \cdots, R_N) \quad (2.17)$$

where $\eta$ is a complex number with magnitude one [56], which in principle could be any number of the form $e^{i\theta}$ (in the case of two-dimensional quasiparticle excitations called *anyons*, any complex phase is indeed possible), the spin statistics theorem [58] instead provides the restriction that $\eta$=$\pm$1. Particles for which $\eta$=1 are called bosons, and have integer spin, while particles for which $\eta$=-1 are called fermions, and have half-integer spin.

This (anti) symmetry property is expressed by the density matrix as well (which is nothing but a bilinear combination of products involving these many-particle wavefunctions), and for a system of identical particles undergoing P permutations, we must have that,

$$\rho(R, PR', \beta) = \eta^{\mathrm{P}}\rho(R, R', \beta) \quad (2.18)$$

and our thermal averages must be summed over all possible permutations of the $N$ particles. While in the case of fermions, the anti-symmetry property spawns an entire class of (in general, intractable by Monte Carlo methods - the problem arises from averaging of equal magnitude contributions of positive and negative sign for the thermal expectation values, with these sign differences arising via particle permutations; the signal becomes swamped by statistical noise) difficulties because of the nature of the numerical procedure employed in the calculation of thermal averages (a discussion of which is outside the scope of this thesis), the symmetry property for bosonic systems can be incorporated

without difficulty or the introduction of systematic errors [56]. It is reiterated that an accurate generation and accounting of such permutations is *necessary* in order to properly capture the physical properties (such as superfluidity) we are interested in.

## 2.2 Path Integral Monte Carlo

As a direct analytical calculation of (2.15) is out of the question for systems with non-trivial Hamiltonians, we will use an $M$-discretized form of (2.15) in our calculations, making $R(\tau)$ discontinuous, and using some approximation of the density matrix.

Direct interpolative quadrature at this level is out of the question, as the immense multidimensional character of the problem ($D \times N \times M$, for a $D$-dimensional system of $N$ particles with $M$ discretization points of $\beta$) makes such an approach scale unfavorably. Indeed, the large number of coupled degrees of freedom inherent to the problem renders viable only one approach, Monte Carlo integration. The sampling of the vast configuration space is then performed stochastically. This *path integral Monte Carlo* (PIMC) prescription can be very robust, offering the ability to obtain results at arbitrary precision by increasing $M$.

We proceed, for convenience, by denoting by $X = \{R_0, R_1, \cdots, R_{M-1}, R_M\}$ the many-particle path consisting of the full set of configurations $R_i$ across the $M$ imaginary time intervals. In this notation, we can write thermal expectation values in the compact form

$$\langle O \rangle \approx \frac{\int dX\ O(X)\ P(X)}{\int dX\ P(X)} \tag{2.19}$$

where we must impose the $\beta$-periodicity and particle-permutation constraints, given by $\mathrm{P}(R_M)$=$R_0$, and where $P(X)$, the exponential of the discretized Euclidean action (which has the mathematical structure of a probability distribution) [56], is given by

$$P(X) = e^{-U(X)} \prod_{i=0}^{M-1} \rho_f(R_i, R_{i+1}, \tau) \tag{2.20}$$

where we have some freedom in our choice of $U$, being constrained only by the requirement of recovering the exact thermal expectation value given by (2.15) in the limit as

$\tau \to 0$. For the purposes of this discussion, we can use the form of $U$ suggested by equation (2.14), namely

$$U(X) = \tau \sum_{j=0}^{M-1} V(R_j) \tag{2.21}$$

which satisfies the constraints imposed above. We note that in our calculations we adopt a different form of $U(X)$, which permits the use of fewer $M$ steps ("slices") in imaginary-time to achieve the same accuracy, the expression for which can be found in reference [59].

The core PIMC procedure is then to accumulate statistics for the computation of (2.19) by generating a large number of independent (uncorrelated) many-particle paths $\{X_i\}$ randomly drawn from the distribution $P(X)$, averaging the obtained $\hat{O}$ for each independent path [56]. An example configuration of one many-particle path is shown in Figure 2.1.

### 2.2.1 Path Sampling

How does one go about generating the set of many-particle paths $\{X_0, X_1, ...\}$? A particularly efficient method is to employ the Metropolis algorithm, in which a Markov chain is used to generate a random walk through path space. A transition rule $\Gamma(X \to X')$ depending only on the initial state $X$ guides this random walk, with a goal of sampling paths with a probability proportional to $P(X)$ in such a way that the random walk is ergodic (i.e. that all configurations are equally accessible in the infinite-sampling limit). We can guarantee ergodicity as well as the convergence to $P(X)$ by imposing the following detailed balance condition

$$P(X)\Gamma(X \to X') = P(X')\Gamma(X' \to X) \tag{2.22}$$

in which $\Gamma(X \to X')$ is expressed as product of two terms

$$\Gamma(X \to X') = Y(X \to X')A(X \to X') \tag{2.23}$$

where $Y(X \to X')$ is the sampling distribution determining how transitions between state $X$ and $X'$ are sampled [56], while $A(X \to X')$ is the acceptance probability for the

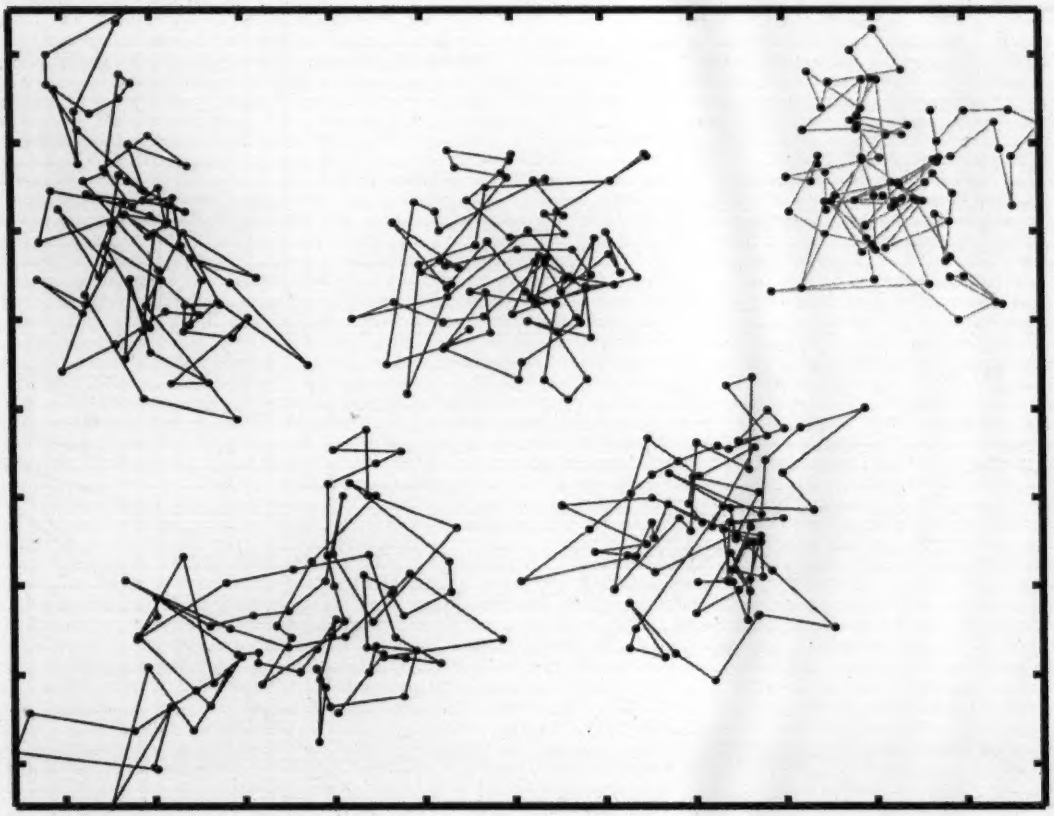

Figure 2.1: An example configuration of $N$=5 particles at $T$=1 K. Each dot denotes a single imaginary-time bead, of which there are $M$=80 for every particle. The spread of each particle gives a rough measure of the quantum zero point motion. Distance between tics is 1 Å.

particular attempted transition. To ensure that our $A(X \rightarrow X')$ satisfies detailed balance for any $Y(X \rightarrow X')$, we must have that

$$A(X \rightarrow X') = \min\left\{1, \frac{Y(X' \rightarrow X)P(X')}{Y(X \rightarrow X')P(X)}\right\} \tag{2.24}$$

which permits us to select an arbitrary form for $Y$, and in practice we will choose a form which leads to efficient sampling.

Beginning from an $X_i$ many-particle configuration in path space, the very general sampling prescription is as follows. We construct a new trial path $X_j$ by sampling updates to the positions of one or more particles over some number of imaginary-time slices according to $T(X_i \rightarrow X_j)$. For this trial update, we then compute the acceptance probability $A(X_i \rightarrow X_j)$, and draw a uniform [0,1) random number $\alpha$. If $A(X_i \rightarrow X_j) \leq \alpha$, we reject the move and sample a different trial update starting anew from $X_i$. If $A(X_i \rightarrow X_j) > \alpha$, then we accept the trial update, setting $X_{i+1}$=$X_j$ [56].

A set of efficient update procedures defining $Y$ are essentially accepted as standard for conventional PIMC; see for example References [60, 61]. In this work, while making some use of the traditional trial update forms, we employ a variation of PIMC with an extended configuration space and an expanded suite of general trial updates. We will focus on this novel approach in the next section.

## 2.3 Extended Configuration Space: Worm Algorithm

In conventional PIMC, the entire configurational space is represented by a collection of closed ($\beta$-periodic) paths, each path associated with one particle. These closed world-line configurations, being diagonal, contribute to the partition function, so we refer to the space occupied by all such configurations as the *Z-sector*.

### 2.3.1 Motivation

A serious flaw with conventional PIMC is that it suffers from an exponential decrease in efficiency when sampling long permutation cycles (quantum exchanges) for an increase of particles $N$ and/or imaginary-time slices $M$. This inefficiency comes about because

permutational cycles involving groups of particles are sampled directly by cutting and reconnecting pairs (or triplets, etc) of world-lines in such a way that permutations occur while remaining in the $Z$-sector. For weakly interacting particles, this procedure gives reasonable sampling efficiency. However, for particles interacting via a potential with a repulsive core (a feature of any realistic potential describing the interaction between atoms or molecules), the reconstruction of world-line segments inevitably will involve bringing two particles within their hard-core distance, with an associated increase of the potential energy. Permutations in such a scenario will thus suffer a low acceptance rate, with the problem being particularly serious when more than two particles are involved in a permutational exchange.

This problem is a critical issue in the simulation of systems for which the observation of phenomena such as Bose-Einstein condensation and superfluidity are sought, as quantum exchanges underpin these effects - in particular quantum exchanges involving large numbers of particles. Even a two to three order magnitude increase in computational power enjoyed over the last two decades has not permitted systems with greater than 64 particles to be probed in relation to the superfluid properties. The difficulty is compounded by the fact that, in such PIMC simulations, the absence of permutational exchange cycles can reflect either a real physical effect or an inefficiency in the path sampling routine - this assessment can be impossible to perform with confidence.

A recent reformulation of PIMC, called the *worm algorithm* (WA) has been found which completely overcomes these problems. Borne of conceptually similar techniques used in quantum lattice models, the WA generates all possible many-particle permutations through a sequence of local single-particle updates. The updates - called "swaps" - take place for configurations sampled outside the $Z$-sector, and do not require any two particles involved in a permutation to be brought within the hard-core radius of their interatomic potential. As no potential energy penalty is involved, this update can enjoy a very high acceptance rate. The structure of the updates, as we shall see, also permits us to sample only two-particle permutations, since arbitrarily long permutation cycles can be constructed through a sequence of these two-particle exchanges.

The continuous-space worm algorithm, first described in References [62, 63], operates in an extended configuration space which includes the $Z$-sector as a subspace, as well as

configurations with *open* world-lines, called "worms". These worm configurations are not diagonal, thus do not contribute to the partition function; however, they contribute to a similar object called the *one-particle Matsubara Green function*, which in second quantized Matsubara representation is given by,

$$G(r,\tau) = \left\langle \mathcal{T} \left\{ \hat{b}_{r'+r}(\tau)\, \hat{b}^{\dagger}_{r'}(\tau = 0) \right\} \right\rangle \tag{2.25}$$

where $\mathcal{T}$ is the time-ordering operator, $-\beta/2 \leq \tau \leq \beta/2$, $\hat{b}_r(\tau)$ is the Bose particle annihilation operator, and $\hat{b}^{\dagger}_r(\tau)$ is the Bose particle creation operator. The zero-time limit of (2.25) is the one-body density matrix, $n(r)$. If $G(r,\tau)$ and $n(r)$ decay exponentially in $r$, we note that the system is necessarily not superfluid. Like the energy, the temperature dependence of $G(r,\tau)$ can be used also to infer if one is probing the system's ground-state.

Configurations including worms occupy what is referred to as the $G$-sector, with the ends of a worm, which for historical reasons are referred to as *Ira* (the head), and *Masha* (the tail), sampled as to permit traversals in space and imaginary-time.

To go from a configuration in the $Z$-sector to a configuration in the $G$-sector, one must sample and then accept an opening of a closed world-line. Similarly, to go back from a configuration in the $G$-sector to a configuration in the $Z$-sector, one must sample and then accept a closing of the worm. The worm algorithm can be constructed in either the canonical or the grand-canonical ensemble, the latter introducing particle number fluctuations through the creation and annihilation of worms. In our implementation, $Z$-sector configurations are constrained in particle number $N$ (i.e. canonical simulations), and all $G$-sector configurations have a single worm, plus $N-1$ closed world-lines.

### 2.3.2 Worm Sampling

This section follows from References [62, 63]. In the following, we label the imaginary-time coordinate with the index $i$ (which ranges from "bead" 0 to $M-1$), and the particles with an index $k$. Consider a many-particle configuration $X$, which in general can include a worm, assigned a statistical weight $W(X,\tau)e^{-U(X)}$, where

$$W(X,\tau) = \prod_{i=0}^{M-1} \rho_f(R_i, R_{i+1}, \tau) \tag{2.26}$$

where $\rho_f$ is defined by (2.9), and we note that $W(X,\tau)$ must coincide with (2.20).

We sample this configuration space using the following suite of elementary ergodic updates, divided into three classes:

1. Open/close updates (complementary pair)

2. Advance/recede updates (complementary pair)

3. Particle swap (self-complementary)

Starting from a state in the random walk through configuration space for which the many-particle path $X_1$ is in the $Z$-sector, we can sample an *open* update for the random world-line associated with particle $k$ by attempting to remove its beads with indices $(M-\gamma) < i < M-1$ ($\gamma$ chosen at random, subject to the constraint $2 < \gamma \leq \gamma_{max} < M$, with $\gamma_{max}$ chosen to optimize the sampling efficiency). We associate Ira with the bead at index $M-\gamma$ and Masha with the bead at index $M-1$ (the last bead, which we will assume is the position of Masha in all following discussions). Our acceptance probability for the new $G$-sector configuration $X_2$ given by

$$A_{\text{open}} = \min\left\{1, \frac{Ce^{U(X_1)-U(X_2)}}{\rho_f(r_{\text{Ira}}, r_{\text{Masha}}, (\gamma-1)\tau)}\right\} \tag{2.27}$$

where the arbitrary constant $C$ can be used to control the relative proportion of time spent in the $G$ and $Z$ sectors.

Similarly, when starting from a configuration in the $G$ sector such that the number of imaginary-time slices between Ira and Masha is $\zeta - 1$, with $1 \leq \zeta < \gamma_{\text{max}}$, we can produce a trial update consisting of the creation of $\zeta - 1$ intermediate beads connecting the worm ends (thereby rendering the configuration diagonal) by sampling directly from the product of $\zeta$ free-particle propagators, $\prod_{i=1}^{\zeta} \rho_f(r_{i-1}, r_i, \tau)$. In order for the open/close complementary pair to satisfy detailed balance, the probability of accepting the close move must be given by

$$A_{\text{close}} = \min\left\{1, \frac{e^{U(X_1)-U(X_2)}}{C}\rho_f(r_{\text{Ira}}, r_{\text{Masha}}, (\gamma-1)\tau)\right\} \tag{2.28}$$

with the configuration returning to the $Z$-sector if the attempt is accepted.

Instead of closing the worm, a pair of $G$-sector trial updates can be attempted in which the head, Ira, can move forward or backward in imaginary-time. Let $i$ be the current position of Ira, where $0 \leq i \leq M-1$. In an attempted *advance* move of the worm, we generate a random number $\gamma$ subject to $\gamma \leq M-1-i$ which determines the number of new imaginary-time beads we will generate according to the product of $\gamma$ free-particle propagators $\prod_{i=1}^{\gamma}\rho_f(r_{i-1}, r_i, \tau)$. For a *recede* move, we draw a random integer number $\zeta < M-i-1$, and starting from bead Ira, we eliminate $\zeta$ imaginary-time beads. The acceptance probabilities for advance and recede moves are both given by the expression,

$$A_{\text{advance}} = A_{\text{recede}} = \min\left\{1, e^{U(X_1)-U(X_2)}\right\} \tag{2.29}$$

except in two cases where Ira and Masha are adjacent; if Ira=0, no recede move may be attempted, and if Ira$= M-2$, no advance move may be attempted.

The remaining move in our suite of $G$-sector updates is *swap*, which involves the permutation of particles. Consider all closed world-lines intersecting imaginary-time slice $(j+m)$ and select one of them, which we will call $C$, with probability $T_C = \Theta_j^{-1}\sum_i \rho_f(r_{A,i}, r_{C,i+m}, m\tau)$ where

$$\Theta_j = \sum_l \rho_f(r_{A,i}, r_{l,i+m}, m\tau) \tag{2.30}$$

which is rejected as a trial move if the world-line selected contains Masha at some time slice $w$ such that $i \leq w \leq i+m$. A set of random trial positions given by $\{r_{A,i+1}, \ldots, r_{A,i+m-1}\}$ is generated precisely the same way as in the *close* move described previously, while the set of imaginary-time slices $\{r_{C,i+1}, \ldots, r_{C,i+m-1}\}$ are erased (in analogy with *open* moves). The entire swap move is then accepted with probability $A_{\text{swap}} = \min\left\{1, e^{U(X)-U(X')}\Theta_A/\Theta_C\right\}$

If the swap is accepted, Ira is shifted from $r_{A,i}$ to $r_{C,i}$, while world-line $A$ reconnects with world-line $C$, implying a relabeling as illustrated in figure 2.2.

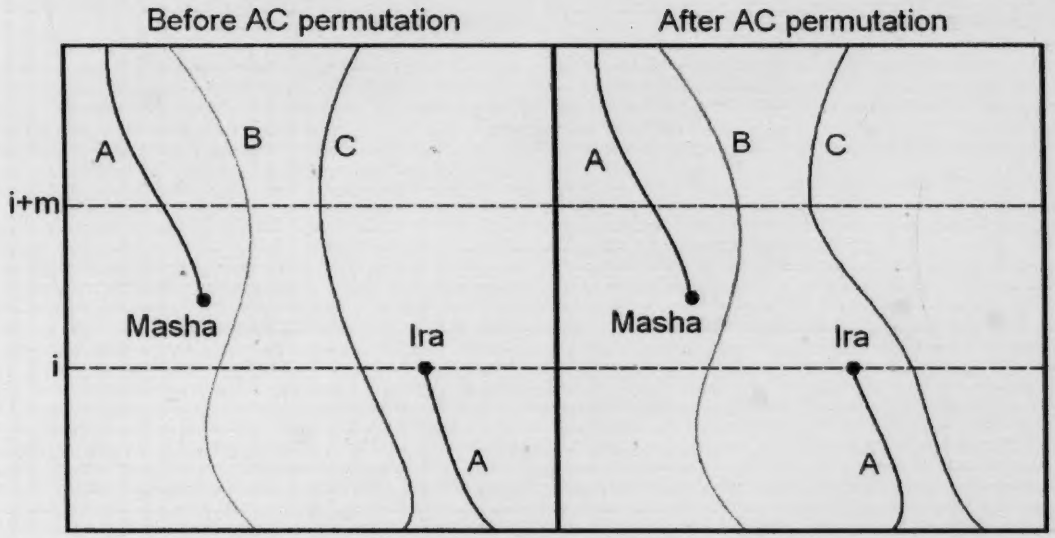


Figure 2.2: Swap move between world-lines $A$ and $C$ between imaginary-time slices $i$ and $i + m$, as described in the text. World-line $B$ is a spectator for this swap process.

### 2.3.3 The Return on Investment

Upon the development of the worm algorithm, several showcase systems were immediately studied, including liquid $^4$He in both two and three dimensions [62, 63], with systems encompassing thousands of bosons (two orders of magnitude greater than system sizes capable of being accurately studied using traditional PIMC), as well as simulations performed to elucidate the role of vacancies and extended defects in solid $^4$He, for systems with tens of thousands of bosons [41, 50, 51, 55].

Numerical results with unsurpassed accuracy have been reported in the above studies, as well as results describing phenomena beyond the reach of earlier QMC approaches. The extension of the configuration space to the $G$-sector also permits the explicit and exact computation of imaginary-time off-diagonal correlations not available to *any* other continuous-space QMC technique.

### 2.3.4 Physical Estimators

This section is derived from References [56, 61, 62, 63].

Using efficient schemes to sample the phase-space of quantum many-body systems forms the backbone of our simulations. What we are ultimately interested in, however, is the computation of physical observables, such as those encapsulating energetic and structural information, as well as imaginary-time correlations and estimates of quantities such as the superfluid density.

We calculate structural information such as pair-correlation functions, denoted by $g(r)$, which measure the relative probability of finding two particles at a distance $r$ from each other, using standard histogramming. A related quantity, the static structure factor $S(q)$ (which can be accessed directly in experiments using neutron or x-ray scattering, and thus has utility in direct comparisons), can then be obtained as the Fourier transform of $g(r)$. These spatial correlation functions provide important information related to thermal and quantum phase transitions.

In order to estimate the total energy, we take advantage of the thermodynamic identity

$$\langle E \rangle = -\frac{1}{Z}\frac{\partial Z}{\partial \beta} \tag{2.31}$$

with the partition function $Z$ for $N$ particles in $D$ dimensions with each world-line consisting of $M$ imaginary-time slices expressed in path integral notation as

$$\begin{aligned} Z_M = & \frac{1}{(4\pi\lambda\tau)^{DNM/2}} \int dR^0 \cdots dR^{M-1} \times \\ & \exp\left[\sum_{i=0}^{M-1}\sum_{k=1}^{N} \frac{r_k^i - r_k^{i+1}}{4\lambda\tau}\right] \exp\left[-\tau \sum_{i=0}^{M-1} V(R^k)\right] \end{aligned} \tag{2.32}$$

which becomes exact in the limit as $M \to \infty$ if we use the expression for $U$ in (2.20) given by (2.21). Here, $\lambda = \frac{\hbar^2}{2m}$. By plugging (2.32) into (2.31), we can compute energies per particle $e(N)$=$K(N)$+$V(N)$ using the resulting estimator given by

$$e(N) = \frac{\langle E \rangle}{N} = \frac{D}{2\tau} - \frac{\left\langle (r_k^i - r_k^{i+1})^2 \right\rangle}{4\lambda\tau^2} + \frac{\langle V \rangle}{N} \tag{2.33}$$

Recalling that $\tau = \frac{\beta}{M}$ has units of inverse temperature, the third term in the above expression can be readily identified as the thermal average of the potential energy $V$ per particle, with the remaining two terms being necessarily associated with the kinetic energy

$K$ per particle. The first term herein is the classical kinetic energy, and the second term corresponds to the average square displacement that a particle's beads in imaginary-time experience from the center of mass of the particle, which gives a measure of the particle's zero point motion (a reflection of the Heisenberg uncertainty principle). As required, when we take $\lim_{M\to 1}$ of (2.33), the expression for $K$ reduces to its classical value.

In order to obtain dependable results, in particular for the energy, one must perform a series of independent simulations varying only by the number of slices, $M$, and extrapolate from these estimates the $M \to \infty$ limit (i.e. $\tau \to 0$), typically by fitting the results by an expression of the form $J(\tau) = c_1 + c_2\tau^4$.

Another quantity we are interested in is the superfluid density, a property experimentally characterized in terms of the response of a system to the movement of its boundaries. Assume we have a cylinder filled with a liquid cooled to some very low temperature. If a rotation of the cylinder about its axis is induced, a normal fluid will be dragged along with the surface of the container, regardless of the speed of rotation. A superfluid, however, will remain at rest if the container rotates slower than some critical velocity. Following from Reference [61], the effective moment of inertia (i.e. the work needed to induce an infinitesimally slow rotation) is given by

$$I = \left.\frac{dF}{dw^2}\right|_{w=0} = \left.\frac{d\langle \mathcal{L}_z\rangle}{dw}\right|_{w=0} \tag{2.34}$$

where $F$ is the free energy, and $\mathcal{L}_z$, the total angular momentum operator in the axial direction ($\hat{z}$) of the cylinder, is given by

$$\mathcal{L}_z = i\hbar \sum_{k=1}^{N} \frac{\partial}{\partial\theta_k} \tag{2.35}$$

where $\theta_k$ is the angle of the $k$th particle of mass $m$ in cylindrical coordinates. The ratio of (2.34) to the classical moment of inertia, $I_c$, is defined as the normal density $\rho_n$, and anything remaining is the superfluid density $\rho_s$ (where $\rho_s + \rho_n = \rho$, the total density), defined as

$$\frac{I}{I_c} = \frac{\rho_n}{\rho} = 1 - \frac{\rho_s}{\rho} \tag{2.36}$$

and following from the derivation given in Reference [61], one can express

$$\frac{\rho_s}{\rho} = \frac{2m\langle A_z^2\rangle}{\beta\lambda I_c} \tag{2.37}$$

where we have defined the *projected area*

$$\mathbf{A} = \frac{1}{2}\sum_{k,i} R_{k,i} \times R_{k,i+1} \tag{2.38}$$

where, for a rotation about $\hat{z}$, we have taken only the $z$ component of $A$.

In our simulations, however, we probe these properties using computationally manageable system sizes coupled with periodic boundary conditions, so expressions such as (2.37) are of no direct utility.

Consider a modification of our geometry outlined above; instead of one cylinder, we will consider two concentric cylinders with radii $R_c$ and $R_c + d$, where $d \ll R_c$. This toroidal geometry is topologically equivalent to the imposition of periodic boundary conditions. The classical moment of inertia in this case will be given by $mNR_c^2$, and the area can be written as $WR_c/2$, where $W$ is called the "winding number". The winding number is defined as the total flux of paths winding around the torus multiplied by the circumference of the torus. Using these values in equation (2.37), we obtain

$$\frac{\rho_s}{\rho} = \frac{\langle W^2\rangle}{2\lambda\beta ND} \tag{2.39}$$

where the winding number is formally defined as

$$\mathbf{W} = \sum_{k=1}^{N}\int_0^\beta d\tau\left[\frac{dR_k(\tau)}{d\tau}\right] \tag{2.40}$$

If no world-lines wrap around the periodic boundary, $W$, and thus $\rho_s$, will be zero. This makes it clear that the sampling of long particle permutation cycles are critical for capturing superfluid properties.

One final observable we will discuss in this section is the one-body density matrix, defined formally in second-quantized form as $n(r,r') = \left\langle \hat{\psi}^\dagger(r)\hat{\psi}(r')\right\rangle$, where $\hat{\psi}^\dagger(r)\hat{\psi}(r)$ is the local density operator, $\hat{\psi}^\dagger(r)$ is a particle creation operator, and $\hat{\psi}(r)$ is a particle annihilation operator. In terms of our density matrix formalism, we can express the one-body density matrix as

$$n(r_1, r_1') = \frac{\Upsilon}{Z} \int dr_2 dr_3 \cdots dr_N \times \rho(r_1, r_2, r_3, \cdots, r_N; r_1', r_2, r_3, \cdots, r_N; \beta) \tag{2.41}$$

for an isotropic system of volume $\Upsilon$. It should be clear that this quantity cannot be calculated using configurations in the $Z$-sector. Although in traditional PIMC there have been techniques developed to manually open world-lines to compute this quantity [61] with some success, in using the worm algorithm we avoid these manipulations completely and accumulate accurate statistics for the one-body density matrix *almost automatically* by virtue of our sampling in an extended configuration space.

One customarily writes the one-body density matrix in a form averaged over all angles $\Omega$, given by

$$n(r) = \frac{1}{4\pi\Upsilon} \int d\Omega \int dr'\, n(r', r' + r) \tag{2.42}$$

where we note that the Fourier transform of this object is the momentum distribution, which is experimentally accessible. One can in fact extract the condensate fraction (which will be non-zero for superfluids if $D \geq 3$) from (2.42) by first calculating

$$n_0 = \frac{1}{\Upsilon^2} \int dr\, n(r) \tag{2.43}$$

and then taking $\lim_{r \to \infty}$.

## 2.4 Path Integral Ground State

Accurate ground state ($T$=0) expectation values for quantum many-body systems can *also* be computed by means of quantum Monte Carlo simulations. In this work, the method utilized is the *Variational Path Integral* (VPI) method, which is an extension to zero temperature of traditional PIMC [56].

VPI (also referred to as Path Integral Ground State, PIGS [64]) is a projection technique, which filters out the exact ground state wave function out of an initial trial state.

### 2.4.1 Ground State Projection Methods

Again consider a system of $N$ identical particles of mass $m$, with the quantum-mechanical Hamiltonian $\hat{H}$ of the system again given by

$$\hat{H} = \hat{H}_0 + \hat{V} = -\frac{\hbar^2}{2m}\sum_{k=1}^{N}\nabla_k^2 + V(R). \tag{2.44}$$

The exact ground state wave function $\Phi_0(R)$ can be formally obtained from an initial trial wave function $\Psi_T(R)$ as

$$\Phi_0(R) \propto \lim_{\beta\to\infty}\int dR' G(R,R',\beta)\Psi_T(R') \tag{2.45}$$

where $G(R,R',\beta) = \left\langle R\left|\exp\left[-\tau\hat{H}\right]\right|R'\right\rangle$, is referred to as the imaginary-time propagator, with $\beta$ appearing as an effective inverse temperature in analogy with the finite temperature density matrix (though, here it plays the role of a projection time, given the analogy of the projection operator with a quantum evolution operator in imaginary time).

For a given $\hat{H}$, $G$ is generally not known analytically. Just as in PIMC however, using one of several schemes, it is possible to obtain approximations for $G$ whose accuracy increases as $\beta \to \infty$. Suppose $G_0(R,R',\beta)$ is one such approximation. Making use of the formal identity $\exp\left[-\beta\hat{H}\right] \equiv \left(\exp\left[-\tau\hat{H}\right]\right)^M$, with $\beta = M\tau$, one can express $G$ as

$$\begin{aligned} &G(R,R',\beta) \approx \\ &\int dR_1 dR_2 \cdots dR_{M-1} G_0(R,R_1,\tau)G_0(R_1,R_2,\tau)\cdots G_0(R_{M-1},R',\tau) \end{aligned} \tag{2.46}$$

The above approximate expression becomes exact only in the limit where $M \to \infty$ and $\tau \to 0$ such that $\beta \to \infty$. In a numerical calculation, however, one by necessity works with finite values, so $\tau$, the 'timestep', must be chosen to be small enough that our replacement of $G$ by $G_0$ entails an insignificant loss of accuracy; likewise $M$, the number of 'slices' which the imaginary time interval, $\beta$, is broken up into, must be chosen to be sufficiently large such that the $M\tau = \beta \to \infty$ limit can be approached to the desired precision.

The form of $G_0$ used determines the efficiency of the numerical calculation. The simplest form it can take on is the *primitive approximation*

$$G_0(R, R', \tau) = \rho_F(R, R', \tau)\, e^{-\frac{\tau}{2}[V(R)+V(R')]} + O(\tau^3), \tag{2.47}$$

$$\rho_F(R, R', \tau) = (4\pi\beta\tau)^{-3N/2} \prod_{k=1}^{N} \exp\left[-\frac{(\mathbf{r}_k - \mathbf{r}'_k)^2}{4\beta\tau}\right] \tag{2.48}$$

where $\rho_F$ is the exact propagator for a system of $N$ non-interacting particles.

We have so far succeeded in turning an intractable integral, (2.45) (since we do not know $G$), into a multi-dimensional integral which, in principle, can be solved.

### 2.4.2 Implementation: Monte Carlo

How does one go about calculating the above multi-dimensional integrals? Just as in the techniques outlined in previous sections, a Monte Carlo procedure is the natural approach, since it scales optimally in many dimensions (in comparison with other numerical integration schemes). The specific technique we use to do this is termed *Variational Path Integral* (VPI), also known as *Path Integral for the Ground State* (PIGS). The procedure works as follows: One samples a large set $\{X^q\}$, $q = 1, 2, ..., Q$, of discretized many-particle paths $X \equiv R_0 R_1 ... R_M$, where $R_j \equiv \mathbf{r}_{j1}\mathbf{r}_{j2}...\mathbf{r}_{jN}$ represents the positions of all $N$ particles in the system at the $j$th "slice" in imaginary time. These paths are sampled based on the probability density

$$\mathcal{P}(X) \propto \Psi_T(R_0)\Psi_T(R_M) \left\{ \prod_{j=0}^{M-1} G_0\left(R_j, R_{j+1}, \tau\right) \right\} \tag{2.49}$$

where $\Psi_T(R)$ is our trial wave function for the many-body system. One can show [61] that, for any choice of $\Psi_T$, in the limit as $L\tau \to \infty$ and $\tau \to 0$, $R_{M/2}$ is sampled from the square of the exact ground state wave function $\Phi(R)$. This allows one to calculate the ground state expectation value of any observable $\hat{O}$ diagonal in the coordinate representation as a simple statistical average

$$\langle \hat{O} \rangle \approx \frac{1}{Q} \sum_{q=1}^{Q} \mathcal{O}(R^q_{M/2}) \tag{2.50}$$

The ground state energy can be evaluated using the convenient "mixed estimator", which yields an unbiased estimate:

$$\langle \hat{H} \rangle \approx \sum_{q=1}^{Q} \frac{\hat{H}\Psi_T(R_1^q)}{\Psi_T(R_1^q)} \tag{2.51}$$

Expressions of the form (2.50) can be rendered arbitrarily accurate by letting $Q \to \infty$ (i.e. by sampling a large set of configurations).

For a particular choice of $\tau$, since the projection time $\beta = M\tau$ is necessarily finite, simulations must be performed for increasing $M$, until one finds that estimates of the observables have converged, within statistical errors.

One must also extrapolate estimates obtained for different $\tau$, in order to infer results in the $\tau \to 0$ limit. A more accurate form of $G$ (such as that thoroughly discussed in Ref. [65], accurate to $\tau^4$), or a more accurate trial wave function $\Psi_T$ allows one to obtain convergence with larger $\tau$ and/or fewer slices $M$, but, at least in principle, the extrapolated results ought to be independent of the choices of $G$ and $\Psi_T$.

In summary, with sufficient computer time and proper calibration of $\tau$ and $M$, one can generate estimates of physical observables that are *exact* (errors being only statistical).

Individual simulations involve generating the set $\{X^q\}$ using a random walk through path space. Though the paths could be updated by sampling changes in position for one bead at a time, we can increase computational efficiency by sampling a variety of trial moves involving more than one bead. The implementation includes trial moves involving rigid displacements of an entire particle path (*displace* type moves), and multilevel sampling updates (see, for instance, Ref. [61]), which are divided into "wiggles" of central path portions (i.e., updates not including an endpoint, namely $j$=0 or $j$=$M$), and "wag" updates involving path endpoints (which involve $\Psi_T$ in the acceptance test, as do the *displace* moves).

The suite of trial updates may also be expanded to include sampling procedures similar to those used in Section 2.3.2 for the worm algorithm, which would potentially provide efficiency benefits.

It should be noted that, unlike in PIMC, permutations need not be explicitly sampled with their own set of trial moves; since the paths are open, the algorithm allows ample

opportunity for all configuration updates corresponding to permutations to be efficiently sampled. Thus, though permutations are in a sense explicitly included in the sampling, there is no direct measure of their frequency available.

Despite the lack of permutation statistics, it is possible – for systems lacking translational invariance – to compute the superfluid density using an extrapolation to $\beta \rightarrow \infty$ of the fractional winding number, though there are some ambiguities involved in this process. One procedure is outlined in Reference [66].

The trial wave function utilized in these simulations is of the Jastrow type, which for a system of $N$ identical pair-wise interacting particles has the form:

$$\Psi_T(\mathbf{r}_1, \mathbf{r}_2, ...\mathbf{r}_N) = \prod_{i<j}^{N} e^{-\frac{1}{2}u(r_{ij})} \tag{2.52}$$

which fulfills the symmetry requirement of a many-boson wave function. The pseudo-potential $u$ is chosen to be of some simple form (usually a Padé approximation of the form $(a + b\ r^n)/(1 + c\ r^m)$, with parameters obtained empirically, by minimizing the energy expectation value computed in separate variational calculations).

The greatest utility of the algorithm is that one can obtain accurate structural and energetic properties of many-body systems at $T$=0 with great efficiency (whereas, with the worm algorithm and PIMC, one must perform a series of more expensive simulations at different low temperatures and then extrapolate properties to the ground state).

## 2.5 Computational Details

In this section, we will discuss technical details related to error estimation, the forms of the intermolecular potentials assumed, as well as a selection of other topics pertinent to our simulations.

### 2.5.1 Boundary Conditions

For bulk simulations, our aim is to predict the properties of systems with order $\sim 10^{23}$ atoms or molecules, i.e. effectively the thermodynamic limit. Such a number of particles

is many orders of magnitude beyond the capability of today's most powerful computers (and will likely remain inaccessible for the foreseeable future, short of a dramatic innovation in computing architecture). So it is necessary for us to utilize methods which allow simulations of much smaller systems to capture our properties of interest, or, at worst, methods to extrapolate to the thermodynamic limit on the basis of results calculated using a series of different system sizes.

The standard technique to reduce these finite-size effects is to introduce periodic boundary conditions, which eliminate the spurious influence of artificial surfaces. We do this the standard way, by using a rectangular (or box, in 3D) simulation cell, and implementing the minimum image convention. Our interaction potentials, given by expressions like (2.57) and (2.58), are short range, and we apply a truncation at some value $r_c < L/2$, where $L$ is the minimum dimension of the box (in the case of long-range interactions, like in coulombic or gravitational problems, we would need to implement Ewald sums, see Reference [67]). We then typically smooth the potential $v$ and its derivative to zero at $r_c$ via the following modification,

$$v_{\text{smooth}}(r) = \begin{cases} v(r) - a - b(r - r_c), & r < r_c \\ 0 & \text{otherwise} \end{cases} \tag{2.53}$$

where $a = v(r_c)$, and $b = \frac{d}{dr} v(r)|_{r_c}$. Corrections to the calculated potential energies due to truncation and smoothing can be estimated using $g(r)$ and our original $v(r)$, where we either set $g(r) = 1$ (its asymptotic value) beyond the cutoff (which works well for liquids or gases), or perform a more involved fitting procedure, such one based on the Percus-Yevick approximation - see Ref. [67]. The influence of these approximations is small, and is reduced as the system size increases.

In all simulations performed for the research presented in thesis, we work in periodic boundary conditions, and, for simulations of the bulk, we use the suite of procedures outlined above. For simulations of finite systems (for example, pinned clusters), we simply set the box to be large enough that the periodic boundary conditions have no influence, and we do not perform truncation nor smoothing.

### 2.5.2 Estimates for Statistical Errors

For the thermal average of a physical observable $\hat{O}$, calculated as a mean of its values over a large set of $t$ many-particle paths $X_j$ generated by our sampling procedure, we have

$$\left\langle \hat{O} \right\rangle \approx \frac{1}{t} \sum_{j=1}^{t} \hat{O}(X_t). \tag{2.54}$$

where we collect data after determining that the system has relaxed to its equilibrium configuration from the initial configuration used as input.

In order for our measurement to be meaningful, however, we must provide an associated statistical error. If we assume that the calculation of $\hat{O}$ takes place for values of $X_j$ such that the measurements are independent and normally distributed, we can estimate the uncertainty of $< \hat{O} >$ as

$$\sigma \approx \sqrt{\frac{1}{(t-1)} \sum_{j}^{t} \left( \hat{O}(X_j) - \left\langle \hat{O} \right\rangle \right)^2}. \tag{2.55}$$

However, we sample states via a Markov chain in which one state is generated starting from the previous state, and so on. Sequential states in this random walk are thus correlated, and we underestimate the statistical error by using (2.55). One must find a way to perform the average over uncorrelated configurations.

The common approach is to split the simulation up into a number of equal blocks containing a large number (thousands) of sequential configurations (the number of sequential configurations divided by the number of particles is defined as the number of sweeps), over which partial averages for each block are calculated and stored. One then constructs bins with a fixed number of data blocks in each, and obtains the error as the standard deviation (variance) of the resulting histogram.

For any given set of data blocks, one performs this procedure by increasing the bin size (reducing the number of bins) until the estimates of the error converge (so long as the number of bins is not too small, typically no fewer than 20 bins). If convergence is not observed, then one must gather more statistics by generating additional data blocks via the usual sampling procedures as before.

This blocking and binning procedure will not change the calculated mean, but the results for the errors will better reflect the true statistical uncertainty.

To give one a sense of the numbers involved in these simulations, a typical run (a given Hamiltonian with one specific particle density at one temperature) may require the collection of anywhere between only fifty up to tens of thousands of data blocks composed of usually 1000 sweeps each. Some fraction of these data blocks will be discarded to eliminate configurations not representative of the equilibrium state (one determines this number by probing the convergence of the mean itself for different discard numbers), and, in general, the remaining blocks will be distributed into, for example, equal bins containing 5, 10, and 20 data points, with the resulting error from each binning compared to determine if the error has converged.

### 2.5.3 Interparticle Potentials

With the procedures outlined in the above sections, one seemingly has everything necessary to simulate systems of bosonic particles in such a way that arbitrary accuracy can be obtained (which is true - for any input Hamiltonian, the methods can generate results which can be made arbitrarily accurate, i.e. there are no uncontrolled approximations).

There is a wrinkle in the works, however, related to the description of interactions between particles. We make several approximations here which warrant some discussion and justification.

First, we will treat atoms like $^4$He and molecules like $p$-$H_2$ as elementary bosons, i.e. *almost* ignoring their composite form by conflating the electronic and nuclear structure, treating each as a neutral particle with no direct treatment of the substructure. This is consistent with working within the *Born-Oppenheimer approximation*; the electrons adapt instantly to changes in the configuration of nuclei, justified by their much lower mass.

We have considered only potentials which are *central*, meaning that the interaction only depends upon relative distances. In the case of modeling complex molecules, such an approach cannot be justified, and at a minimum, one cannot neglect relative orientations and thus must take into account angular dependencies. Some success can be achieved by treating extended molecules as collections of centrally-interacting atoms with some

additional model for the chemical bonds between them (for example, this framework can be used for modeling some molecular liquids). For the work we are interested in (simulations of $^4$He and molecular hydrogen), the anisotropies involved are weak, and the approximation of using central potentials is adequate.

In general, central interparticle potentials can be expressed as sums of terms involving clusters of particles,

$$V(r_1, r_2, \cdots, r_N) = \sum_{i<j} v_{ij}^{(2)}(r_i, r_j) + \sum_{i<j<k} v_{ijk}^{(3)}(r_i, r_j, r_k) + \cdots \tag{2.56}$$

where $v^{(2)}$ is the part of the interaction involving all pairs of particles, $v^{(3)}$ involves all triplets, etc. In most cases, $v^{(2)}$ is by far the dominant part of the interaction, and as a good approximation, we can consider the potential to be only a sum of these pair-wise terms.

In cases such as molecular hydrogen, where three-body effects cannot be entirely neglected, we can incorporate some of their effects indirectly into an *effective* two-body potential. We will discuss this later in this subsection.

The particles we deal with in our simulations are electrically neutral, and according to classical mechanics, the only force between them should be gravitational (which is negligibly small), as electrostatic forces should be zero. To see this, consider two neutral particles at a large (much greater than their radii) separation $r$. If the distribution of electric charge around each particle remains rigid and spherically symmetric, then the coulombic attraction and repulsion forces between the respective electrons and nuclei will cancel to zero.

While it is clear that the system could reduce its total energy by having the particles induce in each other mutual dipole moments, one can argue on symmetry grounds that, outside of some external perturbation (such as an imposed external field), this event would never occur (i.e. the particles would remain in a state of unstable equilibrium, like a ball at the crest of a hill). In quantum mechanics, however, instantaneous fluctuations in the electron density break this symmetry, and indeed allow an electrostatic dipole to be induced.

It can be shown that the electrostatic field generated by a single electrostatic dipole

is proportional to $1/r^3$, which leads to a dipole attraction (also referred to as *London attraction*, *dispersion*, and *Van der Waals* attraction) proportional to $1/r^6$, which is the dominant force at large distance.

At short distances, another quantum effect becomes important - the Pauli exclusion principle. Though we do not model the electrons directly, we must take into consideration their fermionic character as the composite atoms or molecules are brought close together. If their relative distance is short enough to cause an overlap of atomic or molecular orbitals for electrons in both particles (if we were to model them explicitly), there will be a large energetic cost associated with the promotion of electrons to higher energy levels (since the exclusion principle prevents more than two electrons, one spin up and one spin down, from occupying any given energy level).

Though there are (very expensive) post-Hartree-Fock ab initio methods to treat these electronic effects, and indeed generate entire intermolecular or interatomic potentials, very accurately (though still within the Born-Oppenheimer approximation) - see Ref. [68, 69] - it is sufficient, for the properties we are interested in, to simply model this effect with some effective hard-core repulsion. A function with the form of an exponential in powers of $r$ has some theoretical justifications, but, for reasons of computational efficiency, one generally models repulsion instead using a term proportional to $1/r^{12}$.

The result of this line of reasoning is the *Lennard-Jones* (LJ) potential, used extensively in molecular dynamics (MD) simulations, as well as for QMC simulations of bosons. The LJ potential has the form

$$v(r) = 4\epsilon \left\{ \left(\frac{\sigma}{r}\right)^{12} - \left(\frac{\sigma}{r}\right)^{6} \right\} \tag{2.57}$$

where $\epsilon$ is the well-depth of the potential (setting a characteristic energy) and $\sigma$ is the hard-core radius (setting a characteristic length-scale). The LJ potential is empirical in that these two parameters are adjusted as to best reproduce particular experimental results. For $p$-$H_2$, the values of the parameters are $\sigma$=2.96 Å and $\epsilon$=34.16 K.

In our simulations of molecular hydrogen, we make use of an enhanced LJ-type potential to model the $p$-$H_2$-$p$-$H_2$ and $o$-$D_2$-$o$-$D_2$ intermolecular interactions, namely, the *Silvera-Goldman* (SG) pair potential [70] given by

$$v_{SG}(r) = \epsilon \left\{ e^{-\alpha x - \gamma x^2} + \left[ \frac{C_6}{x^6} + \frac{C_8}{x^8} + \frac{C_9}{x^9} + \frac{C_{10}}{x^{10}} \right] F(x) \right\} \tag{2.58}$$

where $x = r/r_m$ and $F(x) = e^{-[(D/x)-1]^2}$ for $x < D$ and 1 otherwise. The parameters used in (2.58) are defined in Table 2.1.

| Parameter | Value | Parameter | Value |
|---|---|---|---|
| $r_m$ | 6.444 | $C_6$ | 12.14 |
| $D$ | 8.248 | $C_8$ | 215.2 |
| $A$ | 1.713 | $C_9$ | 143.1 |
| $\alpha$ | 1.5671 | $C_{10}$ | 4813.9 |
| $\gamma$ | 0.00993 | $\epsilon$ | 315774.661 |

Table 2.1: Parameters for the Silvera-Goldman potential given by (2.58). All parameters are dimensionless, except for $\epsilon$ (given in K) and $r_m$ (given in Å).

The first term in (2.58) models the Pauli repulsion between electrons, and the terms in square brackets with even inverse powers of $x$ incorporate the long-range attraction due to the induced dipoles, and $F(x)$ damps the power-law terms at short distances. The term $C_9/x^9$ effectively incorporates three-body Axilrod-Teller effects (which arise from a third-order perturbation correction to the dispersion forces [71]). Though this latter term obviously is not equivalent to a full incorporation of three-body interactions, three-body corrections of this form have been found empirically in simulations of fluids to capture a great deal of the physics missing when only two-body terms are explicitly present [72].

The quality of the potential required depends upon what information one is trying to obtain. Often, qualitative features can be reliably extracted by using, for example, square-well potentials, or even hard or soft sphere interactions. In our studies, we are not interested primarily in obtaining very accurate energies - our goal is to capture broad phase character, explore the role of geometry, and obtain accurate quantum many-body statistics. To this end, we use the most accurate potentials available, such as (2.58), which can be rendered with reasonable computational effort. It is not expected that refinements here would fundamentally change the observed physics (at most, we would expect an effective shift in temperature for the properties we are interested in).

## 2.6 A Note on Molecular Hydrogen

As outlined in Chapter 1, a useful quantity for determining how important quantum effects are is the de Boer parameter $\Lambda$, which is proportional to the ratio of the de Broglie wavelength of the particles, $\lambda=h/p$, to their hard-core radius, $\sigma$. When $\Lambda \geq 1$, quantum effects play a dominant role; when $\Lambda \leq 1$, quantum effects are small, and one can preclude macroscopic quantum behavior such as BEC and SF.

After the two stable isotopes of helium, the stable baryonic particles with the highest value of $\Lambda$ are molecular hydrogens, which have comparable mass to helium, but interact more strongly. The two hydrogenic composite bosons are $H_2$ (molecular hydrogen) and $D_2$ (molecular deuterium, which has twice the mass of $H_2$ and roughly an equal mass to $^4$He), which can interact almost like rare gases, or like molecular species with strong angular anisotropies.

$H_2$, composed of two electrons and two protons, can exist in two distinct states:

- **ortho-hydrogen**: the nuclear spins of the protons are aligned, leading to nuclear spin $I$=1. Odd-integer values of the rotational quantum number $J$ are allowed. Ortho-hydrogen molecules have a highly anisotropic charge distribution, and spin-orbit coupling may need to be accounted for.

- **para-hydrogen**: the nuclear spins of the protons are anti-aligned, leading to nuclear spin $I$=0. By the symmetry requirements of the nuclear wave function, only even-integer values of the rotational quantum number $J$ are allowed. Para-hydrogen molecules have a nearly isotropic charge distribution.

$D_2$, composed of two electrons, two neutrons, and two protons, similarly exists in two states. Within the nucleon, two boson pairs (one neutron plus one proton) form, and a symmetry requirement for the total nucleon wave function is imposed:

- **ortho-deuterium**: Nuclear spin states of $I$=0 and $I$=2 are allowed, with only even-integer values of the rotational quantum number $J$ permitted. Ortho-hydrogen molecules have a nearly isotropic charge distribution.

- **para-deuterium**: Only nuclear spin state $I$=1 is possible, with only odd-integer values of the rotational quantum number $J$ permitted. Ortho-hydrogen molecules have a highly anisotropic charge distribution.

At room temperature, $H_2$ gas in equilibrium is composed of 25.1% para and 74.9% ortho states; as $T$ approaches 0 K, entropy effects (based on the degeneracy of rotational levels) diminish and the higher-energy ortho-hydrogen state is disfavored, with a 100% occupation of the para-hydrogen state below $T$ ~20 K [73].

Likewise, at room temperature, $D_2$ gas in equilibrium has relative abundances of 33.3% para and 66.7% ortho states [73]; as $T$ approaches 0 K, entropy effects diminish and the much higher-energy para-deuterium state, as well as the slightly higher energy ortho state with $I$=2, are disfavored, and we observe 100% occupation of the ortho-deuterium state with $I$=0 below $T$ ~20 K. [73]

We further note that the energy required to promote $p$-$H_2$ ($o$-$D_2$) from its rotational ground-state to its first rotational excited state is roughly 170 K (86 K); thus, only $J$=0 rotational states are occupied at low temperature. [73]

We will thus treat molecular hydrogen isotopes at low temperature as being solely composed of either $p$-$H_2$ or $o$-$D_2$, both cases in the rotational ground state.

# Chapter 3

# Adsorption of *para*-hydrogen on fullerenes

## 3.1 Introduction

Low temperature adsorption of highly quantal fluids, such as helium or *para*-hydrogen ($p$-$H_2$) on the outer surface of a fullerene ("buckyball") can provide insight into physical properties of a quantum many-body system confined to spatial regions of nanometer extent. As the diameter of the fullerene is increased, the properties of the adsorbate ought to interpolate between those of a cluster with a solvated impurity, and those of an adsorbed film on a planar substrate.[1]

We consider adsorption of $p$-$H_2$ on a single fullerene $C_l$, with $l$=20, 36, 60 and 80. All of these molecules are strong adsorbers, and very nearly spherical. Background for this study is provided by the wealth of theoretical [39, 52, 74, 75, 76, 77] and experimental [32, 34, 35, 36, 78, 79, 80] work, spanning over two decades, aimed at investigating the properties of adsorbed $p$-$H_2$ films on various substrates. This work is also inspired by recent theoretical results on adsorption of helium on buckyballs [81, 82]. A considerable

[1] A version of this chapter has been published in:
Joseph Turnbull and Massimo Boninsegni. Physical Review B **71**, 205421 (2005).
Reprinted in Virtual Journal of Nanoscale Science and Technology **11**, 23 (2005).

effort has also been devoted to the theoretical characterization of superfluid properties of solvating $p$-$H_2$ clusters around linear molecules, such as OCS [30, 31].

The study of hydrogen adsorption on nanocarbons falls within the same general research theme, but is also motivated by possible practical applications; an important example is hydrogen storage, for fueling purposes. So far, research along these lines has mostly focused on nanotubes [83, 84, 85, 86, 87], but it seems worthwhile to extend the investigation, possibly providing useful quantitative information on adsorption on other nanostructures, including fullerenes.

In this chapter, energetic and structural properties of a monolayer of $p$-$H_2$ molecules adsorbed on a $C_l$ fullerene are investigated theoretically, by means of ground state Quantum Monte Carlo simulations (PIGS), as outlined in chapter 2. In order to provide a reasonable, quantitative account of the corrugation of the surface of the fullerene, we explicitly modeled in our study each individual carbon (C) atom. For comparison, however, we have also performed calculations with a simpler model, describing fullerenes as smooth spherical surfaces, interacting with $p$-$H_2$ molecules via an angle-averaged potential.

Only one adsorbed layer is found to be thermodynamically stable on these small nanocarbons. On a corrugated substrate, a commensurate solid layer is observed at equilibrium; as the chemical potential is increased, $p$-$H_2$ is compressed discontinuously to an incommensurate solid layer on $C_{20}$, $C_{36}$ and $C_{60}$. We could not find, within the statistical uncertainties of our calculation, evidence of an incommensurate layer on $C_{80}$.

The difference in compression between commensurate and incommensurate layers, as measured by the effective $p$-$H_2$ coverage, is approximately 216% for $C_{20}$, and decreases to $\sim 25\%$ for $C_{60}$.

Obviously, on a smooth fullerene, there is no distinction between commensurate and incommensurate layers. In the absence of corrugation, energetics of the adsorbed layer are determined primarily by the interactions among $p$-$H_2$ molecules. The ground state of $p$-$H_2$ in two dimensions (2D) is a solid, with molecules forming a triangular lattice [38, 52]. Our results indicate that $p$-$H_2$ molecules attempt to reproduce the same triangular arrangement as on an infinite plane, even when confined to moving on a spherical surface of radius as small as a few Å.

Evidence of quantum exchange is absent in these systems, i.e., no evidence suggesting possible superfluid behavior is gathered in this work.

The remainder of this chapter is organized as follows: Sec. 3.2 offers a description of the model used for our system of interest, including a discussion of the potentials used and the justifications for underlying assumptions. Sec. 3.3 involves a brief discussion of the computational technique and specific details of its implementation, in addition to details of calibration and optimization. The results are presented in Sec. 3.4; finally, Sec. 3.5 is a summary of the findings and our concluding remarks.

## 3.2 Model

We consider a system of $N$ $p$-$H_2$ molecules, in the presence of a single $C_l$ molecule. The latter is assumed fixed in space, owing to its relatively large mass; the center of the molecule is taken as the origin of a Cartesian coordinate frame. The $l$ individual C atoms are fixed at positions $\{\mathbf{R}_k\}$, $k$=1,2,...,$l$. All of the atoms and molecules are regarded as point particles. The model quantum many-body Hamiltonian is therefore the following:

$$\hat{H} = -\frac{\hbar^2}{2m}\sum_{i=1}^{N}\nabla_i^2 + \sum_{i<j}V(r_{ij}) + \sum_{i=1}^{N}\sum_{k=1}^{l}U(|\mathbf{r}_i - \mathbf{R}_k|) \qquad (3.1)$$

Here, $m$ is the mass of a $p$-$H_2$ molecule, $r_{ij} \equiv |\mathbf{r}_i - \mathbf{r}_j|$, $\{\mathbf{r}_j\}$ (with $j$=1,2,...,$N$) are the positions of the $p$-$H_2$ molecules, $V$ is the potential describing the interaction between any two of them, and $U$ represents the interaction of a $p$-$H_2$ molecule with a C atom.

The interaction $V$ is the Silvera-Goldman potential described in Chapter 2, while the interaction of a $p$-$H_2$ molecule and a C atom is modeled using a standard 6-12 Lennard-Jones (LJ) potential, with $\epsilon = 32.05$ K and $\sigma = 3.179$ Å (see, for instance, Ref. [87]).

The model (3.1) already contains important physical simplifications, such as the neglect of zero-point motion of C atoms, as well as the restrictions to additive pairwise interactions (to the exclusion of, for example, three-body terms), all taken to be central, and the use of the highly simplified LJ interaction. On the other hand, (3.1) is the simplest microscopic model that explicitly takes into account the corrugation of the surface of the buckyball.

A further simplification can be introduced by replacing the third term in (3.1) with $\sum_i \tilde{U}(r_i)$, where $\tilde{U}$ is the following, spherically symmetric external potential (see Ref. [81] for details):

$$\begin{aligned}\tilde{U}(r,\mathrm{R}) &= \frac{\epsilon n}{\mathrm{R}r}\left\{\frac{\sigma^{12}}{5}\left[\frac{1}{(r-\mathrm{R})^{10}}-\frac{1}{(r+\mathrm{R})^{10}}\right]\right. \\ &- \left.\frac{\sigma^{6}}{2}\left[\frac{1}{(r-\mathrm{R})^{4}}-\frac{1}{(r+\mathrm{R})^{4}}\right]\right\} \end{aligned} \tag{3.2}$$

Here, $n = 4\pi\theta\, a^2$, $a$ being the radius of the fullerene and $\theta$ being the areal density of C atom on its surface; $\epsilon$ and $\sigma$ are the parameters of the LJ potential $V$ introduced for the fully corrugated model. By using (3.2), one is describing the fullerene as a smooth spherical shell, i.e., corrugation is neglected. This approximation substantially simplifies the calculation; it has been adopted in recent studies of helium adsorption on buckyballs [81, 82].

As mentioned above, in this work we have performed calculations based on the full model (3.1), as well as using the effective potential (3.2); results obtained in the two ways are compared in Sec. 3.4.

## 3.3 Computational Method

In this section, the method utilized is *Variational Path Integral* (VPI), as described in chapter 2, section 2.4. The trial wave function utilized is of the Jastrow type:

$$\begin{aligned}\Psi_T(\mathbf{r}_1,\mathbf{r}_2,\ldots\mathbf{r}_N) &= \left(\prod_{i=1}^{N}\prod_{k=1}^{l} e^{-w(|\mathbf{r}_i-\mathbf{R}_k|)}\right)\times \\ &\times \left(\prod_{i<j}^{N} e^{-u(r_{ij})}\right) \end{aligned} \tag{3.3}$$

which fulfills the symmetry requirement of a many-boson wave function. In the case of the spherically averaged model, $l$=1 and $R_1$=0. The pseudo-potentials $w$ and $u$ were chosen as follows:

$$w(r) = \frac{\alpha}{r^x} \text{ and } u(r) = \frac{\gamma}{r^5} \tag{3.4}$$

where $x = 2$ for the spherically averaged potential, and $x = 5$ for the corrugated case. The values of the parameters $\alpha = 80$ Å$^x$, $\gamma = 750$ Å$^5$ and $x$ were obtained empirically, by minimizing the energy expectation value computed in separate variational calculations.

Using the given $\Psi_T$, we observe convergence of the ground state energy estimates with a projection time $L\tau = 0.250$ K$^{-1}$, with $\tau = \tau_\circ = 1/640$ K$^{-1}$. Estimates for all quantities quoted in this study were obtained using $\tau = \tau_\circ$, even though convergence of the estimates for structural quantities can be typically observed with values of $\tau$ significantly greater than $\tau_\circ$ (for an equal projection time).

VPI calculations for a range of $p$-$H_2$ coverages were carried out for each of $C_{20}$, $C_{36}$, $C_{60}$, and $C_{80}$ (we refer here to the near spherical isomers of each). We use an initial configuration of para-hydrogen molecules surrounding the fullerene at a distance of approximately twice the $C_l$ radius (i.e., making sure that no $p$-$H_2$ start off within the buckyball). Because of the strongly attractive character of the $C_l$, for a small enough number of surrounding hydrogen molecules the system remains spatially confined (i.e., $p$-$H_2$ molecules do not evaporate). Thus, even though periodic boundary conditions are used in the simulation, they have no effect, so long as a sufficiently large simulation cell is used.

The systematic errors of our calculation are attributable to the finite projection time $L\tau$ and the finite time step $\tau$. Based on comparisons of results obtained from simulations with different values of $L$ and $\tau$, we estimate our combined systematic error on the total energy per $p$-$H_2$ molecule to be of the order of 0.6 K or less.

## 3.4 Results

Physical quantities of interest include the ground state energy per $p$-$H_2$ molecule $e(N)$ and the radial $p$-$H_2$ density $\rho(r)$ about the fullerene, as a function of the total number $N$ of molecules. Results for $e(N)$ for all fullerenes considered in this study are shown in Figs. 3.1 through 3.4.

Let us consider first the case of $C_{20}$ (shown in Fig. 3.1), as it allows us to illustrate some of the general features seen on other fullerenes as well. Filled circles represent the energy estimates yielded by the fully corrugated model (3.1), whereas filled squares represent estimates obtained using the spherically averaged potential $\tilde{U}$ described in Sec. 3.2. Solid lines are polynomial fits to the numerical data. Also shown in the inset is the number of adsorbed molecules $N$ versus the chemical potential $\mu$ (in K). This is obtained by first fitting the results for $e(N)$, then minimizing the grand canonical potential $\phi(N) = N(e(N) - \mu)$ with respect to $N$, for different values of $\mu$. The chemical potential of bulk solid $p$-$H_2$ at zero temperature, computed by Quantum Monte Carlo using the Silvera-Goldman potential, is $\mu_o = -88$ K (from Ref. [88]), and that is where all of the $N(\mu)$ curves end.

There are some qualitative similarities, but also important differences (mainly at low $N$) between the results yielded by the two models utilized. In the large-$N$ limit, both models yield essentially the same energy estimates, as corrugation becomes unimportant for thick adsorbed films. This is the case on all fullerenes.

Both $e(N)$ curves display a single minimum at a specific number $N_e$ of $p$-$H_2$ molecules. The minimum corresponds to the mathematical condition $e(N_e) = \mu(N_e)$, and physically to the formation of a stable $p$-$H_2$ layer. On the corrugated $C_{20}$, a stable layer occurs for a number $N_e \equiv N_C = 12$, significantly smaller than that ($N_e \equiv N_S = 22$) obtained on a smooth fullerene.

Moreover, the energy per molecule $e_C(N_C)$ for the corrugated model is approximately 10% lower than that on a smooth substrate ($e_S(N_S)$), i.e., the corrugated model yields stronger $p$-$H_2$ binding. Qualitatively similar results are observed on all fullerenes; however, the difference between $N_C$ and $N_S$ is seen to decrease with the radius of the fullerene, whereas the difference between the minimum energy values in the two models is $\sim 10\%$ for all fullerenes.

Corrugation introduces the conceptual distinction between a layer that is *commensurate* with the substrate (i.e., the outer surface of the fullerene), and one that is *incommensurate* with it. In a commensurate layer, each $p$-$H_2$ molecule sits right on top of the center of one of the hexagonal (or, pentagonal) faces of the polyhedron formed by C atoms. For example, $C_{20}$ has the shape of a dodecahedron, i.e. it has 12 pentagonal faces, corre-

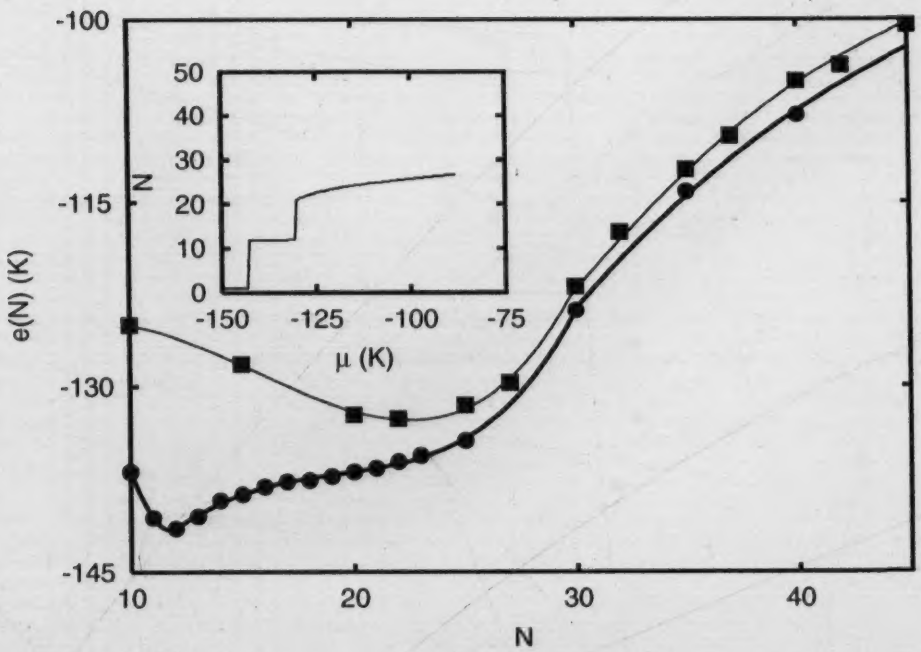


Figure 3.1: Energy per $p$-$H_2$ molecule $e(N)$ computed by VPI, as a function of the number of molecules adsorbed on a $C_{20}$ fullerene. Filled squares: results obtained with the angularly averaged potential (3.2). Filled circles: results obtained by explicitly modeling all carbon atoms in the fullerene. Solid lines are polynomial fits to the VPI data. Inset shows the number of particles $N$ plotted as a function of the chemical potential $\mu$, for the fully corrugated model. The chemical potential of bulk solid $p$-$H_2$ is $-88$ K, and that is where the $N(\mu)$ curve ends.

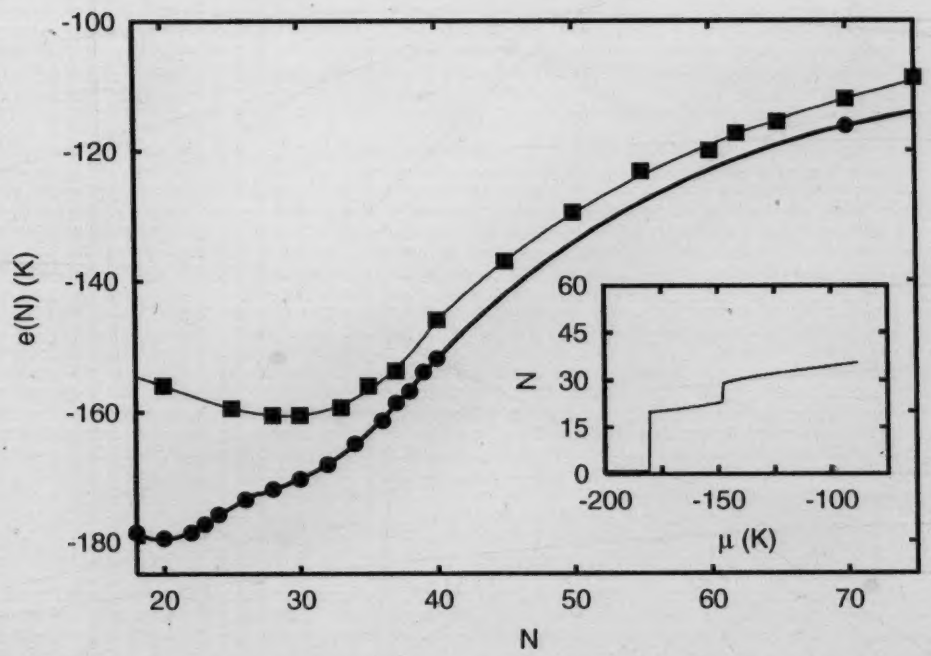


Figure 3.2: Same as Fig. 3.1, but for a $C_{36}$ fullerene. The commensurate layer has $N_C = 20$ $p$-$H_2$ molecules and is compressible, as evidenced by the finite slope of the curve $N(\mu)$ for $20 \leq N \leq 28$.

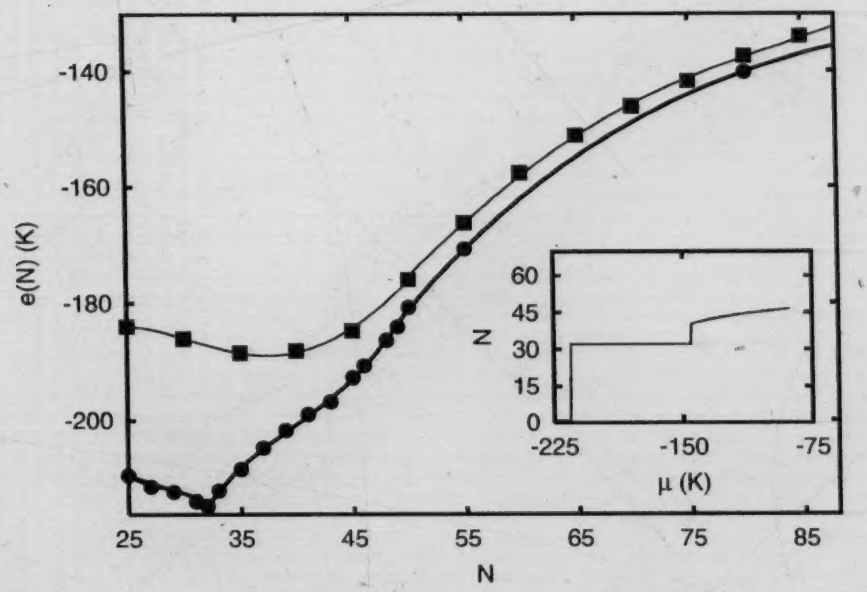


Figure 3.3: Same as Fig. 3.1, but for a $C_{60}$ fullerene.

sponding to as many adsorption sites for $p$-$H_2$ molecules. In an incommensurate layer, on the other hand, the arrangement of $p$-$H_2$ molecules is mostly determined by their mutual interactions; the fullerene, in this case, merely provides a background attractive potential and a curved geometry.

On all fullerenes studied here, using the corrugated model, the equilibrium adsorbed $p$-$H_2$ layer is found to be commensurate. On a corrugated substrate, one normally sees a transition from a commensurate to an incommensurate layer, as the chemical potential is increased from its equilibrium value [76]. No such transition can be observed on a smooth substrate, for which commensuration is undefined. This is indeed what we *generally* observe on the various fullerenes that we have considered. Details, however, differ for the different systems.

On $C_{20}$, the number of adsorbed $p$-$H_2$ molecules remains constant as the chemical potential is increased (i.e., no compression of the commensurate layer is observed), until

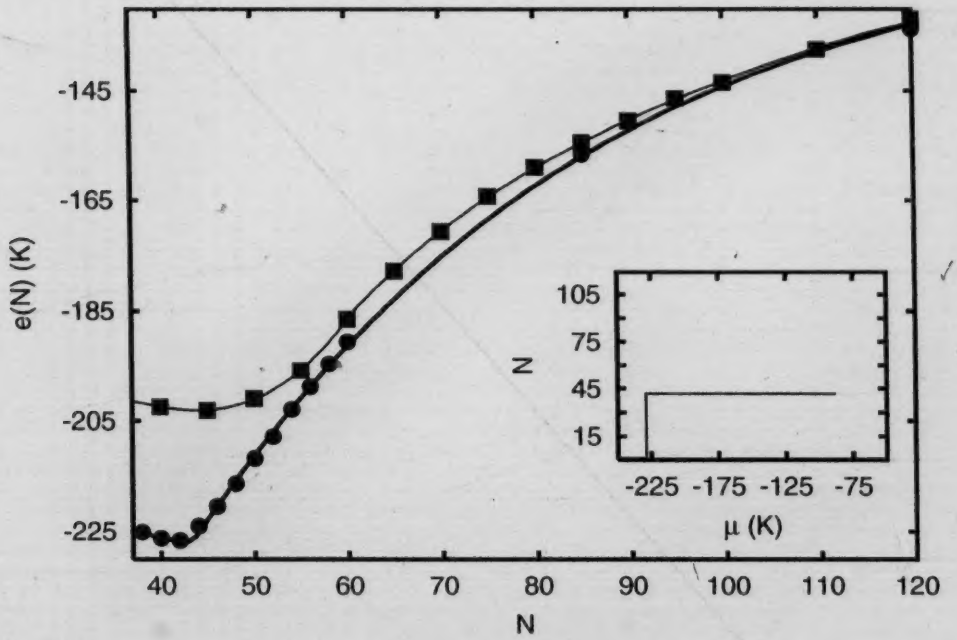


Figure 3.4: Same as Fig. 3.1, but for a $C_{80}$ fullerene.

it jumps discontinuously from $N_C = 12$ to $N_I = 22$ (see Fig. 3.1). This signals the (abrupt) appearance of an incommensurate layer. The number $N_I$ of molecules in such an incommensurate layer is the same as in the equilibrium layer on a smooth $C_{20}$; this leads us to surmise that the physics of the incommensurate layer on the corrugated fullerene and that of the equilibrium layer on the smooth fullerene are essentially the same. Thus, the main effect of the neglect of corrugation associated with the spherically averaged potential model, is the absence of the commensurate layer. We come back to this point later, when discussing density profiles.

The incommensurate layer that forms on a $C_{20}$ fullerene is compressible, i.e., the number of adsorbed molecules is seen to increase monotonically with $\mu$, up to $N \sim 28$; no second layer formation is seen before $\mu$ reaches the value ($\mu_o$) corresponding bulk *p*-$H_2$, above which thicker adsorbed films are thermodynamically unstable. In fact, on none of the fullerenes considered here, do we find more than one stable adsorbed layer.

On $C_{36}$, our results indicate that the commensurate layer is compressible; here too, however, a discontinuous transition occurs to an incommensurate layer, also compressible

| $C_l$ | $a$ | $N_C$ | $\theta_C$ | $N_I$ | $\theta_I$ | $N_S$ | $\theta_S$ |
|---|---|---|---|---|---|---|---|
| $C_{20}$ | 2.00 | 12 | 0.2387 | 22 | 0.4377 | 22 | 0.4377 |
| $C_{36}$ | 2.75 | 20 | 0.2105 | 28 | 0.2946 | 30 | 0.3157 |
| $C_{60}$ | 3.55 | 32 | 0.2021 | 40 | 0.2526 | 40 | 0.2526 |
| $C_{80}$ | 4.11 | 42 | 0.1979 | - | - | 45 | 0.2120 |

Table 3.1: Effective $p$-$H_2$ monolayer coverages for both the corrugated and uncorrugated models of the fullerenes. For the model including corrugation, $N_C$ and $N_I$ mark the number of $p$-$H_2$ molecules in the adsorbed layer at commensuration and incommensuration, respectively, with coverages $\theta_C$ and $\theta_I$ (in $\text{Å}^{-2}$). The number $N_S$ marks the number of $p$-$H_2$ molecules in the adsorbed layer on a smooth fullerene, $\theta_S$ being the corresponding coverage. The radius $a$ of each fullerene (in Å) is also given.

and again physically similar to the one that forms on a smooth fullerene.

The same physical behavior to that observed on $C_{20}$ is seen on $C_{60}$ and $C_{80}$, with an incompressible commensurate layer. On $C_{80}$, though, we fail to observe an incommensurate layer; it should also be noticed that, on this system, it is $N_C = 42$ and $N_S = 45$, i.e., there is a much smaller relative difference between $N_C$ and $N_S$ than on the other fullerenes.

Our results are summarized in Table 3.1, where the numbers are listed of $p$-$H_2$ molecules $N_C$ and $N_I$ in the commensurate and incommensurate layers adsorbed on a corrugated fullerene, as well as $N_S$ for a smooth fullerene. Also shown are the values of the effective coverage (2D density)

$$\theta = \frac{N}{4\pi a^2} \tag{3.5}$$

where, again, $a$ is the radius of the fullerene. The effect of the curvature of the substrate can be quantitatively established by comparing these values of $\theta$ to the equilibrium coverage of $p$-$H_2$ on a graphite substrate [76], estimated at 0.070 $\text{Å}^{-2}$. It should be noted that this definition of $\theta$ is used to compare the coverage as a function of *the surface area of the substrate*. A definition of the coverage incorporating the distance at which the $p$-$H_2$ sit above the fullerenes is given below (the two definitions would be equivalent for a planar

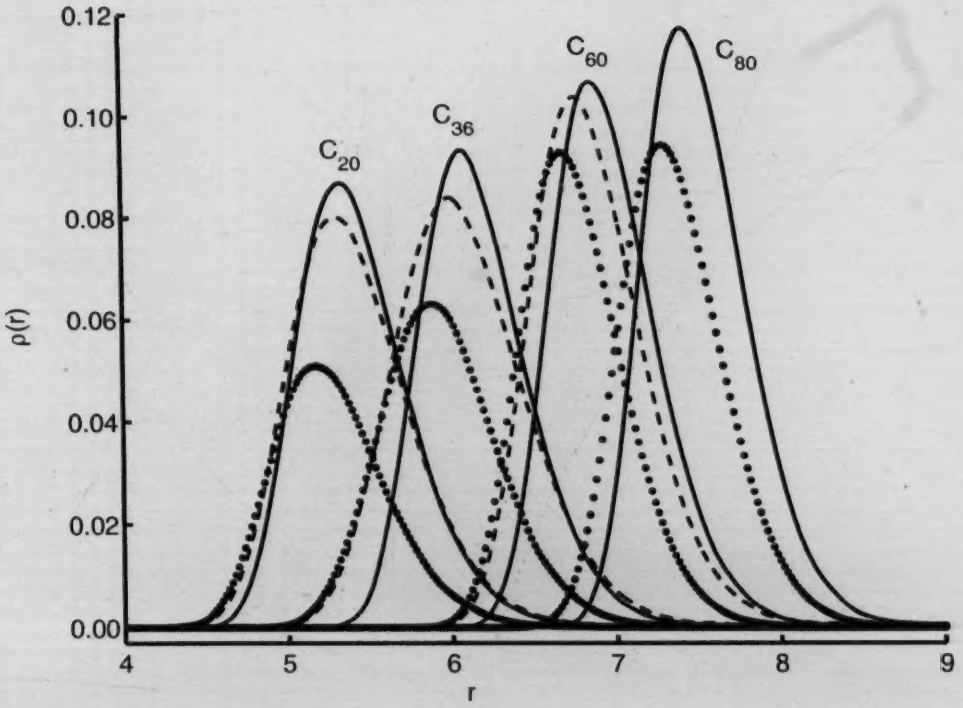


Figure 3.5: Radial density profiles of a $p$-$H_2$ layer adsorbed on $C_l$. Solid lines: profiles obtained for the smooth fullerene model. Dotted lines: profiles of commensurate layers on corrugated model. Dashed lines: profiles of incommensurate layers on corrugated models. Density is given in $Å^{-3}$, whereas the distance $r$ from the center of the fullerene is given in Å.

substrate, a distinction only arising with the introduction of non-zero curvature).

Structural information about these systems is offered by the radial density profiles $\rho(r)$ of $p$-$H_2$ on each of the four $C_l$ for the two models, all shown in Fig. 3.5. Solid lines denote the radial profiles on a smooth fullerene, while dotted and dashed lines denote radial density profiles in the corrugated model at commensuration and incommensuration, respectively. These results are qualitatively the same for each fullerene. The peak of the profile is shifted away from the center of the fullerene, as the system makes a transition from a commensurate to an incommensurate layer, which is not physically unexpected. No evidence is seen of second layer formation, on any of the fullerenes studied here, for values of the chemical potential for which the adsorbed film is thermodynamically stable

(i.e., $\mu \leq \mu_o$).

On comparing the density profile for the incommensurate layer on a corrugated fullerene (dashed lines) with that for a smooth fullerene (solid lines), one observes a further shift to the right for the case of a spherically averaged potential. Perhaps more interestingly, the incommensurate layer on a corrugated fullerene features a greater spatial width, with respect to that on a smooth fullerene (particularly on $C_{20}$ and $C_{36}$). Otherwise, these layers seem physically similar; for example, one can compute an effective 2D density $\theta_{eff}$ (different than the coverage $\theta$ discussed above) defined as

$$\theta_{eff} = \frac{N}{4\pi a_p^2} \tag{3.6}$$

where $a_p$ is the position of the peak of $\rho(r)$. The values obtained for the two layers are very close. In the case of a smooth fullerene, as one goes from $C_{20}$ to $C_{80}$, $\theta_{eff}$ approaches from below the value 0.067 $Å^{-2}$, namely the equilibrium density of $p$-$H_2$ in 2D [38]. This suggests that the physics of the incommensurate layer (and that on a smooth fullerene) is determined primarily by the interaction among $p$-$H_2$ molecules, which attempt to replicate, on a curved surface, the same arrangement as they do in 2D.

One further thing to note is that the width of the adsorbed $p$-$H_2$ layer on these systems is of the order of 1 Å, very close to that of an adsorbed monolayer film on graphite [76].

As pointed out in chapter 2, the computational method adopted here does not allow one to make a direct estimation of the $p$-$H_2$ molecule exchange frequency, unlike its finite temperature counterpart (Path Integral Monte Carlo). Nevertheless, from visual inspection of many-particle configurations generated in the Monte Carlo simulation, we observe high localization of paths associated to different molecules, which is substantial evidence that many-particle permutations are absent in this system. This high degree of localization is evident in both the commensurate and in the incommensurate adsorbed layers.

## 3.5 Conclusions

Using a numerically exact ground state Quantum Monte Carlo method, we studied $p$-$H_2$ adsorption on the outer surface of near-spherical fullerenes. We performed calculations based on a simple model, in which all carbon atoms are included explicitly, i.e., corrugation of the surface of the fullerene is captured.

A single solid layer of $p$-$H_2$ is found to be thermodynamically stable on the fullerenes studied in this work. We find that the equilibrium adsorbed layer is commensurate with the corrugated surface of the fullerene. Such a layer is found to be compressible on one of the fullerenes (namely, $C_{36}$, for which a finite density of interstitials is accepted), incompressible on the others. On increasing the chemical potential, a discontinuous transition is observed to an incommensurate layer on all fullerenes, except for the largest one considered here ($C_{80}$).

The physics of the incommensurate layer is driven primarily by the interaction among $p$-$H_2$ molecules, which attempt to reproduce the same triangular arrangement as on an infinite plane, even when confined to moving on a spherical surface of radius as small as a few Å. Indeed, the incommensurate layer is very similar to that found using a simpler model of the system, describing the fullerene as a smooth spherical substrate. This simpler model yields results for the energetics and structure of the incommensurate layer in good quantitative agreement with those provided by the fully corrugated model; obviously, however, it is necessary to include corrugation in order to reproduce the commensurate layer. An interesting question that arises is whether a commensurate layer of helium may exist on these molecules; the theoretical studies performed so far have made use of a spherically averaged potential to describe the fullerenes [81].

Being solids with a high degree of particle localization, these $p$-$H_2$ systems do not appear as likely candidates for the observation of the elusive superfluid phase of *para*-hydrogen, for example, as defined by a decoupling of the hydrogen layer to an externally induced rotation of the fullerene.

In conclusion, this chapter has provided preliminary information on the structure and energetics of hydrogen films adsorbed to the exterior of buckyballs, though much remains to be answered. The experimental tests of several of the stated predictions could be carried

out, for example, by measuring the mass of adsorbed hydrogen on $C_l$ by examination of excitation spectra in a dipole trap [89, 90, 91].

# Chapter 4

# Molecular hydrogen isotopes adsorbed on krypton-preplated graphite

## 4.1 Introduction

In the recent neutron scattering investigation of $o$-$D_2$ films adsorbed on a krypton preplated graphite substrate [40] (a substrate of interest in the study of quantum films for decades [92]) mentioned in chapter 1, evidence of a stable "liquid-like" phase of $o$-$D_2$ down to $T \sim 1.5$ K was reported. Motivated by this experiment, we have undertaken a theoretical study of the low temperature phase diagram of $p$-$H_2$ and $o$-$D_2$ films adsorbed on such a substrate; the results of the study have been distilled to form this chapter. [1]

In a 2005 study [93], we determined that $p$-$H_2$ adsorbed upon a substrate consisting of graphite preplated with a *commensurate* monolayer of krypton forms two thermodynamically stable monolayer phases at low $T$, both *solid*; one is commensurate with the krypton layer, the other incommensurate. Shown in Figure 4.1 is the energy per particle $e(N)$ obtained as a function of coverage for this system, with the first minimum corresponding to the equilibrium commensurate coverage of $p$-$H_2$ with density $\theta_o$=0.0636 Å$^{-2}$, and the

[1] A version of this chapter has been published in:
Joseph Turnbull and Massimo Boninsegni. Physical Review B **76**, 104524 (2007).
Joseph Turnbull and Massimo Boninsegni. Journal of Low Temperature Physics **140**, 269 (2005).

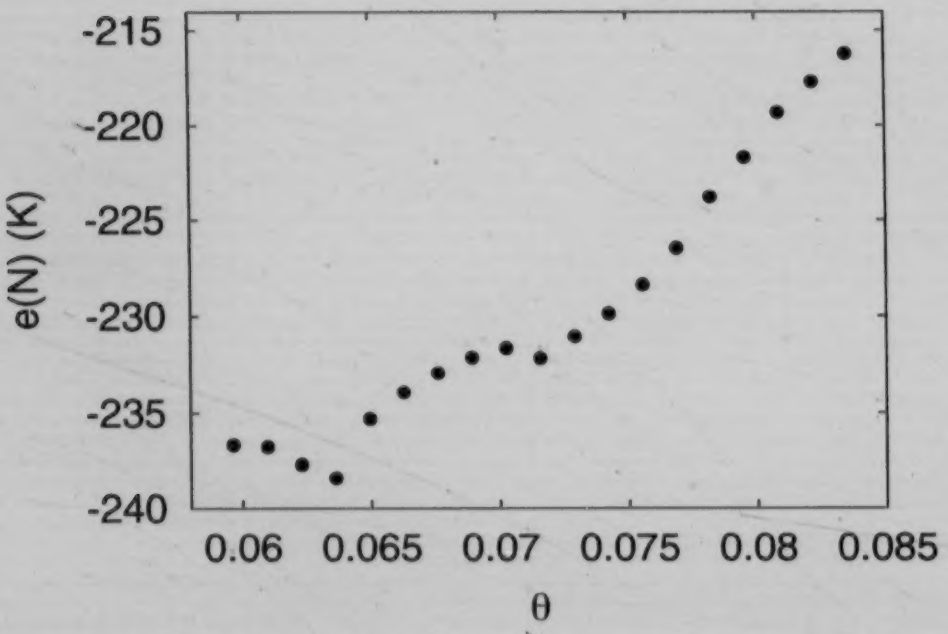


Figure 4.1: Energy per $p$-$H_2$ molecule $e(N)$ (in K) computed by PIGS, as a function of the coverage $\theta$ (in $\text{Å}^{-2}$).

second local minimum corresponding to the incommensurate coverage of $p$-$H_2$ with density $\theta_1$=0.0716 $\text{Å}^{-2}$, compressible up to $\theta_2$=0.0769 $\text{Å}^{-2}$. No evidence was observed of a liquid phase at $T = 0$ for these or any intermediate coverages, and quantum exchanges of $p$-$H_2$ were found to be greatly suppressed. Quantum zero-point motion in the direction perpendicular to the substrate was found to be less significant than that observed for $p$-$H_2$ adsorbed on lithium [39], from which one can conclude that this mechanism ought not yield a significant reduction in the melting temperature. In that study, while the Kr layer was modeled explicitly, the underlying graphite substrate was assumed smooth.

In this chapter, we again explore this system, but with two important modifications with respect to Ref. [93], namely *a*) we assume this time a *compressed* krypton layer preplating the graphite, i.e., *incommensurate* with the underlying substrate lattice structure, and *b*) we *explicitly* model corrugation of the underlying graphite substrate, in some of our simulations. Furthermore, in order to allow for a direct comparison with Ref. [40], we study adsorption of both $p$-$H_2$ and $o$-$D_2$.

Energetic, structural and superfluid properties are investigated using Path Integral ground state (PIGS) Monte Carlo simulations (see Chapter 2, Section 2.4), as well as the continuous-space worm algorithm [62, 63] (see Section 2.3) for simulations at finite temperature.

The main results of this chapter are the following:

1. No evidence is observed of a thermodynamically stable liquid phase for $o$-$D_2$ or $p$-$H_2$. In all cases, equilibrium phases are solid monolayers, commensurate with the underlying krypton plating, with coverage (i.e., 2D density) $\theta_o$=0.07253 Å$^{-2}$ for both isotopes.

2. An $o$-$D_2$ monolayer composed of commensurate domains separated by domain walls is found to be thermodynamically stable, compressible in a relatively small range of coverages.

3. Quantum exchanges of $p$-$H_2$ or $o$-$D_2$ molecules are essentially absent in the $T \to 0$ limit; consistently, no evidence of a finite superfluid response of either isotope is ever observed.

4. Our results are consistent with the presence of a "domain-wall fluid", as suggested in Ref. [40]. Though no dynamical information can be reliably extracted using the QMC techniques employed here, visual inspection of *instantaneous configurations* generated by our sampling procedure suggests that such a domain-wall fluid indeed forms; however, such a fluid does not support SF of either hydrogen isotope even at $T$=0. The hydrogen molecules are highly localized, with even those molecules making up the domain wall being localized by virtue of sitting at a potential minimum of the substrate.

The remainder of this chapter is organized as follows: Sec. 4.2 offers a description of the model used for our system of interest, including a discussion of the potentials and the justifications for the main underlying assumptions. Sec. 4.3 involves a brief discussion of the computational techniques and specific details of implementation, in addition to details of calibration and optimization. The results are presented in Sec. 4.4; finally, Sec. 4.5 is a summary of the findings and our concluding remarks.

## 4.2 Model

We consider a system of $N$ hydrogen molecules sitting above a substrate consisting of a single atomic layer of krypton, below which is a graphite substrate. The Kr layer consists of ($L$) point-like atoms, pinned at fixed positions $\mathbf{R}_k$ ($k = 1, 2, ..., L$) (an assumption justified by their relatively large mass). They are arranged in a perfectly two-dimensional triangular lattice, with a spacing [40] of 3.99 Å and sit at a height of 3.46 Å over the top layer of C atoms of the graphite substrate; this latter distance corresponds to the energetic minimum of the most accurate Kr-graphite potential available [94, 95], if graphite is regarded as smooth.

If a smooth graphite substrate is assumed, the model quantum many-body Hamiltonian is therefore as follows:

$$\hat{H} = -\frac{\hbar^2}{2m}\sum_{i=1}^{N}\nabla_i^2 + \sum_{i<j}V(r_{ij}) + \sum_{i=1}^{N}\sum_{k=1}^{L}U(|\mathbf{r}_i - \mathbf{R}_k|) + \sum_{i=1}^{N}\tilde{U}(z_i).$$

Here, $z_i$ is the height of the $i$th hydrogen molecule above the graphite surface. $V$ is the potential describing the interaction between any two hydrogen molecules, and $U$ represents the interaction of a hydrogen molecule with a Kr atom. Finally, $\tilde{U}$ represents the interaction of a hydrogen molecule with the smooth graphite substrate.

The interaction $V$ is described by the Silvera-Goldman potential [96], given in Section 2.5.3.

The interaction of a hydrogen molecule and a Kr atom is modeled using a standard 6-12 Lennard-Jones (LJ) potential; we make use of the Lorentz-Berthelot mixing rule [97, 98], yielding $\epsilon = 75.6$ K and $\sigma = 3.3$ Å, for our purposes consistent with current state-of-the-art potential energy surfaces (for example, numerical agreement is within $\approx$ 5% for the well depth) [99]. The Kr atomic monolayer is uniform, with each Kr atom kept fixed in its lattice position for the duration of the simulation.

We use a simple "3-9" potential to describe the interaction of hydrogen molecules with the smooth graphite substrate [100], i.e.,

$$\tilde{U}(z_i) = \frac{4C^3}{27D^2z^9} - \frac{C}{z^3} \tag{4.1}$$

where $C$=7913.24 Å$^3$ K and $D$=259.39 K are parameters derived from the original $p$-$H_2$-C Lennard-Jones parameters [87] ($\sigma$ = 3.18 Å, $\epsilon$ = 32.05 K) and the density of carbon atoms in graphite ($\rho = 0.114$ Å$^{-3}$).

The assumption built in (4.1) of a smooth graphite substrate seems justified, on account of the relatively large ($\sim$ 6 Å) distance between the hydrogen molecules and the substrate, due to the presence of the Kr layer. Nevertheless, corrugation may be important in this problem, given that the Kr layer is not registered with the underlying graphite substrate. Therefore, in order to gauge the effect of substrate corrugation, we performed a number of simulations with an explicitly modeled top layer of C atoms, placing a smooth graphite slab underneath. For these simulations, the pair-wise interaction between a hydrogen molecule and a C atom was taken to be the same LJ potential utilized to infer the "3-9" interaction of hydrogen molecules with a smooth substrate.

The results obtained using this composite substrate indicate no qualitative change in the physical character of the system as a result of introducing the smooth plane approximation for graphite. Quantitatively, the potential energy per particle, for example, was found to be $\sim$2 K lower when assuming explicit corrugation of the graphite substrate, a difference of less than 1%. Henceforth, therefore, we shall confine our discussion to the case of a smooth graphite substrate, i.e., model (4.1).

A slice of the effective potential energy surface for molecular hydrogen resting at its average height above the substrate is shown in Figure 4.2; included are the interactions with both the Kr monolayer and the graphite slab. There are two energetically degenerate sublattices of preferential adsorption sites for this geometry - these are denoted sublattice A and sublattice B.

The model (4.1) clearly contains important physical simplifications, such as the use of the highly simplified LJ and "3-9" potentials. Nonetheless, it seems a reasonable starting point, and even quantitatively we expect it to capture the bulk of the physical picture.

## 4.3 Computational Method

For this chapter, one method utilized is *Path Integral ground state* (PIGS), described in Chapter 2, Section 2.4. Some of the technical details of the calculation performed in this

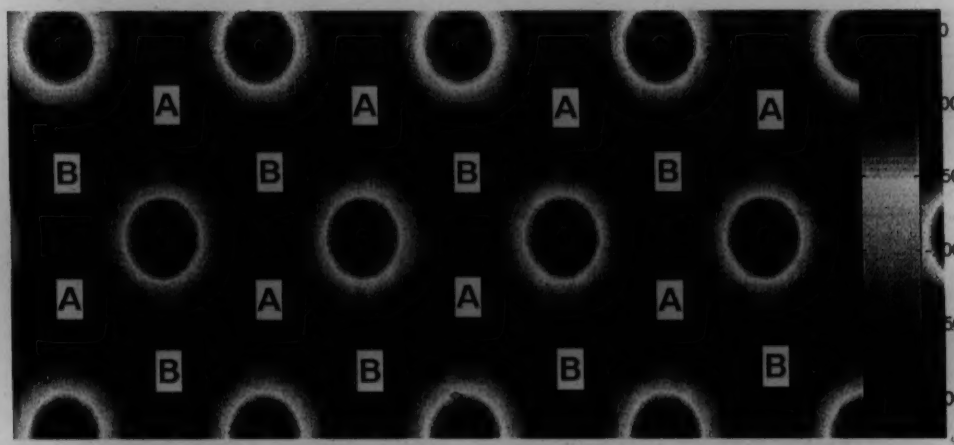


Figure 4.2: Potential energy surface, at the vertical equilibrium distance of molecular hydrogen, as a function of position. The two energetically degenerate sublattices of preferential adsorption sites, A and B, are shown. A *commensurate* coverage is defined as the occupation of one entire sublattice (also termed "$\frac{1}{2}$ filling").

work (mainly, the short imaginary time propagator) are the same as in Ref. [101].

The trial wave function utilized is of the Jastrow type:

$$\begin{aligned}\Psi_T(\mathbf{r}_1, \mathbf{r}_2, ...\mathbf{r}_N) &= \left(\prod_{i<j}^{N} e^{-v(r_{ij})}\right) \times \left(\prod_{i=1}^{N} e^{-w(z_i)}\right) \\ &\times \left(\prod_{i=1}^{N}\prod_{k=1}^{L} e^{-u(|\mathbf{r}_i - \mathbf{R}_k|)}\right) \end{aligned} \tag{4.2}$$

with pseudo-potentials $w$ ($p$-$H_2$-graphite and $o$-$D_2$), $u$ ($p$-$H_2$-Kr and $o$-$D_2$-Kr), and $v$ ($p$-$H_2$-$p$-$H_2$ and $o$-$D_2$-$o$-$D_2$) chosen as follows:

$$w(r) = \frac{\alpha}{z^3}\,, \quad u(r) = \frac{\gamma}{r^5} \text{ and } v(r) = \frac{\mu}{r^5} \tag{4.3}$$

The values of the parameters $\alpha = 30$ Å$^3$, $\gamma = 250$ Å$^5$ and $\mu = 750$ Å$^5$ were obtained empirically, by minimizing the energy expectation value computed in separate variational calculations. Using the trial wavefunction as defined above, we observe convergence of the ground state energy estimates with a projection time 0.250 K$^{-1}$, using a time step $\tau = (\nu/2560)$ K$^{-1}$, where $\nu = 1$ for $p$-$H_2$ and $\nu = 2$ for $o$-$D_2$.

Finite-temperature results were obtained making use of the *worm algorithm* (WA), described in Chapter 2 Section 2.3 and in references [62, 63]. The only input parameter to the WA, as for any finite temperature method, is the microscopic model (4.1). Just as in ground state simulations, an optimal value $\tau_w$ of the imaginary time step must be determined, for accurate and unbiased estimates of the observables to be obtained; for this system, satisfactory results are yielded by the choice $\tau_w = (\nu/320)\ \mathrm{K}^{-1}$.

Calculations for a range of $p$-$H_2$ and $o$-$D_2$ coverages were carried out, starting from an initial configuration of molecules sitting atop the Kr layer. The simulation cell consists of a $12\times 14$ triangular lattice of Kr atoms with 3.99 Å nearest neighbor spacing (resulting in a simulation box of dimension 47.880 Å $\times$ 48.3762 Å) [40]. Periodic boundary conditions are used in the three directions, but the simulation cell is chosen sufficiently large in the $z$ direction that they have no effect vertically, because of the strongly attractive character of the composite substrate (i.e., $p$-$H_2$ and $o$-$D_2$ molecules do not evaporate). It is important to note that to capture the features observed experimentally in Ref. [40] requires that a large number of particles be simulated (the simulation cell must be large enough to support at least two crystalline domains).

The systematic errors of our calculation are attributable to finite projection time (for the $T$=0 PIGS calculations) and the finite time step $\tau$ (for both PIGS and the WA). Based on comparisons of results obtained from simulations with different values of projection time and/or time step, we estimate our combined systematic error on the total energy per $p$-$H_2$ molecule to be of the order of 0.7 K or less (corresponding to less than 0.5%). The simultaneous use of a ground state and a finite temperature method allows us to obtain an independent check of our calculations in the $T \rightarrow 0$ limit, where the two methods must yield the same results, within statistical uncertainties.

## 4.4 Results

Physical quantities of primary interest, for both $p$-$H_2$ and $o$-$D_2$, include the energy per molecule, $e(\theta)$, and the superfluid fraction, $\rho_s$. PIGS ($T$=0) was used to compute $e(\theta)$ as a function of the coverage (two-dimensional density), $\theta$, from $\theta$=0.06735 $\mathrm{Å}^{-2}$ to $\theta$=0.09498 $\mathrm{Å}^{-2}$. For a subset of these coverages, the worm algorithm (WA) was employed to yield

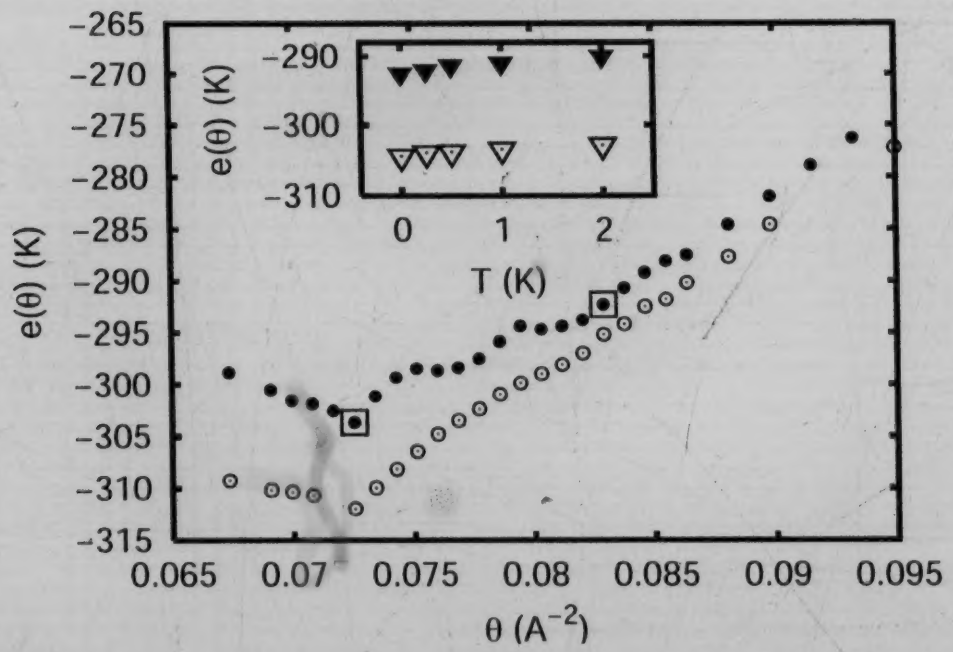


Figure 4.3: Energy per molecule $e(\theta)$ (in K) for $p$-$H_2$ ($\circ$), shifted by $-50$ K for clarity, and $o$-$D_2$ ($\bullet$) computed by PIGS ($T$=0), as a function of the coverage $\theta$ (in Å$^{-2}$). Inset: $e(\theta)$ calculated using WA for $o$-$D_2$ is shown with $\blacktriangledown$ for $\theta$=0.08389 Å$^{-2}$ and $\triangledown$ for $\theta$=0.07253 Å$^{-2}$, values marked with $\square$ on the $T$=0 $o$-$D_2$ curve.

finite temperature estimates for all of the above physical quantities, for a set of temperatures between $T$=5 K and $T$=0.25 K.

The results for $e(\theta)$ are shown in Figure 4.3; note that $e(\theta)$ for $p$-$H_2$ has been shifted by $-50$ K for clarity. In the case of $p$-$H_2$, the main feature is an energetic minimum at $\theta$=0.07253 Å$^{-2}$, corresponding to the formation of a thermodynamically stable solid layer, that is commensurate with the underlying krypton lattice. This coverage is approximately 8% greater than the equilibrium density of $p$-$H_2$ in strictly 2D [38]. Within the precision of the calculation, $e(\theta)$ is numerically consistent with the absence of other thermodynamically stable coverages, in the range explored in this work.

For $o$-$D_2$, we find that there is an energetic minimum at $\theta$=0.07253 Å$^{-2}$, again corresponding to a commensurate solid film. In addition, one finds two coverage ranges, separated by a cusp, where $\theta e(\theta)$, shown in Figure 4.4, has a positive second deriva-

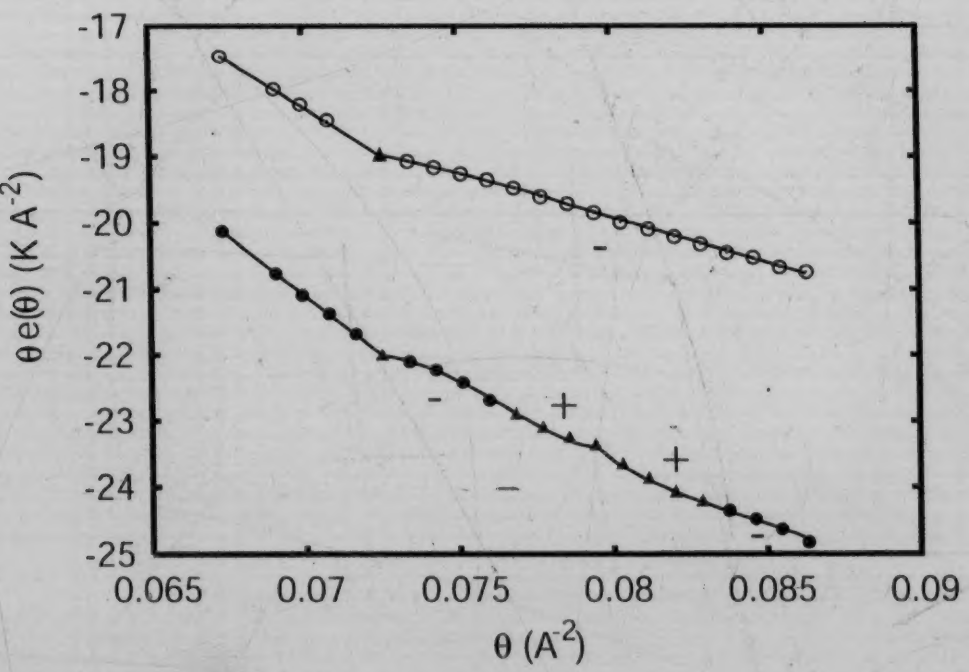


Figure 4.4: The product $\theta e(\theta)$ (in K$\text{Å}^{-2}$) for $p$-$H_2$ (○), and for $o$-$D_2$ (●) computed by PIGS ($T$=0), as a function of the coverage $\theta$ (in $\text{Å}^{-2}$). ▲ denote coverages within regions of positive curvature.

tive (meaning that these configurations satisfy the condition of positive compressibility, $d\mu/d\theta = d^2[\theta e(\theta)]/d\theta^2 > 0$, and are thus thermodynamically stable); we will call the first of these IC-I, and the second IC-II. IC-I extends from $\theta$=0.07598 $\text{Å}^{-2}$ to $\theta$=0.08030 $\text{Å}^{-2}$, while IC-II extends from $\theta$=0.08030 $\text{Å}^{-2}$ to $\theta$=0.08635 $\text{Å}^{-2}$. The much richer behavior of $e(\theta)$ in the case of $o$-$D_2$, is a direct consequence of the greater mass, and reduced zero-point motion, of this isotope; as a result, the potential energy plays a greater role in shaping the physical properties. Phases of intermediate coverages found for $o$-$D_2$ are apparently "washed out" by zero-point motion in the case of $p$-$H_2$. While this result is surprising, similar anomalous behavior is noted in related studies [73, 102].

Of particular interest for the present analysis is IC-II, where the $o$-$D_2$ is found to form a structure best characterized as being composed of several crystalline domains commensurately occupying one of the two triangular sublattices available. Between these commensurate domains are regions of high $o$-$D_2$ density - domain walls. Molecules that

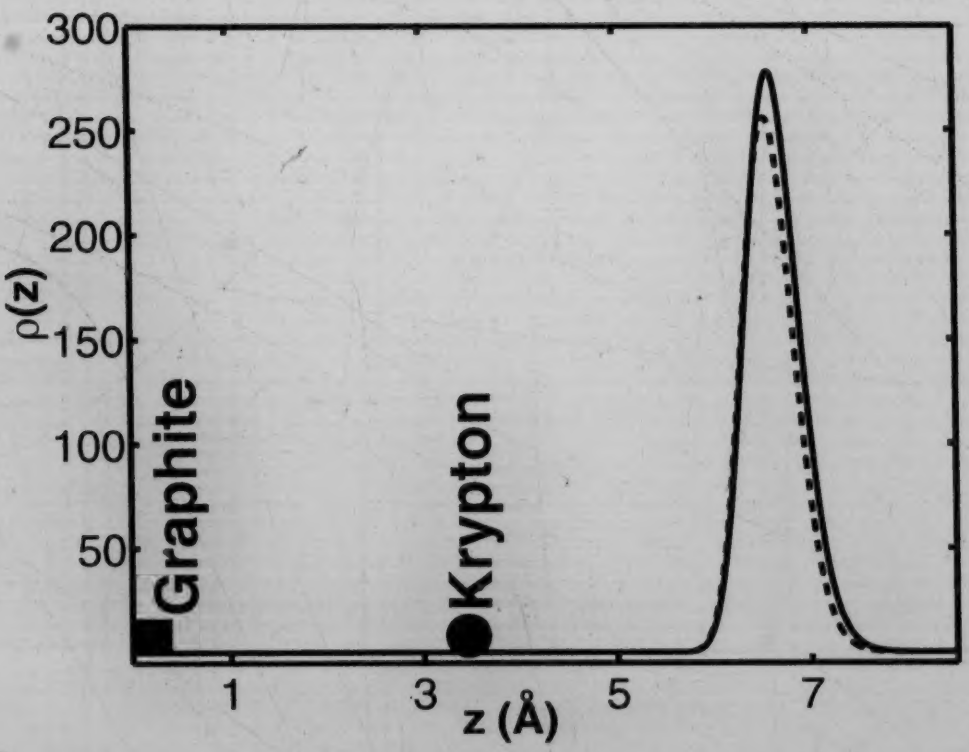


Figure 4.5: Density profile of $o$-$D_2$ adsorbed to the composite substrate for $\theta$=0.08389 Å$^{-2}$ and $\theta$=0.07253 Å$^{-2}$ at $T$=1 K (solid line and dashed line respectively). The square represents the position of graphite (at $z$=0 Å) and the circle represents the position of the Kr layer (at $z$=3.46 Å). Plots have been normalized to particle number.

are part of these domain walls have a decreased average interparticle distance. One may expect that such $o$-$D_2$, having the same zero-point motion as $o$-$D_2$ in the commensurate domains, would have a greater likelihood of quantum exchange, in particular if there is domain-wall disorder. Indeed, IC-II includes precisely the coverages reported in the experiments of Ref. [40] to exhibit anomalous fluid-like signatures down to $T$=1.5 K, well below the expected freezing point.

In order to provide accurate permutation statistics and superfluid density estimates, additional simulations were carried out for several coverages at finite temperature using the worm algorithm. Figure 4.3, inset, shows the energy values obtained in the range of temperature 0.25 K $\leq$ T $\leq$ 5 K, for $\theta$=0.07253 Å$^{-2}$ and $\theta$=0.08389 Å$^{-2}$.

Shown in Figure 4.5 are vertical density profiles, $\rho(z)$, for $\theta$=0.07253 Å$^{-2}$ and $\theta$=0.08389 Å$^{-2}$ at $T$=1 K. One can see that the vertical extent of the $o$-$D_2$ film is slightly enhanced for increased coverages.

While dynamical information cannot be extracted using the computational techniques employed here, one does have access to real-space instantaneous configurations of the system, from which one can extract qualitative insight, and potentially use to preclude particular system behaviors. Such representative many-particle configurations are shown in Figures 4.6, 4.7, 4.8 for $o$-$D_2$ and $p$-$H_2$ with $\theta$=0.07253 Å$^{-2}$ at $T = 0$, and for $o$-$D_2$ with $\theta$=0.08389 Å$^{-2}$ at $T$=0.5 K. In each, we find a high degree of particle localization, even along the domain walls observed in 4.8. No single configuration observed was found to be inconsistent with the instantaneous configurations one would necessarily observe in a domain-wall fluid, while the spatial configuration of domain-walls was not fixed as the system evolved in Monte Carlo time (which, we must again stress, cannot be used directly to infer anything about the real-time dynamics).

Finally, consistent with the high degree of $o$-$D_2$ localization observed, permutations are found to not take place at any temperature for any coverage examined, and, accordingly, the finite temperature estimator for the superfluid density consistently yields a value of $\rho_s$=0. In light of the absence of structural and energetic differences found between $T$=0 and $T$=0.25 K, it is unlikely that novel phases of $o$-$D_2$ (namely, phases with a finite superfluid density) remain unexplored at intermediate temperatures.

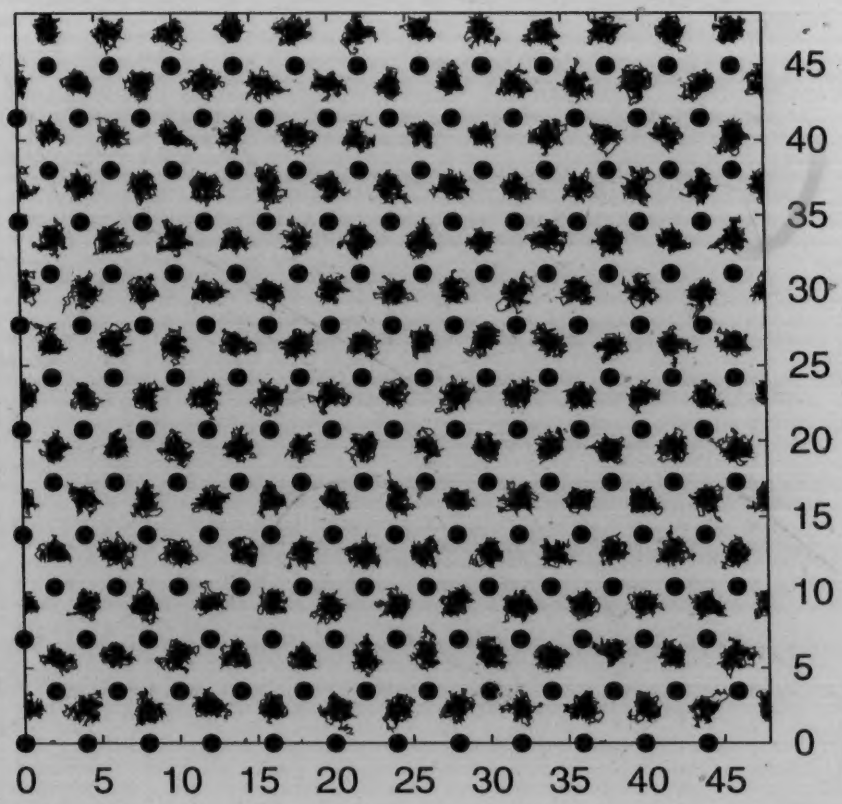


Figure 4.6: Snapshots of typical configurations of $p$-$H_2$ molecules, with $\theta$=0.07253 Å$^{-2}$ at $T$=0 K, adsorbed to the graphite/compressed Kr substrate. The positions of all molecules at each one of the imaginary time slices are shown as discrete paths. Distances are expressed in Å.

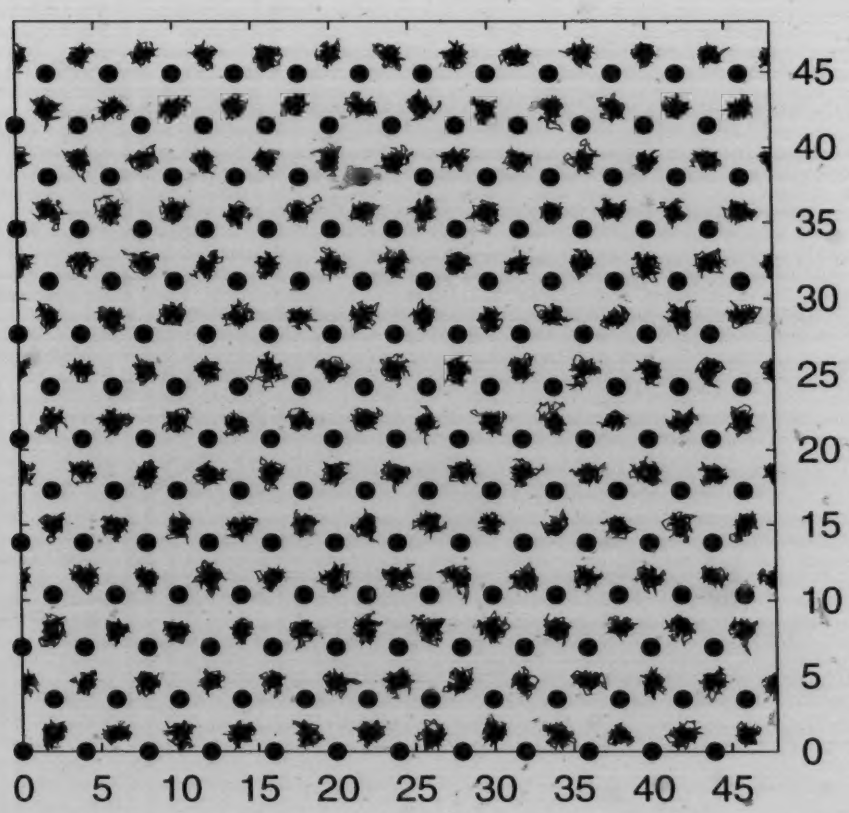


Figure 4.7: Snapshots of typical configurations of $o$-$D_2$ molecules, with $\theta$=0.07253 Å$^{-2}$ at $T$=0 K, adsorbed to the graphite/compressed Kr substrate. The positions of all molecules at each one of the imaginary time slices are shown as discrete paths. Distances are expressed in Å.

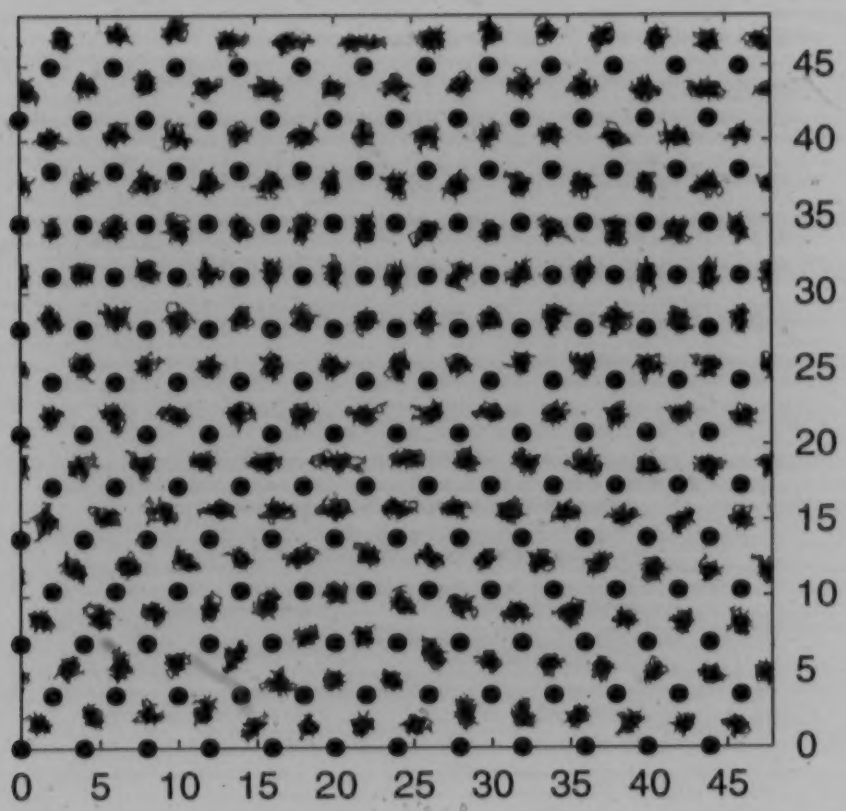


Figure 4.8: Snapshots of typical configurations of $o$-$D_2$ molecules, with $\theta$=0.08389 Å$^{-2}$ at $T$=0.5 K, adsorbed to the graphite/compressed Kr substrate. The positions of all molecules at each one of the imaginary time slices are shown as discrete paths. Distances are expressed in Å.

## 4.5 Discussion

Using numerically exact ground state Quantum Monte Carlo (PIGS) and finite-temperature path integral Monte Carlo (worm algorithm) methods, we studied $p$-$H_2$ and $o$-$D_2$ adsorption onto a graphite substrate preplated with a compressed krypton monolayer. We performed calculations based a simple model, in which graphite corrugation is ignored, the Kr atoms in the spacer layer are assumed static and point-like, and $p$-$H_2$($o$-$D_2$)-substrate interactions are given by Lennard-Jones type potentials.

Using an exact ground state technique, for both $p$-$H_2$ and $o$-$D_2$, we find that a solid monolayer commensurate with the Kr layer is thermodynamically stable, and, in both cases, is the coverage corresponding to the minimum energy per particle. For $o$-$D_2$, we also find that there are two distinct compressible incommensurate solid regions, with the denser region, IC-II, corresponding to regions of commensuration separated by domain walls. Investigation of this coverage region at finite temperature, using the worm algorithm, down to $T$=0.25 K, yields no evidence of superfluidity, consistent with our observation of a high degree of localization of $o$-$D_2$ molecules, in particular those molecules along the domain-walls. No non-identity permutations are found to take place, though they are sampled efficiently.

Though our simulations support the notion of a "domain-wall fluid", this mechanism is found not to support superfluidity of either hydrogen isotope.

There are obviously several sources of uncertainty in this calculation which need to be discussed. The potentials used to describe the interactions between the $p$-$H_2$ and the substrate are very rough; this does not seem too important an issue, as far as the interaction of $p$-$H_2$ molecules with graphite is concerned, given the relatively large average distance at which molecules sit, supported by calculations using explicit corrugation of the graphite substrate. On the other hand, a more realistic interaction potential between $p$-$H_2$ and krypton may *quantitatively* alter the energetics shown here. Despite these issues, and other simplifications, it does not seem likely that the qualitative structural information will change. Thus, we conclude this system is not a good candidate for further consideration in the search for superfluid $o$-$D_2$ or $p$-$H_2$.

The results shown here strengthen the case that frustration arising from incommensu-

ration does not lead to the formation of a stable superfluid phase of molecular hydrogen at low $T$. The problem here seems to be that the corrugation of the substrate, while inducing incommensuration, also promotes particle localization.

# Chapter 5

# Para-hydrogen in two dimensions: incommensuration and disorder

## 5.1 Introduction

We remind the reader of the 1997 study by Gordillo and Ceperley [52] (GC) outlined in the introduction, where it was proposed that a significant lowering of the equilibrium density of 2D $p$-$H_2$, and the ensuing stabilization of a low temperature "liquid" phase, could be achieved by embedding a $p$-$H_2$ fluid in a regular crystal of identical scatterers (e.g., foreign atoms or molecules), incommensurate with the equilibrium crystal structure of pure 2D $p$-$H_2$. Path Integral Monte Carlo (PIMC) simulations of such a model system yielded some evidence of a possible superfluid transition at $T \sim 1$ K. However, the size of the simulated system was very small (of order of 10 $p$-$H_2$ molecules). A subsequent PIMC study, comprising up to ten times as many particles, strongly suggests that *a*) the equilibrium phase of $p$-$H_2$ in such a setting is not liquid, but instead exhibits long range crystalline order, and *b*) the observation of superfluidity in Ref. [52] is merely a finite-size effect.

In this chapter[1], we report first the results of a theoretical study which seeks to clarify the physics of this system by repeating the simulations of Ref. [52] and Ref. [53], using

[1] A version of this chapter has been submitted for publication.
Joseph Turnbull and Massimo Boninsegni. Physical Review B (2008). See ArXiv:0807.2210

the wórm algorithm. In our simulations for the smallest system size, we obtain a finite superfluid signal in agreement with both previous studies; however, the finite superfluid signal persists for somewhat larger systems, in contrast with Ref. [53]. We augment these results by studying the structural properties of a much larger manifestation of the system, containing hundreds of impurities and $p$-$H_2$ molecules. Evidence is obtained that the $p$-$H_2$ forms a perfect crystal with a large unit cell (having non-trivial structure), devoid of interstitials. Such a phase, masked before by the smaller system sizes (for which the obtained structure is artificially frustrated), is necessarily insulating. Thus, we conclude that the observed superfluid properties in small systems are finite-size artifacts, and that $p$-$H_2$ in this geometry is a regular quantum solid in the thermodynamic limit.

We next explore the behavior of $p$-$H_2$ in a 2D and disordered environment. Our aim is to determine whether a non-crystalline equilibrium phase, displaying long-range superfluid coherence, may arise as a result of the frustration of solid long-range order induced by the random potential. That disorder should promote SF is certainly not obvious, and may even be counter-intuitive. In fact, disorder is known to promote *localization*, with the ensuing *disappearance* of SF in a system of hard core bosons [54]. However, recent numerical work has yielded evidence of a possible "superfluid glassy" phase of condensed helium, characterized by simultaneous broken translational invariance (and therefore nonzero shear modulus) *and* SF, with no diagonal long-range order [55]. It is conceivable that a similar phase of $p$-$H_2$ could arise in disorder.

Specifically, we simulate a fluid of $p$-$H_2$ molecules moving in 2D in the presence of a static potential generated by a random distribution of identical impurities, averaging the results over several independent realizations of the external potential. We have assumed a specific simple model potential, so as to describe the interaction between each scatterer and the $p$-$H_2$ molecules, and varied the overall strength of the disordering potential by changing the density of impurities. The main result of this study is a *null* one, i.e., even though we observe exchanges of small groups of molecules, they have a local character, i.e., long permutation cycles spanning the entire system do not occur; as a result, a finite superfluid signal never materializes in the low temperature and thermodynamic limits. We observe a glassy phase, with broken translational invariance, but we also clearly observe that $p$-$H_2$ molecules *locally* recreate the triangular lattice structure associated with bulk

2D $p$-$H_2$, interrupted by the underlying impurity matrix.

Based on this finding, as well as on the null results yielded by various simulation works carried out over the past few years, we propose that a superfluid phase of 2D $p$-$H_2$ will *not* be observed, in the absence of some indirect physical mechanism capable of renormalizing (weakening) the effective interaction among molecules.

The remainder of this chapter is organized as follows: Sec. 5.2 offers a description of the model used for our systems of interest, including a discussion of the potentials and the justifications for the main underlying assumptions. Sec. 5.3 involves a brief discussion of the computational techniques and specific details of implementation, in addition to details of calibration and optimization. The results are presented in Sections 5.4, 5.5, and 5.6; finally, Sec. 5.7 is a summary of the findings and our concluding remarks.

## 5.2 Model

We consider a system of $N$ hydrogen molecules (composite bosons) in the *para* nuclear spin state, intercalated within a strictly 2D array of identical impurities, the entire system enclosed within a simulation cell of sides $L_x$ and $L_y$ ($\mathcal{A}$=$L_x \times L_y$), with periodic boundary conditions in both directions. All of the ($M$) impurities and hydrogen molecules are regarded as point particles, with impurities fixed in space at positions $\mathbf{R}_k$, $k = 1, ..., M$. The model quantum many-body Hamiltonian is therefore as follows:

$$\hat{H} = -\frac{\hbar^2}{2m}\sum_{i=1}^{N}\nabla_i^2 + \sum_{i<j}V(r_{ij}) + \sum_{i=1}^{N}\sum_{k=1}^{M}U(|\mathbf{r}_i - \mathbf{R}_k|) \qquad (5.1)$$

Here, $m$ is the mass of a hydrogen molecule, $\{\mathbf{r}_j\}$ (with $j$=1,2,...,$N$) are the positions of the hydrogen molecules, and $r_{ij} \equiv |\mathbf{r}_i - \mathbf{r}_j|$. $V$ is the potential describing the interaction between any two hydrogen molecules, and $U$ represents the interaction of a hydrogen molecule with an impurity. All pair potentials are assumed to depend only on relative distances.

The interaction $V$ is described by the Silvera-Goldman potential described in chapter 2. The interaction of a hydrogen molecule with each impurity scatterer is modeled using

a standard 6-12 Lennard-Jones (LJ) potential, with parameters $\epsilon = 9.54$ K and $\sigma = 3.75$ Å [52].

In addition to restricting the dimensionality of the system to $d$=2, the model (5.1), which is identical to that assumed in Ref. [52] and Ref. [53], clearly contains important physical simplifications, such as the restriction to additive pairwise interactions (to the exclusion of, for example, three-body terms), all taken to be central, and the use of the highly simplified LJ potential. As in previous studies [53], however, we are primarily interested in examining the fundamental physics contained in a general many-body problem described by a Hamiltonian such as (5.1), rather than making quantitative predictions about an actual experimental system (though it should be noted that an experimental realization may be feasible [103, 104]).

## 5.3 Computational Details

In this study, finite-temperature results were obtained making use of the continuous-space *worm algorithm*, described in Section 2.3, and in References [62] and [63].

As usual, the only input in the simulations are the Hamiltonian and the temperature. As in Chapters 3 and 4, the calculation has associated to it a finite time step error, which can be made sufficiently small by taking the time step short enough; for all of the system sizes explored, it was found that convergence of the energy estimate is achieved (within statistical uncertainty) using a value of the time step $\tau_w = 1/640$ K$^{-1}$. Convergence for properties such as the superfluid density is reached using a much longer time-step, and this property has been taken advantage of where indicated. Based on comparisons of results obtained from simulations with different values of the time step, we estimate our systematic error on the total energy per $p$-$H_2$ molecule (the observable that is most sensitive to time-step error) to be of the order of 0.1 K or less (of order 0.6%).

### 5.3.1 Simulations

All of the simulation results presented below are obtained starting from an initial configuration of hydrogen molecules randomly dispersed within the impurity array. We have

studied the physical behavior of the system at sufficiently low temperature, with the aim of extrapolating the results to the $T$=0 limit. Specifically, the lowest temperature for which estimates were obtained is $3.125\times10^{-2}$ K.

Calculations for a range of $p$-$H_2$ coverages were carried out for $T = \{4.0, 2.0, 1.0, 0.500, 0.250, 0.125, 0.0625, 0.03125\}$ K, starting from an initial configuration of hydrogen molecules randomly dispersed within the impurity crystal. Three system sizes were examined, with the simulation cell containing triangular lattices composed of 2×2 (20×17.32 Å$^2$), 4×4 (40×34.64 Å$^2$), and 5×6 (50×51.96 Å$^2$) impurity atoms with 10.0 Å nearest neighbor spacing. For each lattice size, a $p$-$H_2$ coverage $\theta = N/\mathcal{A} \cong 0.0381$ Å$^{-2}$ was examined (corresponding to $N$=13, 53, and 99 $p$-$H_2$ molecules respectively); for the 5×6 lattice, a range of coverages between $0.030\ \text{Å}^{-2} \leq \theta \leq 0.045\ \text{Å}^{-2}$ was explored as well to confirm, using the worm algorithm, the equilibrium $p$-$H_2$ density. These results are discussed in section 5.4.

In order to assess the robustness of our predictions in the thermodynamic limit, we have also performed simulations for a 10×12 (100×103.92 Å$^2$) lattice of impurities, at $T$=4 K and $T$=0.25 K (the latter using a 4× larger time step). We use these results largely to infer structural properties. These results are also discussed in section 5.4.

Our simulations for a disordered environment are carried out with two different cells. The first is a 30×30 Å$^2$ square cell, wherein we arrange $M$=12, 16, and 20 impurities (corresponding to impurity densities $\Omega$=0.0133 Å$^{-2}$, 0.01778 Å$^{-2}$, and 0.0222 Å$^{-2}$ respectively) in a completely random fashion. The second cell, with dimensions 40×34.64 Å$^2$, contains $M$=16 randomly placed impurities (corresponding to $\Omega$=0.01155 Å$^{-2}$). For each impurity density, eight different realizations are considered (i.e., different random positions of the impurities). These results are discussed in section 5.5.

In a slightly different arrangement, we have considered a 40×34.64 Å$^2$ cell, in which we first arranged $M$=16 impurities on a regular triangular lattice (details are given below), and then applied to each impurity are random displacements $D_{0,1} \in$(0.0,1.0) Å, $D_{0.5,2} \in$(0.5,2.0) Å, $D_{0,2} \in$(0.0,2.0) Å, and $D_{1,2} \in$(1.0,2.0) Å. Eight such "nearly-periodic" impurity matrices were realized in each case (32 total). For each realization, calculations for a range of $p$-$H_2$ coverages were carried out for selected coverages. These results are discussed in section 5.6.

For each realization of a disordering potential, as well as for every regular arrangement of scatterers, we performed calculations for a range of $p$-$H_2$ coverages, at low temperature (as low as 0.03 K), in all cases starting from an initial configuration of hydrogen molecules randomly dispersed within the impurity crystal. For each impurity matrix, energetic and structural properties are studied; in general, these remain unchanged below $T$=2 K. Moreover, the superfluid properties of the system are investigated through the direct computation of the superfluid density, as well as of the one-body density matrix, both computed as a function of temperature.

In all energy calculations, estimates of the contribution to the potential energy arising from particles (and their periodic images) beyond the interaction cutoff radii, $r_c = \{8.2, 14.2, 16.5, 22.0, 48.5\}$ Å (in ascending order of system size), are added to the results.

## 5.4 Results: $p$-$H_2$ intercalated within a periodic 2D impurity matrix

In order to obtain the ground state equation of state of the system, we have computed the energy per particle $e$ as a function of coverage $\theta$, extrapolating the results to the $T \rightarrow 0$ limit. Our results (Fig. 5.1) are identical, within statistical uncertainties, to those of Ref. [53]. In particular, no significant dependence of the energy upon temperature is observed for $T$ below 2 K, and even the dependence on the size of the system (for all but the smallest one considered) is within, or very close to, statistical error. Our results are also in *qualitative* agreement with those of Ref. [52], although estimates offered therein are shifted upwardly by as much as a few K (the reasons for this discrepancy remain unclear, as merely finite size corrections can not account for the difference).

The equilibrium 2D density $\theta_e$ is 0.0381 Å$^{-2}$, which, as we shall show below, corresponds to a *commensurate* superstructure formed by the $p$-$H_2$ molecules. Furthermore, a stability analysis of the data for $e(\theta)$ (shown in the inset of Fig. 5.1, upon applying the process described in Chapter 4) indicates that doping above $\theta_e$ will *not* result in a homogeneous phase, but rather in the *coexistence* of two (commensurate) phases.

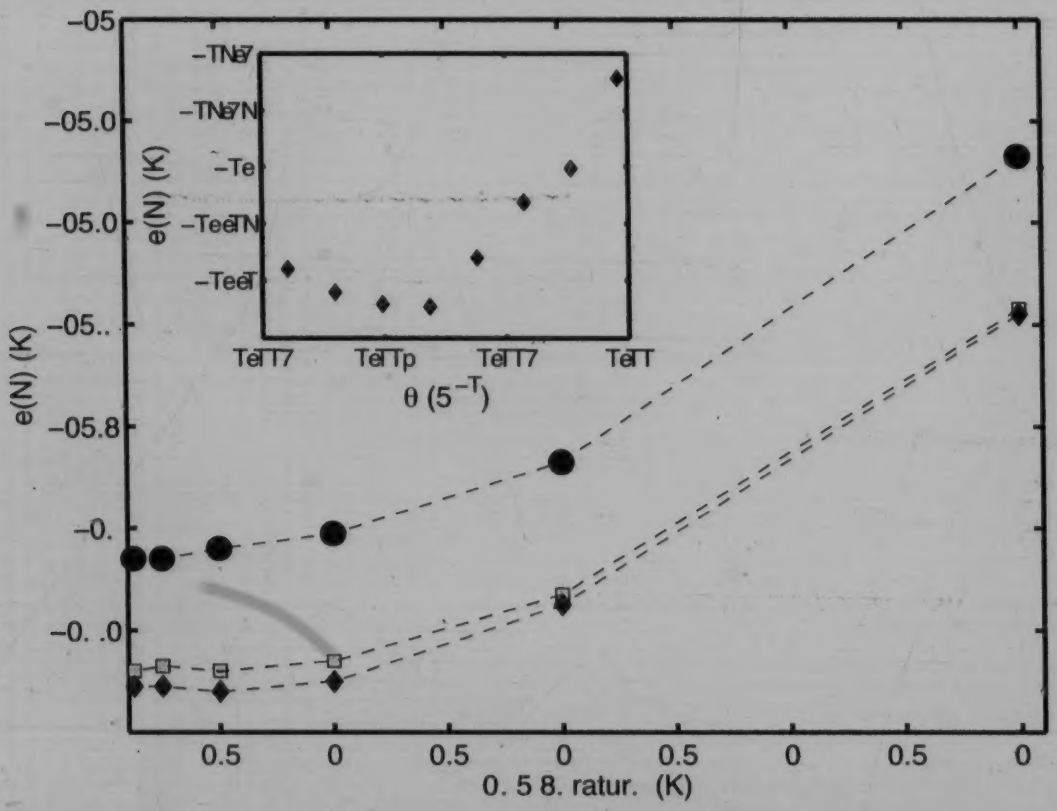


Figure 5.1: Energy per $p$-$H_2$ molecule for a regular crystalline arrangement of impurities, at the equilibrium coverage $\theta_e$=0.0381 Å$^{-2}$ as a function of the temperature, for different system sizes. Different symbols show estimates for lattices of 4 (circles), 16 (squares) and 30 (diamonds) impurities. Inset shows the energy per molecule computed at $T$=1 K as a function of the coverage $\theta$, obtained for a system of 30 impurities.

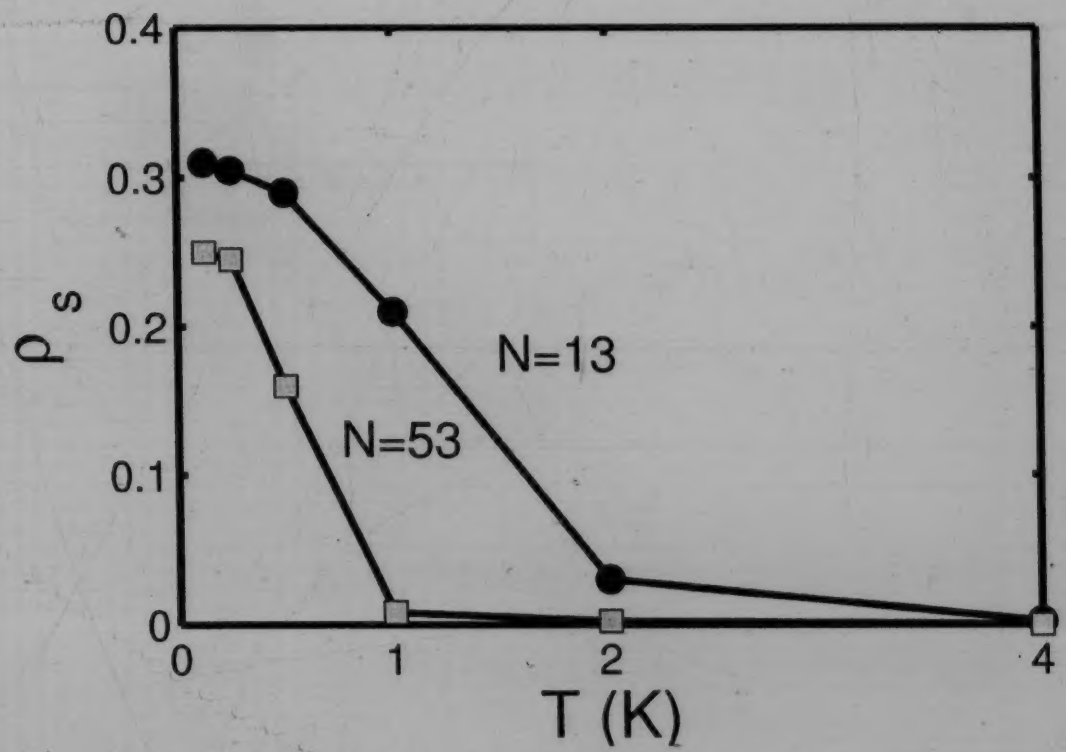


Figure 5.2: The superfluid density, $\rho_s$, for the 2×2 system (■), and the 4×4 system (•). Lines are guides to the eye.

Figure 5.3 shows a snapshot of the $p$-$H_2$ world lines for a system with equilibrium $p$-$H_2$ coverage $\theta$=0.0381 Å$^{-2}$ at $T = 0.25$ K. The positions of all $p$-$H_2$ molecules at each one of the imaginary-time slices are shown as discrete paths, while the fixed impurities are shown as solid circles; it *appears* that the $p$-$H_2$ arrange themselves on a kagomé lattice, with an additional number of $p$-$H_2$ molecules corresponding to an interstitial density of $\sim$10%. The spread of the imaginary-time path for each $p$-$H_2$ molecule gives a measure of the zero-point motion.

The results for the superfluid density (see Figure 5.2) in the 4×4 system, which are in agreement with the results obtained for the 2×2 system, naively may seem to indicate a convergence to $\rho_s(T = 0)$=0.25 ± 0.02. In order to provide an estimate of the transition temperature, $T_c$ using these preliminary results, we first attempt to correct for finite-size effects by using the Kosterlitz-Thouless recursion relations to determine the maximum separation distance between vortex pairs, $d$, and the vortex core energy, $E$, which lead to an optimal fit of our $\rho_s(T)$ data for a given linear system dimension $L$, and then extrapolate the numerical expression obtained for $\rho_s(T)$ in the $L \rightarrow \infty$ limit.

This KTRG process [105] involves solving the recursion relations

$$\frac{\partial \rho_s(T,x)}{\partial x} = \left[\frac{-4\pi^3\hbar^2}{mk_bT}\right] \xi^2(T,x)\rho^2(T,x) \tag{5.2}$$

$$\frac{\partial \xi_s(T,x)}{\partial x} = 2\xi(T,x) - \left[\frac{\pi\hbar^2}{mk_bT}\right] \xi(T,x)\rho(T,x) \tag{5.3}$$

with initial conditions $\rho_s(T, x = 0)$=$\theta\rho_s(T = 0)$, $\xi(T, x = 0) = e^{-\beta E}$, with integration from $x$=0 to $x$=ln($\frac{L}{2d}$), where $m$ is the mass and $\theta$ is the density of $p$-$H_2$, and $\xi$ is proportional to the vortex fugacity. The numerical integration was performed using an adaptive-stepsize method of Runge-Kutta type [106]. From this analysis, we obtain optimal values $E$=1.51 ± 0.04 K and $d$=4.6 ± 0.1 Å, which result in a transition temperature of $T_c$=0.29 ± 0.07 K. However, as will be shown below, such a scaling analysis is not necessarily robust.

Analysis of the one-body density matrix also reveals a rapid exponential decay out to 4.5 Å, followed by a Kosterlitz-Thouless power-law decay, indicative of off-diagonal quasi-long-range order.

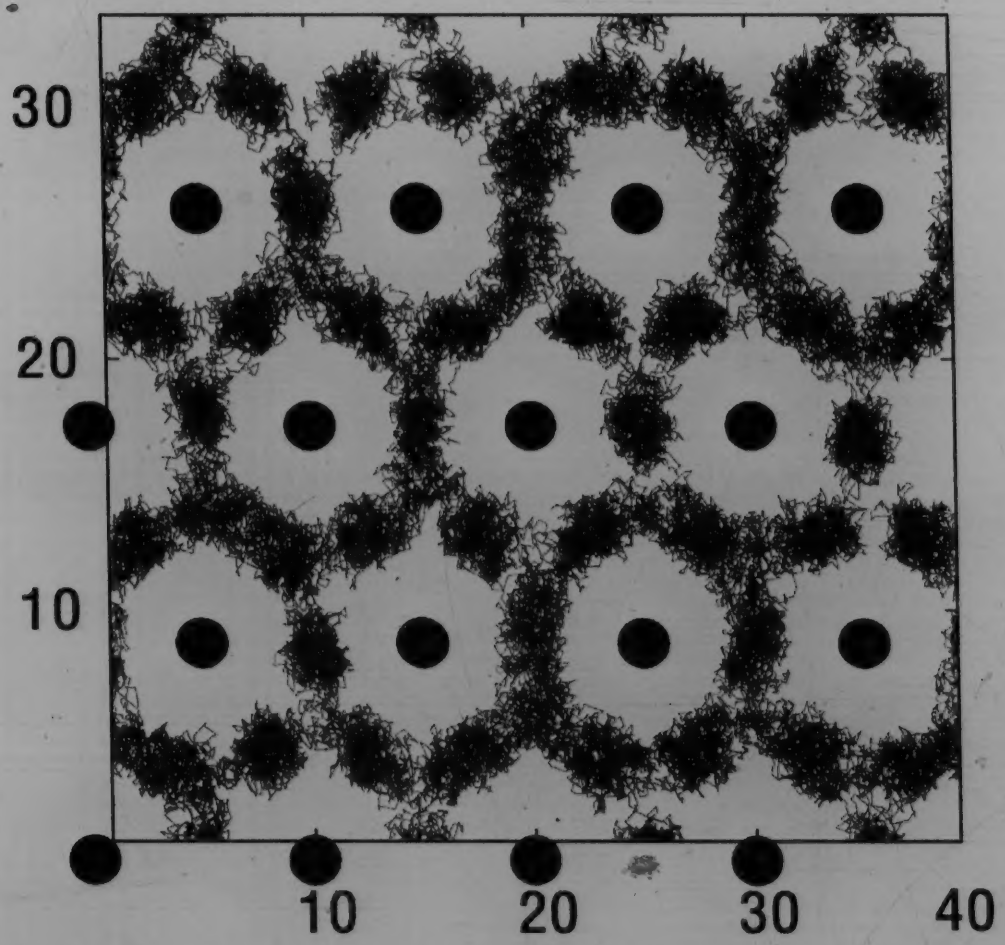


Figure 5.3: Snapshot of a typical configuration of $p$-$H_2$ molecules at $T = 0.25$ K for $\theta$=0.0381 Å$^{-2}$ on the 4×4 system, intercalated within the periodic 2D fixed impurity matrix with density $\Omega$=0.01155 Å$^{-2}$. The positions of all $p$-$H_2$ molecules at each one of the imaginary time slices are shown as discrete paths, while impurities are shown as solid circles. All distances are expressed in Å.

However, upon increasing the system size to the 5×6 cell, the finite superfluid signal goes down to a mere 5%, vanishing altogether for the 10×12 cell; concurrently, the one-body density matrix displays a clear exponential decay with distance, when evaluated for these larger size systems. This behavior persists at and below $T$=0.25 K. It should be noted that the change of behavior observed on extending the system size is *not* attributable to some loss of efficiency of the simulation method in sampling long permutations of $p$-$H_2$ molecules. While this would be certainly an issue with conventional PIMC, the continuous-space Worm Algorithm does not suffer from any such system size limitation, as shown by a number of calculations carried out over the past few years, e.g., for extended defects in solid helium, including several thousand particles [107, 108].

For the 10×12 lattice of impurities at $T$=4 K, we also confirm an equilibrium coverage of $\theta_e$=0.0385 Å$^{-2}$ (corresponding to 400 $p$-$H_2$ molecules, precisely $3+\frac{1}{3}$ times the impurity density). Shown in Figure 5.4 is a snapshot of the $p$-$H_2$ world lines for the noted conditions - the positions of all $p$-$H_2$ molecules at each one of the imaginary-time slices are shown as discrete paths, while the fixed impurities are shown as solid circles. The spread of the imaginary-time path for each $p$-$H_2$ molecule gives a measure of their quantum delocalization (zero-point motion). One can immediately identify a trihexagonal tiling of $p$-$H_2$ corresponding to a kagomé lattice commensurate with, and having three times the density of the impurity background (i.e. three $p$-$H_2$ per centroid of every nearest-neighbor impurity triplet). Superimposed over this structure is an additional 1/3 coverage of $p$-$H_2$ molecules arranged on a triangular lattice; sites of this triangular lattice correspond to regions of the total structure having four $p$-$H_2$ molecules per centroid of nearest-neighbor impurity triplets (schematically shown in inset of Fig. 5.4). As mentioned above it is found, using the procedure described in Ref. [109], that this phase is incompressible.

Fundamental theoretical arguments [49], as well as simulation of hard core bosons on the triangular lattice [110] (with which the commensurate phase of $p$-$H_2$ described above bears significant similarities and seems a close physical realization) strongly suggest that the commensurate phase of $p$-$H_2$ found here is not *supersolid*. Accurate scaling of numerical results obtained for systems of sufficiently different and large sizes is *of paramount importance* in the presence of an underlying crystal, with the ensuing loss of

translational invariance, in order to afford a reliable extrapolation of the physical behavior characterizing the thermodynamic limit.

The system of interest here offers a chief example of the importance of this aspect. A large size is simply required in order for the actual, non-trivial equilibrium structure of the system to be possible. Our analysis reveals that $p$-$H_2$ forms a commensurate crystal phase with no interstitials or defects. Such a phase, masked for smaller system sizes (for which, while the obtained structure is artificially frustrated, remnants of the crystalline phase are noticeable only *a posteriori*), is insulating, with explicit calculations of the superfluid density lending confirmation. Thus, in agreement with Ref. [53], we conclude that all previously reported superfluid properties are finite-size artifacts, and that $p$-$H_2$ in this geometry is necessarily a regular quantum solid in the thermodynamic limit.

This does not mean that exchanges of $p$-$H_2$ molecules do *not* take place; however, they are largely local in character; long cycles spanning the whole system - necessary for a finite superfluid response - are exponentially suppressed in the thermodynamic limit.

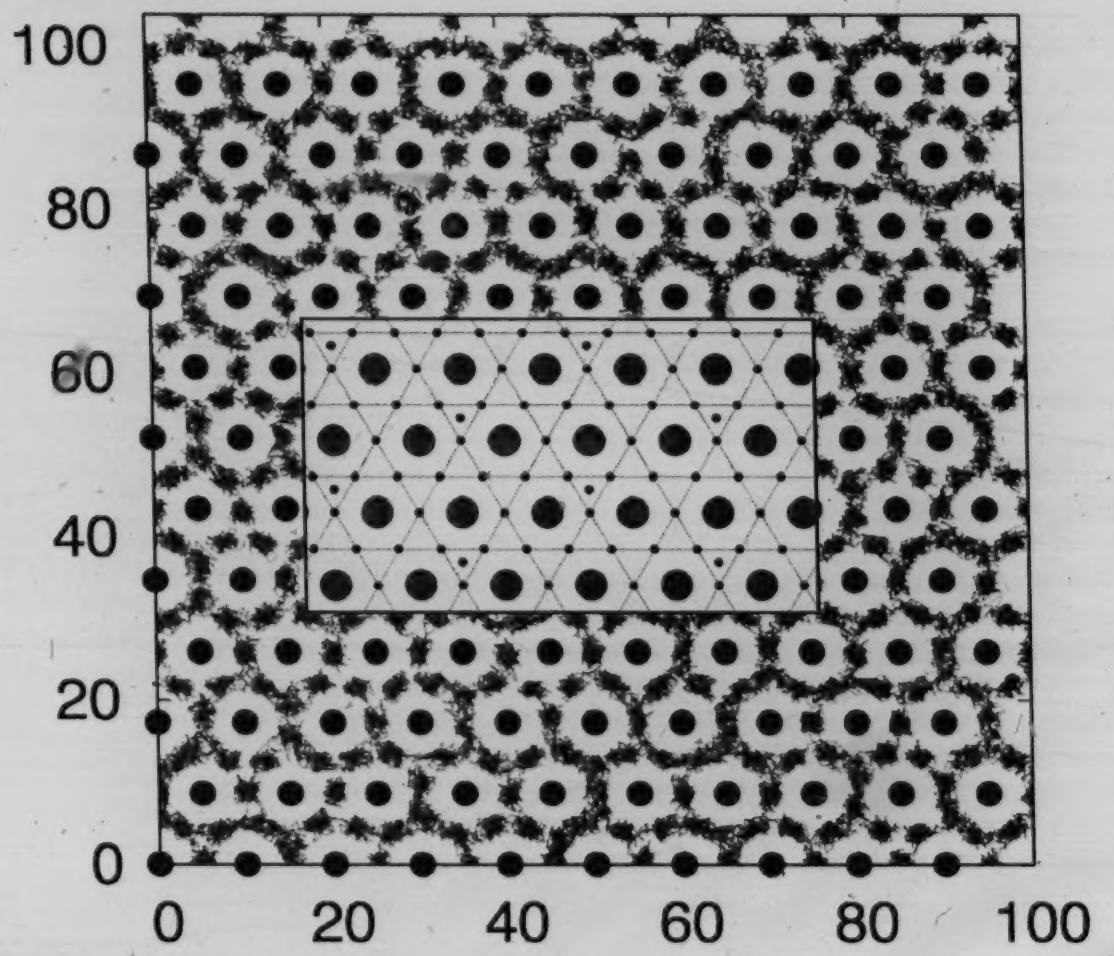


Figure 5.4: Snapshot of a typical configuration of $p$-$H_2$ molecules at low $T$ at $\theta = \theta_e$, intercalated within the periodic 2D fixed impurity matrix (described in the text). The positions of all $p$-$H_2$ molecules at each one of the imaginary time slices are shown as discrete paths, while impurities are shown as solid circles. All distances are in Å. Inset shows a schematic representation of the ensuing phase, inferred from a visual inspection of configurations. Large circles represent impurities, whereas smaller circles are $p$-$H_2$ molecules. Red circles are $p$-$H_2$ molecules forming the 1/3 commensurate triangular phase, which can occupy either one of two equivalent lattices (different color shades).

## 5.5 Results: $p$-$H_2$ intercalated within a random 2D impurity matrix

We now turn to describing the results obtained for *completely random* placement of scatterers. For each of the eight independent realizations of a random distribution of scatterers at a given density, we compute the ground state equilibrium $p$-$H_2$ coverage $\theta_e$; in general, the value of $\theta_e$ depends on the specific impurity realization, particularly for smaller system sizes. It is found to fluctuate typically within $\sim$10% from one realization to another. This gives an idea of the local density fluctuations that occur in the thermodynamic limit, as a result of the inhomogeneity of the system.

The extrapolated ground state energy per particle, $e(N)$, for a disordered arrangement of impurities, roughly interpolates between that for bulk 2D $p$-$H_2$ (see, for instance, Ref. [38]) and the energy for $p$-$H_2$ in the presence of periodic impurity arrays of the same density [53] as should be expected.

Fig. 5.5 shows a snapshot of the $p$-$H_2$ world lines for a system at the equilibrium coverage $\theta_e \approx 0.052$ Å$^{-2}$, for a specific realization of the disorder with an impurity density $\Omega = 0.0133$ Å$^{-2}$ (the temperature is $T = 0.5$ K). By visual inspection, we can clearly establish that the $p$-$H_2$ molecules attempt to recreate the triangular lattice associated with bulk 2D $p$-$H_2$ [38] interrupted by the underlying impurity matrix. This is consistently observed for all realizations of the disorder, at all impurity densities. Moreover, the observed little or no overlap among quantum-mechanical delocalization "clouds" of the different molecules are consistent with quantum exchanges being suppressed in this system.

The above findings are confirmed by an examination of the $p$-$H_2$ pair correlation function, shown in Figure 5.6 for disordered matrices of different impurity densities. Also shown for comparison is the pair correlation function for bulk 2D $p$-$H_2$ at the equilibrium coverage ($\theta$=0.056 Å$^{-2}$, from Ref. [38]), as well as for the case of a regular impurity matrix of density $\Omega$=0.01155 Å$^{-2}$. The progressive loss of structure at long distance, as the concentration of impurities is increased, is obvious; in contrast, the short-range features of the pair correlation function are essentially unaffected, largely reproducing those of the pair correlation function for bulk 2D $p$-$H_2$.

Analysis of the one-body density matrix reveals a rapid exponential decay, with no

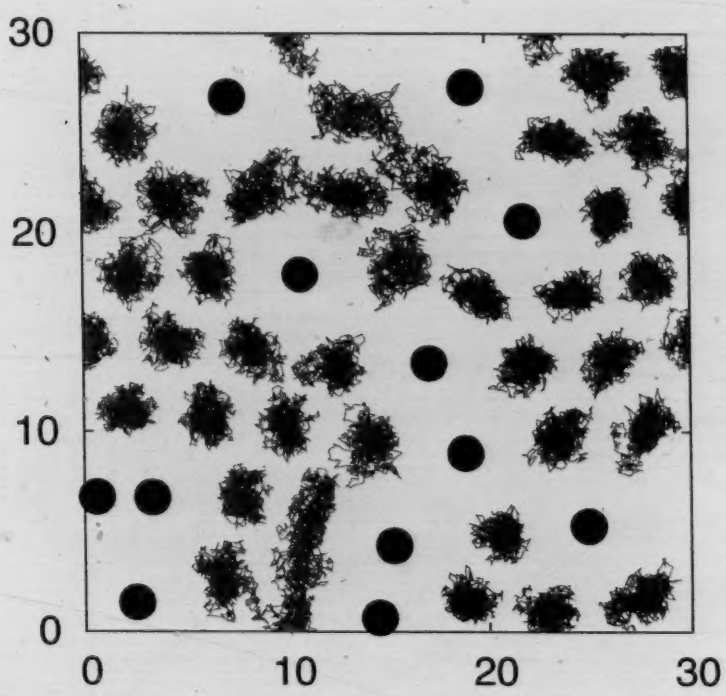


Figure 5.5: Snapshot of a typical configuration of $p$-$H_2$ molecules at $T$= 0.5 K for $\theta$=$\theta_e$, intercalated within the 2D matrix of randomly placed impurities with $\Omega$=0.0133 Å$^{-2}$. The positions of all $p$-$H_2$ molecules at each one of the imaginary time slices are shown as discrete paths, while impurities are shown as solid circles. All distances are expressed in Å.

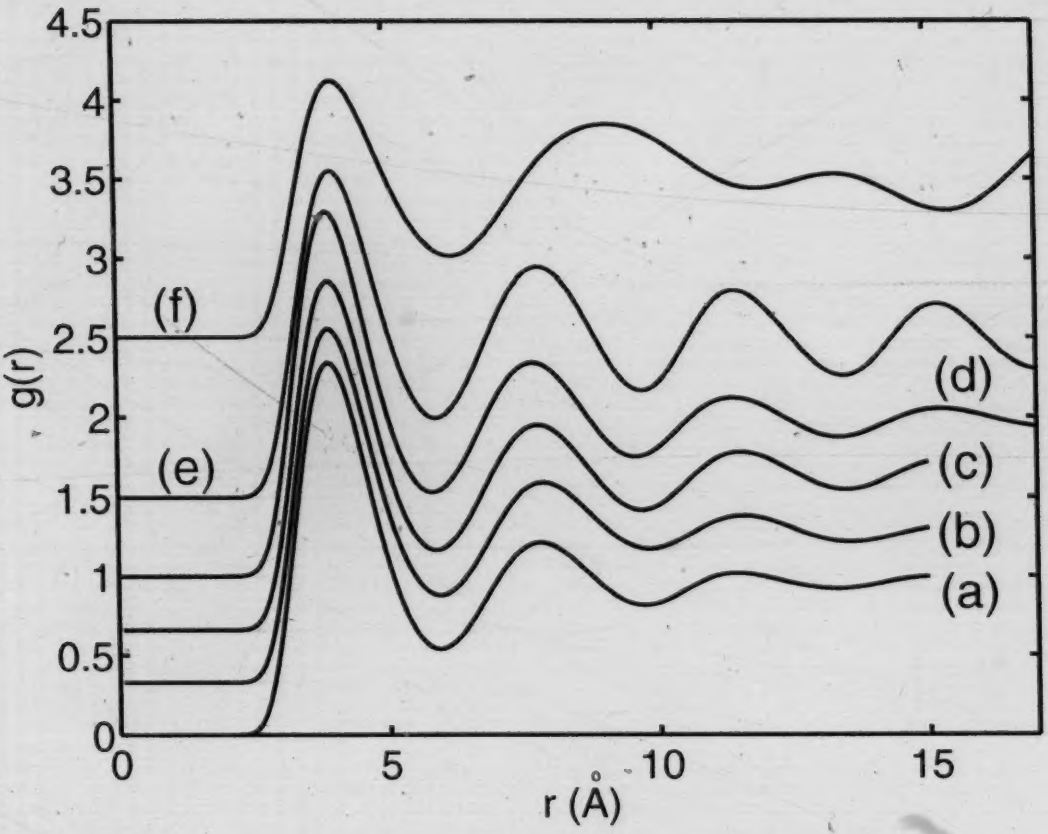


Figure 5.6: Ground state $p$-$H_2$ pair correlation functions ($g(r)$) for equilibrium $p$-$H_2$ coverage. All functions have been uniformly displaced upwards by their y-intercept to ease comparison. Results *a* through *d* refer to randomly placed impurities with decreasing density (from $\Omega$=0.022 (*a*) to 0.01155 (*d*) Å$^{-2}$). Also shown for comparison are $g(r)$ for bulk 2D $p$-$H_2$ (*e*), as well as for the case of a triangular impurity lattice (*f*), with impurity density $\Omega$=0.01155 Å$^{-2}$.

signature of a Kosterlitz-Thouless power-law decay. For each realization, we calculate a superfluid density of precisely zero, with quantum exchanges between $p$-$H_2$ molecules being strongly suppressed with respect to the systems with periodic impurity matrices; system-spanning permutations, necessary for the system to feature a finite superfluid response, are never generated. All evidence points to this system being a "Bose glass", devoid of both solid order and off-diagonal quasi-long-range order. Clearly, no enhancement of Bose statistics is brought about by disorder. In order to gain additional insight into the effect of disorder, we next study a physical arrangement of impurities that interpolates between the regular periodic array of Section 5.4 and the disordered configuration of Section 5.5.

## 5.6 Results: $p$-$H_2$ intercalated within a nearly-periodic 2D impurity matrix

For the case where impurities are located at positions obtained applying random displacements $D_{1,2}$ to regular triangular lattice sites (see Sec. 5.3.1), we find on average a 13% enhancement of the equilibrium $p$-$H_2$ coverage obtained in Section 5.4.

Structurally, one may infer from the pair correlation function (f) in Figure 5.6 that the $p$-$H_2$ is in a liquid-like or glassy state. Shown in Figure 5.7 is a typical world-line snapshot at $T$=0.5 K. Upon examination of many such "snapshots", we confirm that the (very limited) interparticle overlap observed in Figure 5.7 is the norm.

An accumulation of statistics indicate an enormous suppression of quantum exchanges, almost entirely absent. In every disordered impurity realization examined, the superfluid fraction $\rho_s$ is found to be exactly zero. The structure and lack of superflow exhibited when $D_{1,2}$ random displacements are applied, are also observed for $D_{0.5,2}$ and $D_{0,2}$ random displacements, with no significant physical changes observed in these three cases across all realizations. Altogether, these degrees of disorder imparted to the system are sufficient to induce strong particle localization, and eliminate even the local exchanges found for periodic arrays of impurities in smaller systems, as is the case for the systems studied in Section 4.4.

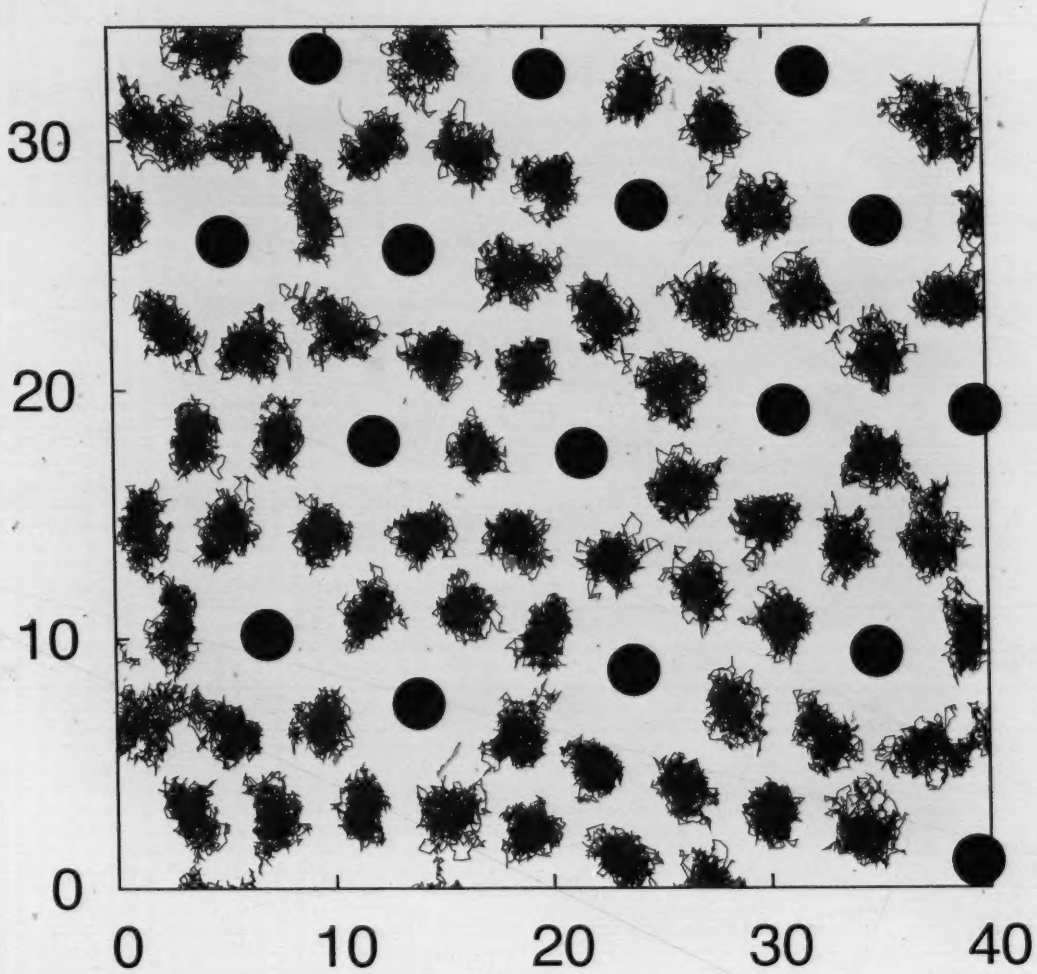


Figure 5.7: Snapshot of a typical configuration of $p$-$H_2$ molecules at $T = 0.5$ K for $\theta$=$\theta_e$, intercalated within the aperiodic 2D fixed impurity matrix with density $\Omega$=0.01155 Å$^{-2}$. The positions of all $p$-$H_2$ molecules at each one of the imaginary time slices are shown as discrete paths, while impurities are shown as solid circles. All distances are expressed in Å.

Upon reducing the magnitude of the impurity displacements to $D_{0,1}$ Å, we find significant variation from one realization to the next, with between a 0% and 4% enhancement of the equilibrium $p$-$H_2$ coverage with respect to the system having a periodic array of impurities (corresponding to at most 2 additional interstitial particles).

In realizations for which the particle density is unchanged, the same insulating phase found in Section 5.4 is recovered, albeit with a very slight broadening of $g(r)$.

In the realizations where additional molecules happen to be introduced (for example, in realizations where three impurities that are part of one nearest-neighbor triplet are displaced radially outward from their centroid by order 1.0 Å), $\rho_s$ is zero for all $T$, and the broadening of $g(r)$ with respect to that of Section 5.4 is more significant.

These results are adequate to conclude that the introduction of disorder which is strong enough to introduce additional particles into the $p$-$H_2$ crystal leads to acute particle localization and a suppression of exchanges; disorder weak enough to not change the equilibrium coverage does not cause a perturbation in the necessarily insulating $p$-$H_2$ crystal structure.

## 5.7 Conclusions

Using numerically exact finite-temperature path integral Monte Carlo (worm algorithm) methods, we studied purely 2D $p$-$H_2$ intercalated within an array of impurities. We performed calculations based on a simple model, in which the impurities are assumed static and point-like, and $p$-$H_2$-impurity interactions are given by a Lennard-Jones potential.

For $p$-$H_2$ intercalated within a periodic array of scatterers, the explicitly observed crystalline structure of hydrogen allows us to conclude with confidence that the results seen for the largest system sizes are indicative of the physics in the thermodynamic limit, and not a manifestation of algorithmic deficiency. The finite superfluid response observed in earlier simulations [52] of small systems (where the crystal structure could not be exactly realized) are thus attributable to finite-size effects.

From our simulations of $p$-$H_2$ in the presence of disordered arrays of impurities, we conclude that the introduction of such disorder enhances localization of $p$-$H_2$ molecules, suppressing quantum exchanges. Though disorder can give rise to a glassy phase, ex-

change frequencies are *suppressed* with respect to the exchange statistics observed in the systems with periodic arrays of impurities, in agreement with the conventional view of disorder-induced (Anderson) localization in strongly-interacting Bose systems.

Our primary conclusion is that $p$-$H_2$ intercalated within a 2D periodic or aperiodic array of impurities is not a candidate for the observation of superfluidity.

# Chapter 6

# Summary and Conclusions

We have studied quasi-2D molecular hydrogen at low temperature in a variety of regimes, with the goal of obtaining physical conditions compatible with the observation of hydrogenic superflow. Using state-of-the-art quantum Monte Carlo methods, we attempted to overcome the barriers to the observation of superfluid hydrogen - namely, crystallization and particle localization - by inducing a reduction of dimensionality, as well as inducing incommensuration.

Several systems are studied toward this end, including $p$-$H_2$ films adsorbed to fullerenes, $p$-$H_2$ and $o$-$D_2$ films adsorbed upon krypton pre-plated graphite, as well as $p$-$H_2$ intercalated within a strictly 2D crystal of impurities. We confirmed that reduction of dimensionality alone is insufficient to promote superflow, and that incommensuration can even enhance particle localization.

For our studies of the adsorption of $p$-$H_2$ on the surface of fullerenes at $T$=0, two models were adopted; the first treated each fullerene as a smooth spherical surface, interacting with $p$-$H_2$ with roughly the strength of a single plane of graphite. Strong particle localization was observed, with the $p$-$H_2$ found to approximately recreate their 2D equilibrium configuration (a triangular lattice).

A second model, incorporating the corrugated structure of the fullerenes, was then studied in the hopes of introducing incommensuration (i.e. disrupting the $p$-$H_2$ from roughly reproducing their 2D equilibrium triangular lattice structure). The equilibrium configuration of hydrogen in this case was, however, commensurate with the carbon-ring

adsorption sites on the surface of the fullerene, with severe particle localization experienced by $p$-$H_2$. The $p$-$H_2$ was found to in general be compressible, with $p$-$H_2$ again attempting to recreate their equilibrium 2D configurations on the fullerene surface as the chemical potential is increased.

Being solids with a high degree of particle localization, these systems are thus not candidates for the observation of the superfluid phase of $p$-$H_2$. Secondary information gleaned was related to the structural and energetic properties of adsorbed $p$-$H_2$ on fullerenes, of some relevance to the field of hydrogen fuel storage.

In our studies of $p$-$H_2$ and $o$-$D_2$ films adsorbed to the surface of krypton pre-plated graphite, inspired by [40], we also confirmed that reduction of dimensionality alone is insufficient to extend the fluid state of $p$-$H_2$ to a low enough temperature for superfluidity to be observed. The first goal was to study the adsorption of $p$-$H_2$ upon a surface similar to graphite, but more weakly interacting.

We found that there are two stable phases of $p$-$H_2$, both solid; one is a monolayer commensurate with the Kr layer, while the other is an incommensurate monolayer, compressible within a small range of coverages. Quantum exchanges of hydrogen molecules are suppressed in this system; altogether, our findings are similar to what is seen for $p$-$H_2$ on bare graphite.

A closely related system was then studied to probe a potential mechanism for inducing incommensuration. The krypton monolayer preplating the graphite substrate was instead compressed, following from additional structural information provided by one of the authors in [40]. In reference [40], it was reported that $o$-$D_2$ with coverage above 1/2 filling adsorbed upon such a geometry displays fluid-like properties down to $T$=1.5 K. The hypothesis was that a particular range of densities of $o$-$D_2$ are accommodated by the formation of commensurate regions separated by heavy domain walls, and that the position of these domain walls is fluid.

Using an exact ground state technique, for both $p$-$H_2$ and $o$-$D_2$, we found that a solid monolayer commensurate with the krypton layer is thermodynamically stable, and, in both cases, is the coverage corresponding to the minimum energy per particle. For $o$-$D_2$, we also found that there are two distinct compressible incommensurate solid regions, with the denser region, IC-II, corresponding to regions of commensuration separated by

domain walls. Investigation of this coverage region at finite temperature, using the worm algorithm, down to $T$=0.25 K, yielded no evidence of superfluidity, consistent with our observation of a high degree of localization of $o$-$D_2$ molecules. No quantum exchanges, and by extension permutations, are found to take place, though they are sampled efficiently.

Though our simulations support a "domain-wall fluid" interpretation offered by Wiechert et al, this mechanism was not found to support superfluidity of either hydrogen isotope. Our interpretation is that, while incommensuration is achieved in the sense that the number of particles is greater than the number of adsorption sites on one sublattice of the substrate, particles along the domain walls are still roughly localized around the minima of the potential, reducing zero-point motion sufficiently to suppress quantum many-body effects.

Following from the earlier work in [52], we next studied $p$-$H_2$ in a strictly 2D lattice of impurities, and probed this system as a function of density, temperature, and impurity distribution. In our preliminary results on small systems we found that reduction of dimensionality coupled with a particular form of incommensuration (where the equilibrium coverage of $p$-$H_2$ appeared to include a large, finite density of interstitials) lead to a novel state of molecular hydrogen supporting a finite superfluid density, simultaneously possessing diagonal long-range order and off-diagonal quasi-long-range order. The equilibrium phase of $p$-$H_2$ for small systems appeared to be an arrangement roughly coextensive (a kagomé tiling) with the impurity background, with the apparent presence of a 10% concentration of interstitials.

In order to qualify the claim that this system, in the thermodynamic limit, supports superflow of $p$-$H_2$, we next attempted to confirm the above structural properties for a much larger manifestation of the system, containing hundreds of impurities and $p$-$H_2$ molecules. Strong evidence is obtained that the $p$-$H_2$ forms a perfect crystal with a large unit cell (having non-trivial structure), devoid of interstitials. Such a phase, masked earlier by the small system size (for which the equilibrium structure is artificially frustrated), is necessarily insulating [49]. Thus, we are forced to conclude that the reported superfluid properties are finite-size artifacts, and that $p$-$H_2$ in this geometry is a regular quantum solid in the thermodynamic limit.

The second part to this investigation focused on the role of disorder, where our aim was to determine whether the above perfectly crystalline equilibrium phase could be weakly disrupted by the introduction of disorder, which could introduce true interstitials at equilibrium, and lead to long-range superfluid coherence. Though disorder is known to cause localization in general, it is also conceivable that a phase of $p$-$H_2$ similar to the "superglass" phase reported in Reference [55] could arise in disorder.

For sufficiently strong disorder, even though we observed exchanges of small groups of molecules, they had a local character, i.e., long permutation cycles spanning the entire system did not occur; as a result, a finite superfluid signal never materialized in the low temperature limit even for relatively small systems. We observed a glassy phase, but we also clearly observed that $p$-$H_2$ molecules *locally* attempted to recreate the triangular lattice structure associated with bulk 2D $p$-$H_2$ at equilibrium [38], only interrupted by the underlying impurity matrix.

For weak disorder, a minor random displacement of the background impurities was found to not disrupt the crystalline state of $p$-$H_2$; as the magnitude of the random displacements was increased to the point where the crystal structure of $p$-$H_2$ was disrupted and interstitials form part of the equilibrium phase, all trace of off-diagonal quasi-long-range order was destroyed.

Altogether, we found strong evidence suggesting that reduction of dimensionality, incommensuration, and imposed disorder, even in conjunction, cannot stabilize a superfluid or supersolid state of bulk 2D $p$-$H_2$. The prognosis, it seems, for observing superfluidity of $p$-$H_2$ in 2D films, is not an optimistic one. Though it is possible that incommensuration may permit an enhancement of disorder and even the formation of a fluid-like state, as shown in chapter 4, it is doubtful that this particular flavor of disorder can ever enhance particle exchange, and indeed here appears to instead suppress it as well. Based on this collection of null results, we conclude that a superfluid phase of 2D $p$-$H_2$ is *not* likely to be observed, in the absence of some indirect physical mechanism capable of renormalizing (weakening) the effective interaction among molecules. We leave open the **remote** theoretical possibility that one could carefully craft a "substrate" supporting a finite density of interstitials or extended defects (which persist in the thermodynamic limit) as part of the low-temperature equilibrium phase of solid 2D $p$-$H_2$, leading to a potential

bulk supersolid state of molecular hydrogen, albeit in an artificial and highly controlled setting.

Barring such a mechanism, superfluid behavior in $p$-$H_2$ may be observed experimentally in finite size systems only, e.g., clusters [28, 111].

# Bibliography


[1] P. Kapitza. *Nature*, 141:74, 1938.

[2] J. F. Allen and A. D. Misener. *Nature*, 141:75, 1938.

[3] F. London. *Phys. Rev.*, 54:947, 1938.

[4] L. Tisza. *Nature*, 141:913, 1938.

[5] W. H. Keesom and G. E. MacWood. *Physica*, 5:737, 1938.

[6] E. L. Andronikashvilii. *J. Phys. USSR*, 10:201, 1946.

[7] L. Landau. *Phys. Rev.*, 75:884, 1949.

[8] D. G. Henshaw and A. D. Woods. *Phys. Rev.*, 121:1266, 1961.

[9] C. E. Chase. *Phys. Rev.*, 127:361, 1962.

[10] J. G. Daunt and R. S. Smith. *Rev. Mod. Phys.*, 26:172, 1954.

[11] J. Bardeen, L. N. Cooper, and J. R. Schrieffer. *Phys. Rev.*, 106:162, 1957.

[12] M. H. Anderson, J. R. Ensher, M. R. Matthews, C. E. Wieman, and E. A. Cornell. *Science*, 269:198, 1995.

[13] A. Griffin, D. W. Snoke, and S. Stringari. *Bose-Einstein condensation*. Cambridge, 1995.

[14] N. D. Mermin and H. Wagner. *Phys. Rev. Lett.*, 17:1133, 1966.

[15] P. C. Hohenberg. *Phys. Rev.*, 158:383, 1967.

[16] J. M. Kosterlitz and D. J. Thouless. *J. Phys. C: Solid State Phys.*, 6:1181, 1973.

[17] J. M. Kosterlitz and D. J. Thouless. *Progress in Low Temperature Physics*, VIIB:371, 1978.

[18] N. Bernardes. *Phys. Rev.*, 120:807, 1960.

[19] A. I. Safonov, S. A. Vasilyev, I. S. Yasnikov, I. I. Lukashevich, and S. Jaakkola. *Phys. Rev. Lett.*, 81:4545, 1998.

[20] V. L. Ginzburg and A. A. Sobyanin. *JETP*, 15:242, 1972.

[21] M. Bretz and A. L. Thomson. *Phys. Rev. B*, 24:467, 1981.

[22] G. M. Seidel, H. J. Maris, F. I. B. Williams, and J. G. Cardon. *Phys. Rev. Lett.*, 56:2380, 1986.

[23] H. J. Maris, G. M. Seidel, and F. I. B. Williams. *Phys. Rev. B*, 36:6799, 1987.

[24] M. Schindler, A. Dertinger, Y. Kondo, and F. Pobell. *Phys. Rev. B*, 53:11451, 1996.

[25] P. Sindzingre, D. M. Ceperley, and M. L. Klein. *Phys. Rev. Lett.*, 67:1871, 1991.

[26] F. Mezzacapo and M. Boninsegni. *Phys. Rev. A*, 75:033201, 2007.

[27] F. Mezzacapo and M. Boninsegni. *Phys. Rev. A*, 76:021201, 2007.

[28] F. Mezzacapo and M. Boninsegni. *Phys. Rev. Lett.*, 100:145301, 2008.

[29] S. Grebenev, B. Sartakov, J. P. Toennies, and A. F. Vilesov. *Science*, 289:1532, 2000.

[30] Y. Kwon and K. B. Whaley. *Phys. Rev. Lett.*, 89:273401, 2002.

[31] F. Paesani, R. F. Zillich, and K. B. Whaley. *J. Chem. Phys.*, 119:11682, 2003.

[32] M. Nielsen, J. P. McTague, and L. Passell. In J. Dash and J. Ruvalds, editors, *Phase Transitions in Surface Films*. Plenum, New York, 1980.

[33] J. Ma, D. L. Kingsbury, F. Liu, and O. E. Vilches. *Phys. Rev. Lett.*, 61:2348, 1988.

[34] H. J. Lauter, H. Godfrin, V. L. P. Frank, and P. Leiderer. In H. J. Lauter H. Taub, G. Torzo and S. C. Fain Jr., editors, *Phase Transitions in Surface Films 2*. Plenum, New York, 1990.

[35] H. Wiechert. In A. F. G. Wyatt and H. J. Lauter, editors, *Excitations in Two-Dimensional and Three-Dimensional Quantum Fluids*. Plenum, New York, 1991.

[36] F. C. Liu, Y. M. Liu, and O. E. Vilches. *J. Low Temp. Phys.*, 89:649, 1992.

[37] F. Liu, Y. Liu, and O. E. Vilches. *Phys. Rev. B*, 51:2848, 1995.

[38] M. Boninsegni. *Phys. Rev. B*, 70:193411, 2004.

[39] M. Boninsegni. *Phys. Rev. B*, 70:125405, 2004.

[40] H. Wiechert, K.D. Kortmann, and N. Stüber. *Phys. Rev. B*, 70:125410, 2004.

[41] L. Pollet, M. Boninsegni, A. B. Kuklov, N. V. Prokofev, B. V. Svistunov, and M. Troyer. *Phys. Rev. Lett.*, 99:035301, 2007.

[42] O. Penrose and L. Onsager. *Phys. Rev.*, 104:205421, 1956.

[43] P. W. Anderson. *Basic Notions of Condensed Matter Physics*. Addison Wesley, New York, 1984.

[44] A. F. Andreev and I. M. Lifshitz. *Sov. Phys. JETP*, 29:1107, 1969.

[45] G. V. Chester. *Phys. Rev. A*, 2:256, 1970.

[46] A. J. Leggett. *Phys. Rev. Lett.*, 25:1543, 1970.

[47] E. Kim and M. Chan. *Nature*, 427:225, 2004.

[48] S. Sasaki, R. Ishiguro, F. Caupin, H. J. Maris, and S. Balibar. *Science*, 313:5790, 2006.

[49] N. V. Prokofev and B. V. Svistunov. *Physical Review Letters*, 94:155302, 2005.

[50] M. Boninsegni, A. B. Kuklov, L. Pollet, N. V. Prokofev, B. V. Svistunov, and M. Troyer. *Phys. Rev. Lett.*, 97:080401, 2006.

[51] M. Boninsegni, A. B. Kuklov, L. Pollet, N. V. Prokofev, B. V. Svistunov, and M. Troyer. *Phys. Rev. Lett.*, 99:135301, 2007.

[52] M. C. Gordillo and D. M. Ceperley. *Phys. Rev. Lett.*, 79:3010, 1997.

[53] M. Boninsegni. *New J. Phys.*, 7:78, 2005.

[54] M. P. Fisher, P. B. Weichman, G. Grinstein, and D. S. Fisher. *Phys. Rev. B*, 40:546, 1989.

[55] M. Boninsegni, N. V. Prokofev, and B. V. Svistunov. *Phys. Rev. Lett.*, 96:105301, 2006.

[56] Massimo Boninsegni. *Monte Carlo Methods in Statistical Physics,*, Physics 646 Course Notes, 2004.

[57] R. Feynman. *Rev. Mod. Phys.*, 20:348, 1948.

[58] W. Pauli. *Phys. Rev.*, 58:716, 1940.

[59] J. E. Cuervo, P.N. Roy, and M. Boninsegni. *J. Chem. Phys.*, 122:114504, 2005.

[60] M. Boninsegni. *Journal of Low Temperature Physics*, 141:27, 2005.

[61] D.M. Ceperley. *Rev. Mod. Phys.*, 67:279, 1995.

[62] M. Boninsegni, N. V. Prokofev, and B. V. Svistunov. *Phys. Rev. Lett.*, 96:070601, 2006.

[63] M. Boninsegni, N. V. Prokofev, and B. V. Svistunov. *Phys. Rev. E*, 74:036701, 2006.

[64] A. Sarsa, K. E. Schmidt, and W. R. Magro. *J. Chem. Phys.*, 113:1366, 2000.

[65] S. Jang, S. Jang, and G. A. Voth. *J. Chem. Phys.*, 115:7832, 2001.

[66] S. Zhang, N. Kawashima, J. Carlson, and J.E. Gubernatis. *Phys. Rev. Lett.*, 74:1500, 1995.

[67] M. P. Allen and D. J. Tildesley. *Computer Simulation of Liquids*. Oxford University Press, 1994.

[68] Y. Xian. *Phys. Rev. A*, 77:042103, 2008.

[69] S. Castillo, A. Cruz, A. Cuan, A. Ramrez-Solis, E. Poulain, and G. DelAngel. *International Journal of Quantum Chemistry*, 56:549, 2004.

[70] I. F. Silvera and V. V. Goldman. *J. Chem. Phys.*, 69:4209, 1978.

[71] B. Axilrod and E. Teller. *J. Chem. Phys.*, 11:299, 1943.

[72] R. J. Sadus. *Fluid Phase Equilibria*, 150:63, 1998.

[73] H. Wiechert. *Adsorption of Molecular Hydrogen Isotopes on Graphite and Boron Nitride*. Springer-Verlag, Berlin, 2003.

[74] M. Wagner and D. M. Ceperley. *Journal of Low Temperature Physics*, 94:161, 1994.

[75] M. Wagner and D. M. Ceperley. *Journal of Low Temperature Physics*, 102:275, 1996.

[76] K. Nho and E. Manousakis. *Phys. Rev. B*, 65:115409, 2002.

[77] W. Shi, J. K. Johnson, and M. W. Cole. *Phys. Rev. B*, 68:125401, 2003.

[78] E. Cheng, G. Mistura, H. C. Lee, M. H. W. Chan, M. W. Cole, C. Carraro, W. F. Saam, and F. Toigo. *Phys. Rev. Lett.*, 70:1854, 1993.

[79] G. Mistura, H. C. Lee, and M. H. W. Chan. *Journal of Low Temperature Physics*, 96:221, 1994.

[80] D. Ross, P. Taborek, and J. E. Rutledge. *Phys. Rev. B*, 58:4274, 1998.

[81] E. S. Hernandez, M. W. Cole, , and M. Boninsegni. *Phys. Rev. B*, 68:125418, 2003.

[82] L. Szybisz and I. Urrutia. *Journal of Low Temperature Physics*, 134:516, 2004.

[83] A. C. Dillon, K. M. Jones, T. A. Bekkedahl, C. H. Kiang, D. S. Bethune, and M. J. Heben. *Nature*, 386:377, 1997.

[84] C. Liu, Y. Y. Fan, M. Liu, H. T. Cong, H. M. Cheng, and M. S. Dresselhaus. *Science*, 286:1127, 1999.

[85] Q. Wang and J. K. Johnson. *J. Chem. Phys.*, 110:577, 1999.

[86] B. K. Pradhan, A. R. Harutyunyan, D. Stojkovic, J. C. Grossman, P. Zhang, M. W. Cole, V. H. Crespi, H. Goto, J. Fujiwara, and P. C. Eklund. *J. Mater. Res.*, 17:2209, 2002.

[87] D. Levesque, A. Gicquel, F.L. Darkrim, and S.B. Kayiran. *J. Phys. CM*, 14:9285, 2002.

[88] F. Operetto and F. Pederiva. *Phys. Rev. B*, 69:024203, 2004.

[89] D. J. Han, S. Wolf, S. J. Oliver, C. McCormick, M. T. DePue, and D. S. Weiss. *Phys. Rev. Lett.*, 85:724, 2000.

[90] E. Riis and S. M. Barnett. *Europhys. Lett.*, 30:441, 1995.

[91] M. E. Gehm, K. M. O'Hara, T. A. Savard, and J. E. Thomas. *Phys. Rev. A*, 61:029902, 2000.

[92] M. J. Tejwani, O. Ferreira, and O. E. Vilches. *Phys. Rev. Lett.*, 44:152, 1980.

[93] J. Turnbull and M. Boninsegni. *J. Low Temp. Phys.*, 140:269, 2005.

[94] W. A. Steele. *Surf. Sci.*, 36:317, 1973.

[95] R. J. Gooding, B. Joos, and B. Bergersen. *Phys. Rev. B*, 27:7669, 1983.

[96] I. F. Silvera and V. V. Goldman. *J. Chem. Phys.*, 69:4209, 1978.

[97] Q. Wang and J.K. Johnson. *Molecular Physics*, 95:299, 1998.

[98] D. MacGowan and Denis J. Evans. *Phys. Rev. A*, 34:2133, 1986.

[99] R. J. LeRoy, H. Wei, R. Wheatley, and W. J. Meath. *J. Chem. Phys.*, 122:084321, 2005.

[100] S.M. Gatica and J.K. Johnson. *J. Phys. Chem. B*, 108:11704, 2004.

[101] M. Boninsegni and L.Szybisz. *Phys. Rev. B*, 70:024512, 2004.

[102] H. Freimuth and H. Wiechert. *Surf. Sci.*, 178:716, 1986.

[103] J. Cui, J. D. White, R. D. Diehl, J. F. Annett, and M. W. Cole. *Surf. Sci.*, 279:149, 1992.

[104] G. S. Leatherman and R. D. Diehl. *Phys. Rev. B*, 53:4939, 1996.

[105] D. M. Ceperley and E. L. Pollock. *Phys. Rev. B*, 39:2084, 1989.

[106] P. Bogacki and L. F. Shampine. *Appl. Math. Letters*, 2:1, 1989.

[107] L. Pollet, M. Boninsegni, A. Kuklov, N. Prokof'ev, B. Svistunov, and M. Troyer. *Phys. Rev. Lett.*, 99:035301, 2007.

[108] M. Boninsegni, A. Kuklov, L. Pollet, N. Prokof'ev, B. Svistunov, and M. Troyer. *Phys. Rev. Lett.*, 98:135301, 2007.

[109] J. Turnbull and M. Boninsegni. *Phys. Rev. B*, 76:104524, 2007.

[110] M. Boninsegni. *J. Low Temp. Phys.*, 132:39, 2005.

[111] F. Mezzacapo and M. Boninsegni. *Phys. Rev. Lett.*, 97:045301, 2006.